Aβ Amyloid Scaffolds the Accumulation of Matrisome and Additional Proteins in Alzheimer's Disease.

Yona Levites*[1,4,5], Eric B. Dammer*[2,4,5], Yong Ran[1,4,5], Wangchen Tsering[6,7,8], Duc Duong[2,4,5], Measho Abreha[2,4,5], Joshna Gadhavi[2,4,5], Kiara Lolo[6,7,8], Jorge Trejo-Lopez[6,7,8], Jennifer Phillips[6,7,8], Andrea Iturbo, Aya Erquizi, Brenda D. Moore[1,4,5], Danny Ryu[1,4,5], Aditya Natu[2,4,5], Kristy Dillon[7,8,9], Jose Torrellas[7,8,9], Corey Moran[7,8,9], Thomas Ladd [7,8], Farhana Afroz[1,4,5], Tariful Islam[1,4,5], Jaishree Jagirdar[13], Cory C. Funk[14], Max Robinson[14], David R. Borchelt[7,8,9], Nilüfer Ertekin-Taner[11, 12], Jeffrey W. Kelly[15], Frank L. Heppner[16], Erik C. B. Johnson[3,4,5], Karen McFarland[7,8,10], Allan I. Levey[3,4,5,] Stefan Prokop**[6,7,8], Nicholas T. Seyfried**[2,4,5],Todd E. Golde**[1,3,4,5].

[1]Department of Pharmacology and Chemical Biology, School of Medicine, Emory University, Atlanta, GA, USA.
[2]Department of Biochemistry, School of Medicine, Emory University, Atlanta, GA, USA.
[3]Department of Neurology, School of Medicine, Emory University, Atlanta, GA, USA.
[4]Goizueta Brain Health Institute and Alzheimer's Disease Research Center, Emory University School of Medicine, Atlanta, GA, USA.
[5]Center for Neurodegenerative Disease Center, Emory University School of Medicine, Atlanta, GA, USA.
[6]Department of Pathology, College of Medicine, University of Florida, Gainesville, USA.
[7]Evelyn F. and William L. McKnight Brain Institute, University of Florida, Gainesville, Fl, USA.
[8]Center for Translational Research in Neurodegenerative Disease, University of Florida, Gainesville, Fl, USA.
[9]Department of Neuroscience, College of Medicine, University of Florida, Gainesville, USA.
[10]Department of Neurology, College of Medicine, University of Florida, Gainesville, USA
[11]Mayo Clinic, Department of Neuroscience, Jacksonville, FL, USA.
[12]Mayo Clinic, Department of Neurology, Jacksonville, FL, USA.
[13]Department of Pathology and Laboratory Medicine, Emory University Hospital. Atlanta, GA, USA.
[14]Institute for Systems Biology, Seattle, WA, USA
[15]Department of Chemistry and The Skaggs Institute for Chemical Biology, The Scripps Research Institute, La Jolla, California, USA.
[16]Department of Neuropathology, Charité – Universitätsmedizin Berlin, corporate member of Freie Universität Berlin and Humboldt-Universität zu Berlin; German Center for Neurodegenerative Diseases (DZNE) Berlin; Cluster of Excellence, NeuroCure, Charitéplatz 110117 Berlin, Germany

Keywords: proteomics, Alzheimer's disease, amyloid, models, plaques, aggregation

Running Title: Amyloid Scaffolds the Matrisome

Abstract

We report a highly significant correlation between human Alzheimer's disease (AD) brain proteome changes and those in CRND8 $APP_{695NL/F}$ transgenic mice. Comparing protein changes observed in the CRND8 mice with co-expression networks derived from human Alzheimer's disease (AD), reveals both conserved and divergent module changes. Many proteins in the most highly conserved module (M42, matrisome) accumulate in plaques, cerebrovascular amyloid (CAA), dystrophic neuronal processes, or a combination thereof. Overexpression of two M42 proteins, midkine (Mdk) and pleiotrophin (PTN), in CRND8 mice brains leads to increased accumulation of Aβ in plaques and in blood vessels; further, recombinant MDK and PTN enhance Aβ aggregation into amyloid structures. Multiple M42 proteins bind to fibrillar Aβ42 and a non-human amyloid fibril *in vitro*. Supporting this binding data, MDK and PTN co-accumulate with transthyretin (TTR) amyloid in the heart. Notably, our findings establish that proteomic changes in modules observed in human AD brains define an Aβ amyloid "responsome" that is well conserved from mouse models to humans. Further, distinct amyloid structures appear to serve as scaffolds, facilitating the co-accumulation of proteins with signaling functions, and this co-accumulation may contribute to downstream pathological sequalae. Overall, this contextualized understanding of proteomic changes and their interplay with amyloid deposition provides valuable insights into the complexity of AD pathogenesis and potential biomarkers and therapeutic targets.

INTRODUCTION

The amyloid cascade hypothesis (ACH) serves as a foundational framework for comprehending the pathogenesis of Alzheimer's disease (AD) [1,2]. Recent evidence from anti-amyloid immunotherapies, developed based on this hypothesis, offers the initial therapeutic validation, affirming the central tenet that Aβ deposition plays a role in the AD pathogenic cascade [3-5]. These antibodies target the early symptomatic phase of AD demonstrating robust reductions in brain Aβ amyloid, slowing AD decline, but not halting or reversing it. Collectively, these findings reinforce the previously proposed notion within the field that, by the time symptoms manifest, the influence of amyloid itself is limited, while additional pathologies may become self-reinforcing or irreversible [6].

Despite extensive investigation, significant gaps in our understanding of AD pathogenesis remain [2,7,8]. The initial notion of a purely linear amyloid cascade, whereby Aβ amyloid deposition in sequence triggers neurofibrillary tau pathology, neuronal degeneration, immune responses, and clinical AD symptoms, is now recognized as overly simplistic. Studies utilizing proteomic, transcriptomic, metabolomic, pathological, and biomarker approaches have unveiled the intricate complexity of changes occurring over decades in the brains of individuals as various AD hallmark pathologies emerge [7,9-24]. These investigations reveal potentially non-linear and multifaceted alterations that affect all major cell-types in the brain, ultimately resulting in regional and widespread organ failure.

At a systems-level, these pathological and cellular changes manifest as fluctuations in protein levels, transcript quantities, and metabolite concentrations, even in brain regions where significant pathology may not be apparent [13]. This further underscores the complexity of AD pathogenesis and highlights the need to consider diverse factors contributing to disease progression beyond the core proteins implicated by the ACH or genetic studies. Comprehensive analyses incorporating multi-omic datasets such as those generated by the Accelerating Medicine Partnership for AD (AMP-AD) and other consortiums provide crucial insights into the systems pathobiology of AD, enabling a more nuanced comprehension of the disease's dynamic processes occurring at the cellular and molecular [7,9-24].

Typically, systems-level omic studies alone cannot establish cause and effect relationships. However, by combining strong correlational inference with omics obtained from different AD stages, we can generate hypotheses regarding causality or the role of these changes in the disease. To determine whether these omic-level changes are a consequence of disease or play a more fundamental role in pathogenesis, it is essential to i) compare the data across related disorders and disease models, ii) integrate the data with genetic risk and biomarker information, and iii) directly manipulate the levels of the altered proteins or RNAs in various model systems to observe their impact on pathophysiology potentially relevant to human AD. By undertaking these approaches, we can gain deeper insights into the significance of omic-level changes in AD, going beyond their descriptive nature and unraveling their potential role in the disease process.

Here, we performed quantitative tandem mass tag mass spectrometry (TMT-MS) based proteomics analyses of the brains from CRND8 transgenic mice at various ages and compared these findings to human proteomic data previously generated from >500 subjects from the Religious Orders Study/Memory and Aging Project (ROSMAP) and Banner Sun Health cohorts [9]. We find robust and highly significant correlation in global proteome changes in human AD brain compared to CRND8 transgenic mouse models. Through integration of protein changes observed in mouse models with co-expression networks derived from human AD, we resolve conserved and divergent network module changes between humans and mice. Multiple proteins that map to the M42 matrisome module, accumulate in Aβ plaques, cerebrovascular amyloid (CAA) and/or dystrophic neuronal processes. We also demonstrate that overexpressing two M42 proteins, midkine (Mdk) and pleiotrophin (PTN), in CRND8 mice leads to accelerated accumulation of Aβ, accompanied by dramatic Aβ amyloid increases in blood vessels linked to CAA. Moreover, *in vitro*

experiments using recombinant MDK and PTN reveal their ability to enhance Aβ aggregation into amyloid structures. Surprisingly, we find that many M42 proteins exhibit binding to fibrillar Aβ and non-human amyloid fibrils *in vitro*. Supporting this association, both MDK and PTN co-accumulate with transthyretin (TTR) amyloid in the heart. These findings establish several critical insights. First, that specific proteomic or module changes observed in human AD brains result from amyloid deposition. Second, amyloid structures seem to serve as scaffolds, facilitating the co-accumulation of proteins such as MDK and PTN with well-established signaling functions. This comprehensive understanding of proteomic changes and their interplay with amyloid deposition provides valuable insights into the complexity of AD pathogenesis and potential biomarkers. More specifically, they suggest that antagonizing MDK and/or PTN binding to amyloid could be a therapeutic strategy.

RESULTS

Deep TMT MS proteomes from 6, 12and 18M CRND8 APP Mice

We have generated TMT-MS proteomic data from the 8M urea extracts of the brains of 6 months (M) 12M and 18M CRND8 mice and non-transgenic (non-Tg) controls (Figure 1, Table S1-S5). We identified 8561, 10066, and 10543 proteins in the 6M, 12M and 18M cohorts with <50% missing values. In the 6M cohort, CRND8 mice show 1097 significant differentially expressed proteins (DEPs) with 172 increased and 65 decreased by more than 20% (Figure 1A). In the 12M cohort, 2340 DEPs are detected with 454 increased and 327 decreased by more than 20% (Figure 1B). In the 18M cohort, 2244 DEPs are detected with 639 increased and 450 decreased by more than 20% (Figure 1C). Notably, proteomic changes in 12M and 18M cohorts are highly reproducible (R^2=0.8129 $p<1e^{-200}$) (Figure 1D), despite being close, but not precise biological replicates. Indeed, out of the 1006 proteins that were significantly altered and detected in both cohorts only 8 were discordant and for these the log2 fold change (log2 Fc) was modest. Such data indicate that using small cohorts of CRND8 mice and matched non-Tg brains with varying levels of amyloid deposition, we can reliably and reproducibly detect proteomic alterations and that these changes increase with age in this transgenic mouse model of rapid and robust Aβ deposition.

Both full-length APP and specific peptides mapping to the human Aβ peptide sequence also distinguishes Tg from non-Tg mice in all cohorts, consistent with human transgene expression and increasing deposition of Aβ (Figure 1A-C, Table S1). Other proteins previously shown to interact with APP such as (Apbb1 (Fe65), Vac14, Rufy2, Tnfrsf21) are also altered at various ages in the CRND8 proteome and several of these (Apbb1, Vac14, Rufy2) show relatively stable alterations across the age groups suggesting that these may be related to mutant APP overexpression and not linked to Aβ or the response to Aβ accumulation per se (Table S1) [25-27]. Top gene ontology (GO) terms for the DEPs increased in all cohorts highlight heparin and glycosaminoglycan binding, amyloid fibril formation and regulation, vacuolar and lysosomal transport, and immune phagosome and vesicular and lysosomal transport, integrin binding and extracellular matrix (ECM) organization (Figure 1E). Top ontology terms for the decreased DEPs in all cohorts highlight impacts on lipid binding, synaptic vesicle regulation and neurotransmitter release, mitochondrial membrane, and neurogenesis and axogenesis. (Figure 1E).

In the 12 and 18M cohorts there is an appreciable rightward shift in the volcano plots reflecting many proteins that show an age dependent increase in protein level indicating such changes may reflect the evolving "responsome" to enhanced accumulation of Aβ. A subset of the proteins that show the largest fold change increase have been observed to be altered in other APP mouse models and in humans [9,10,14,18,28,29] (Table S1). However, in this study using the older CRND8 mice which have extensive parenchymal amyloid deposition in the forebrain and hippocampus and cerebrovascular amyloid deposition (CAA) in the cerebellum, we appear to detect a more comprehensive picture of the alterations in the proteome in response to Aβ deposition in the brain. Top gene ontology (GO) and KEGG terms for the DEPs that are significantly increased in the 18M CRND8 cohort by log2 Fc > 0.2 and increase by more

146 than 2-fold relative to the change observed in the 6M cohort highlight endosomal and lysosomal
147 processes, axonogenesis and neurogenesis, ECM organization, nitric oxide and superoxide metabolism,
148 and glycosaminoglycan degradation, and many other processes (Figure 1G). Limiting the input for these
149 analyses to the subset of proteins with significant log 2Fc > 1 in the 18M cohort, highlight oligodendrocyte
150 differentiation, synaptic signaling and organization, glycoprotein and, heparin, sulfur compound binding,
151 ECM, and neurogenesis and axogenesis (Figure 1H). Top gene ontology (GO) and KEGG terms for the DEPs
152 that are significantly decreased in the 18M CRND8 cohort by log2 Fc < -0.1 and decrease by more than 2-
153 fold relative to the change observed in the 6M cohort highlight terms around neurotransmitter
154 localization and synaptic function, neurogenesis and axogenesis, signal transduction and protein
155 localization to membrane rafts (Figure 1I).

156 **Integration of the AD human brain and CRND8 mouse brain proteome reveals both conserved and**
157 **divergent changes.**

158 To better understand the similarities and differences in protein levels between human AD and control
159 brains and in theCRND8 Tg and non-Tg mouse brain, we leveraged an extensive proteomic network
160 analysis and the resulting modular framework from human AD and control brains that has been previously
161 published. Using identical TMT-MS methodologies, we have built a deep consensus proteomic network
162 of >8,600 proteins from the dorsal lateral prefrontal cortex of >500 subjects from the Religious Orders
163 Study/Memory and Aging Project (ROSMAP) and Banner Sun Health cohorts [9]. This network was
164 constructed using the weighted gene co-expression network algorithm (WGCNA) and consists of 44
165 modules that reflect multiple biological and cell type processes, many of which are altered in AD. Globally,
166 when the levels of 7588 overlapping proteins are compared between the 18M CRND8 Tg and non-Tg
167 brains and AD and control brains there is a significant correlation ($p<1e^{-9}$, $R^2=0.158$) (Figure 2A); the
168 strength of the correlation is increased when filtering on the significant DEPs (n =709) in both the CRND8
169 and human AD brain proteomes relative to respective controls ($p<1e^{-9}$, $R^2=0.458$) (Figure 2B). Comparison
170 of the 6M CRND8 proteome changes with AD reveals a much weaker correlations for all overlapping
171 proteins (n=6794, $p<1e^{-9}$, $R^2=0.018$) (Figure 2C) but still a strong correlation for shared DEPs ($p<1e^{-9}$,
172 $R^2=0.438$) albeit with many fewer shared DEPs (n=161) (Figure 2D). Notably, the correlation for proteins
173 is stronger than for the correlations between protein coding mRNAs in 20M old CRND8 mice vs. non-Tg
174 mice brains and human AD and control brain superior temporal cortex from Mayo Clinic AD vs. control
175 RNAseq data (orthologous protein coding RNAs, n=13066, $R^2=0.079$; all shared DEGs, n=1399, $R^2=0.276$,
176 Figure S1) [12,30].

177 Inclusive correlations of all proteins shared within each of the human modules revealed select
178 modules with high overall correlations in terms of directionality and magnitude of changes, and modules
179 with negative correlations (Figure 2E). More granularly, when we assess the CRND8 mouse proteome
180 changes by evaluating the DEPs and preservation of direction of change within the human AD brain
181 module structure (Figure 2F), we find that there are number of modules in which there is a high degree
182 of preservation between the CRND8 mouse to human proteome in terms of DEP representation. There
183 are also modules for which many DEPs are discordant in terms of directionality, as well as modules where
184 the preservation of directionality is mixed (referred to as non-concordant). Modules showing strong
185 preservation and shared DEPs with increased levels are M42 (Matrisome), M11 (ECM), M7 (MAPK
186 Signaling), M24 (Ubiquitination), M25 (Sugar Metabolism), M19 (Angiogenesis), M12 Cytoskeleton, M39
187 (Translation Initiation), M21 (MHC/Immune), M38 (Heat Shock), M43 (Ribonucleoprotein), M12
188 (Cytoskeleton), M3 (Myelination) and M17 (Translation). Modules showing strong preservation and
189 shared DEPs with decreased levels are M22/M5 (Postsynaptic Density), M1 (Synaptic Transmission), M4
190 (Synapse), M2 (Mitochondria) and M33 (Hormone Secretion). Discordant changes are observed in M9
191 (Golgi), M44 (Viral Transcription), M29 (Glycosylation) M28 (Ribosome/Translation), M23 (GTPase
192 Activity), M34 (GTP Binding), M8 (Protein Transport), M30 (Proteasome), M16 (RNA Processing), and

193 M20/M13 (RNA Splicing). Examples of the cross-species correlations observed between all proteins within
194 individual modules detected between the human AD proteome and the 18M CRND8 proteome are shown
195 in Figure 2G and Figure S2. These correlations range from robust and significant (M42, M11, M4) to
196 modest but significant (M7, M25, M2) to absent (M29).

197 **Human AD protein modules show increased magnitude of change in aged CRND8 brains.**

198 The human proteome and modular network included brains of individuals who had no reported
199 cognitive decline yet neuropathologic criteria of AD. These were referred to as asymptomatic AD (Asym
200 AD). Here we assessed the synthetic eigenprotein levels in the three CRND8 cohorts to evaluate how the
201 overlapping mouse proteins within these modules change over age and how they compare to the modular
202 eigenprotein changes in human Asym AD, and AD (Figure 3 and Figure S3). These data show that across
203 many modules there is an increase in the magnitude of the eigenprotein change with preserved
204 directionality as CRND8 mice age (e.g., M42, M11, M21, M7, M1, M9). Other modules show different
205 patterns of change in the cohorts. For example, M15 (Kinase activity) and M2 (mitochondria) show
206 increased eigenproteins in the 6M cohort and then decreased eigenprotein in the older cohorts, whereas
207 M3 (Myelination) shows a decreased eigenprotein at 6M and then increased at later timepoints. Such
208 data demonstrate that the DEP changes observed often show progressive changes over the age range
209 studied and reveal complex relationships between age, pathology, and proteome changes.

210 **Correlations between Protein and RNA changes in the 18M CRND8 brains.**

211 In human brain, the overall correlation between changes in mRNA and protein levels between AD and
212 control brains is weak [9]. Here we directly compared the protein and RNA levels in the 18M CRND8 cohort.
213 Analyzing the correlation between the changes in 9319 common gene products detected in the 18M
214 CRND8 vs non-Tg proteome at the protein and mRNA levels (Figure S4A) reveals a weak correlation, which
215 is on par with the overall correlation observed in the human brain (protein vs RNA changes in AD vs Control
216 DLPFC) [9]. However, when these data are analyzed within the framework of the protein modular networks,
217 a more complex relationship between changes in mRNA levels and protein levels is observed (Figure S4B-
218 D, Figure S5). For example, within M42 there is no correlation between protein and mRNA levels in either
219 human or mice. However, for modules M11 and M21 there is robust and highly significant correlation
220 between protein and mRNA levels in the CRND8 mouse brain. A more modest, but still highly significant,
221 correlation is observed in the same modules in human AD brain.

222 **Validation of the proteome changes -focus on M42.**

223 We have taken a multifaceted approach to validate the protein changes observed with a major focus
224 on M42 proteins, the module with the most robust changes in CRND8 and strongest correlations between
225 mice and human brains. We also included studies of additional DEPs identified only in the CRND8
226 proteomes that based on biological inference relating to the protein being secreted, a component of the
227 ECM, and known or inferred (based on homology) binding to heparan sulfate (HS) or heparan sulfate
228 proteoglycans (HSPGs) likely had biological roles relevant to M42. We thus refer to this group of proteins
229 as M42+. Several additional DEPs, which showed a log2 Fc >1 in the 18M cohort (Ctss, S100a6, Rev3l),
230 were also targeted in this validation even though they had no obvious links to M42 biology. There was a
231 manifold rationale for the primary focus on M42+ proteins. First, M42 was strongly associated with both
232 core pathological features of AD and cognitive decline and both APOE and APP/Aβ were present in the
233 network. Second, M42, as shown above, was the most conserved module between human AD and CRND8
234 mice. Third, with a few notable exceptions, protein changes appeared to be dissociated from changes in
235 RNA, implicating possible disruptions in proteostasis. Fourth, many M42 proteins show the largest log2 Fc
236 between AD and control brain and in many cases even more striking log2 Fc changes in CRND8 mice.
237 Finally, M42 proteins, represent a mix of DEPs, several with links to AD and amyloid pathology, but others
238 with little or no previous links to AD and amyloid.

239 **Mdk and Ptn co-accumulate with Aβ in plaques and CAA.**

240 We focused initial validation studies at the brain tissue level, as successful detection of the DEP *in situ*
241 would enable us to put the protein changes in pathological context. As exemplars of these studies, we
242 highlight work on midkine (Mdk) and pleiotrophin (Ptn). Mdk and Ptn are homologous small secreted
243 signaling molecules known to interact with HS/HSPGs and signal through a set of overlapping receptors
244 (Sdc1-4, Ptprz1, Ptprb, Lrp1, Ncl, and Integrins α4β1, α6β1, α5β3) [31,32]. In the TMT-MS data, Mdk is
245 significantly increased in all three cohorts studied (log2 Fc) and has the largest log2 Fc of any DEP in the
246 6M cohort, whereas Ptn shows significant increases in the 12 and 18M cohorts. Neither mRNA is altered
247 in bulk transcriptomic studies of human AD brain or APP CRND8 mice brains, though the mRNA levels
248 (Fpkm) are significantly higher for Ptn than Mdk in both human and mouse brain. Select Mdk/Ptn
249 receptors are also altered at the protein level in human AD, CRND8 or both. For example, Sdc2 and Sdc4
250 are significantly increased in AD and CRND8 brains; Ptprz1 is significantly downregulated in CRND8 brains;
251 Lrp1 is significantly upregulated in AD and CRND8 brains; one isoform of Ncl is decreased in 18M CRND8
252 mice; Itga4 and Itgb4 are increased in both CRND8 and AD; Itga5 and b3 are increased in CRND8 mice
253 (Table S1).

254 Immunostaining for Mdk or Ptn shows both exhibit a high degree of overlap with Aβ in CRND8 mice
255 (Figure 4A) and in human brain (Figure 4B). Not only do Mdk and Ptn co-localize to plaques (Figure 4A),
256 but they also co-localize to Aβ amyloid in blood vessels associated with CAA, which is most easily observed
257 in CRND8 in the meningeal vessels of the cerebellum (Figure 4A). In humans, MDK and PTN are detected
258 in both plaques and CAA deposits (Figure 4B). Though both Ptn and Mdk are detected in plaques, they
259 show distinct staining within the cored plaques (Figure 4B-D). Mdk is more prominent in the center of the
260 plaque core in mice and intensity of staining decreases towards the plaque periphery (Figure 4C). Ptn
261 staining is almost the mirror image of Mdk, and it is localized more on the periphery of the fibrillar plaque.
262 In many plaques Ptn does not stain the center where Mdk is most strongly localized (Figure 4C, D). In
263 contrast, in humans, though MDK is more intensely detected in the plaque center, the entire plaque is
264 typically stained, and PTN diffusely stains the fibrillar plaque (Figure 4B). In CAA in the CRND8 mice, both
265 Ptn and Mdk non-homogenously label amyloid deposits detected by Thioflavin S (Thio S) (Figure 4D). In
266 vessels there are some areas where Ptn staining does not overlap with Thio S staining, this might be
267 attributable to expression in pericytes, as Ptn is highly expressed in these cells. Further, staining of Mdk
268 and Ptn in CRND8 mice brains shows co-localization with plaques from 3-12M, as well as staining of
269 plaques in numerous lines of APP transgenic mice (Figure S6A).

270 Western blot analysis of 8M Urea extracts from 20M CRND8 mice brains shows an almost qualitative
271 accumulation of both Mdk and Ptn in both male and female CRND8 brains, relative to the non-transgenic
272 lines, suggesting that TMT-MS methodology may underestimate the true fold change in protein levels
273 (Figure S6B) [33]. As a characteristic feature of Aβ deposited as amyloid is lack of solubility by strong
274 detergent extraction. We examined the crude solubility profiles of Mdk and Ptn in CRND8-Tg brains
275 sequentially extracted with TBS, RIPA, 2% SDS and 8M Urea (Figure S6C). Though relatively low levels of
276 Mdk and Ptn are detected in the TBS and RIPA extracts, the largest amounts were present in the 2% SDS
277 fraction and none was detected in the 2% SDS insoluble urea soluble fraction. Notably, the relative
278 proportion of Mdk or Ptn appearing in each extraction was similar in both the CRND8 Tg and non-Tg brains.
279 This lack of change in gross solubility as the proteins accumulate suggests that they are not undergoing
280 an amyloid-like structural change, which is typically associated with detergent insolubility [34].

281 **Validation of additional M42+ DEP changes**.

282 We initially screened many commercially available antibodies to proteins in M42, few of these
283 antibodies worked in paraffin embedded tissues (Tables S11, S12). We thus, generated many new rabbit
284 polyclonal antibodies. Data showing these antisera can detect the target protein, is provided in Figure

285 S8A. In mice, we evaluated antibody staining of Tg and non-Tg brains in formalin, paraformaldehyde, and
286 ethanol fixed sections. As shown in Figure 5A, we find that many of these antibodies stain amyloid plaques
287 in CRND8 mice (non-Tg controls are shown in Figure S7A). These suggest that many M42+ proteins
288 accumulate, at least in part, due to sequestration within plaques. In mice, a curious feature of these
289 studies is that the localization of the proteins with the plaques is often morphologically distinct. Slit2, Vtn,
290 Olfml3, Ndp, Rev3l, Ntn1, Hhipl1, Bmp6, Ctss, Frzb, Sema3e, Smoc2 and Nog are preferentially localized
291 within the plaque center as observed for Mdk. Col25a1 and Dmp1 appear in the more peripheral regions
292 of the fibrillar plaque akin to Ptn. Another subset shows more diffuse homogenous staining of the plaques
293 (e.g., Vtn, Sdc4, S100a6). Still others show a patchy, nonhomogeneous, staining of the plaques (e.g., Hgf,
294 Spock1, ApoD, Egfl8, C1qTnf4, Slit3), which may in part be attributable to staining of dystrophic structures
295 around or within the plaque. In addition, we find that fixation conditions can dramatically impact the
296 staining pattern observed and that the effects of fixation are antibody dependent (Figure S7B). Dual
297 labeling studies with Aβ or Thio S and a subset of these proteins reinforce the different location within
298 the plaque of select M42 proteins. Finally, except for Mdk, Col25a1 and Ptn which appear to stain most
299 non-diffuse plaques, we note that only a subset of the plaques detected by Aβ immunohistochemistry is
300 stained (Figure 5A). As the anti-Aβ monoclonal used for staining has subnanomolar affinity, additional
301 studies will be needed to further evaluate the extent of co-localization using additional immunologic
302 reagents.

303 CAA Aβ deposition is easily assessed in the cerebellum of 12M CRND8 mice. In Figure 5B we show the
304 subset of antibodies that stain CAA. In addition to Mdk and Ptn a smaller group of the M42+ DEPs are
305 detectable in CAA Aβ deposits (Col25a1, Olfml3, Htra1, Smoc1, Sulf1, Frzb, Egfl8, C1qtnf4, Smoc2, Nog).
306 All of these can also be shown to co-localize with Thio S staining in the vessels (Figure S6C).

307 Several M42 CRND8 DEPs show staining adjacent to the fibrillar plaque (Figure 5C). Spock3, Bmp6, Frzb,
308 and Nog, show staining patterns highly consistent with the classic dystrophic neurites (DN) often
309 visualized with anti-ubiquitin or other DN markers. In contrast Col25a1, Vtn, Rev3l, Sdc4, S100a6, Egfl8,
310 Spock1, and Flt1 show peri-plaque staining that is distinct from the classic DN pattern. In addition,
311 selective staining of reactive astrocytes is noted for Htra1, Sulf1, Sfrp1, HhIpl1, Spock3, Sema3d, and
312 Smoc2 (Figure S7D).

313 We have been able to localize a smaller subset of the M42 proteins in AD postmortem brain tissue
314 (Figure 6). EGFL8, C1QTNF4, COL25A1, HGF, SDC4, NTN1 and SMOC2, all show staining in plaques (Figure
315 7A). We would note that EGFL8 was not detected in the TMT-MS studies in human brain, but Egfl8 was
316 detected as a DEP in CRND8 mice. OLFM3, SPOCK3, SPOCK1, show staining of dystrophic structures around
317 plaques (Figure 7B). SULF1, SFRP5 and SFRP1 stain reactive astrocytes (Figure 7C).

318 In supplementary Table S9, we compile the staining observed and annotate our findings versus previous
319 studies in the field, we also classify the cell type expression observed for the proteins that we detect in
320 these immunohistochemistry studies using data available at the Allen brain atlas [35]. The extended M42+
321 members appear to arise from multiple cell types representing all major brain cell types. This is consistent
322 with the biological annotations of M42 (matrisome, ECM) and likely reflects extracellular processes
323 regulating or responding to abnormal extracellular protein accumulation. Many of the mRNAs encoding
324 these proteins are expressed at low levels (< 5 Fpkm). Further within the M42 DEPs only Olfml3, which is
325 selectively expressed by microglia, shows significant increase in mRNA levels in the 18M RNAseq data. In
326 previous RNAseq studies of CRND8 mice brains, we have found that Olfml3 mRNA levels are increased at
327 6, 12 and 20M. Ctss and S100a6 also show significant increases in mRNA levels, but as noted previously,
328 are not part of the core M42 module, and the associated increase in both mRNA and protein likely reflects
329 reactive gliosis. In addition to these immunohistochemical studies and data on Mdk and Ptn, we can also

330 demonstrate increases in the brains of older CRND8 mice of Vtn, Htra1, Smoc1, Frzb, ApoD and Nog
331 western blot analysis of the CRND8 mice (Figure S8B).

332 **Mdk and Ptn overexpression increase parenchymal amyloid and CAA in CRND8 mice and accelerate**
333 **amyloid aggregation in vivo.**

334 Given the robust data showing the co-localization of Mdk and Ptn with both plaques and CAA Aβ
335 deposits and the early increase observed in the 6M TMT-MS data for Mdk, we evaluated the impact of
336 rAAV-mediated overexpression of Mdk or PTN on amyloid deposition in 2 cohorts of CRND8 mice. The
337 first study examined the impact of P0 ICV injection of rAAV2/8 vectors encoding Mdk or PTN after 3
338 months of age, the second at 6M of age. In both cohorts, similar impacts are observed, for brevity we will
339 primarily describe the 6M analysis here (Figure 7). The 3-month overexpression data is presented in Figure
340 S9A-C. Widespread over expression of Mdk and PTN is detectable in the brain in both cohorts. Even in the
341 small early compact plaques in the 3M cohort it is possible to detect Mdk and PTN staining within the
342 plaques. Mdk and PTN both increased parenchymal plaques (Figure 7A) and CAA (Figure 7B) as assessed
343 by immunohistochemistry. In previous studies of CRND8 mice we have not noted sex differences in
344 amyloid deposition or other phenotypes, though these studies were not designed to be powered to detect
345 sex differences, post hoc analyses do not reveal any major impact of sex. Both also increased Aβ levels in
346 SDS and Formic Acid (FA) fractions, but not in the RIPA fractions (Figure 7C). These studies establish that
347 overexpression of either Mdk and Ptn can accelerate amyloid deposition into fibrillar plaques and CAA in
348 two cohorts. In the 6M cohort, we also evaluated reactive gliosis using IHC for Gfap and Iba1. Both Mdk
349 and PTN increased astrocytosis assessed by Gfap staining, and PTN increased microgliosis as assessed by
350 Iba1 staining. Mdk overexpression also increased Iba-1 staining but this elevation was not significant
351 (Figure S9D). We also assessed the impact of recombinant PTN and MDK on amyloid aggregation *in vitro*
352 using standard THT fluorescence assays (Figure 7D). Both reproducibly and significantly accelerated Aβ42
353 aggregation. Mdk also increased Aβ40 aggregation, whereas only a small impact for PTN on Aβ40
354 aggregation was observed. End of assay total THT fluorescence was also increased in all cases except for
355 the Aβ 40 PTN study, suggesting increased β-sheet formation.

356 **Select M42+ proteins bind to Aβ fibrils and an amyloid derived from a non-human peptide, non-**
357 **homologous peptide.**

358 Many M42 proteins are known or can be inferred by study of other family members to be HS/HSPG
359 binding proteins. We have performed limited studies on heparin interaction with Mdk and Ptn and can
360 confirm strong interactions with immobilized heparin (Figure S10). We evaluated a larger number of these
361 for the potential to interact with Aβ42 fibrils and a non-homologous amyloid formed from a 12 amino acid
362 adenovirus shaft peptide (AVS fibrils) [36,37]. For these studies we turned to a simple amyloid-pulldown assay
363 to screen for interactions with insoluble amyloids [38-40]. As M42 proteins contain numerous intrachain
364 disulfide bonds and other post translational modifications (PTMs), we expressed a subset of these proteins
365 in HEK293 cells and collected conditioned media containing the secreted proteins. Aβ42 fibrils or the AVS
366 fibrils were then incubated and spun down to evaluate potential interactions with amyloid structures. For
367 the subset of proteins which we were able to detect in the media, we can show that APOE4, Mdk, Vtn,
368 Ptn, Olfml3, Htra1, Smoc1, Sulf1, Frzb, ApoD, C1qTnf4, Smoc2, and Nog bind both Aβ42 and AVS amyloids
369 (Figure 8A). Sfrp1 is a notable exception as we only observed it binding to Aβ fibrils in this assay. Such
370 studies provide initial data that many of these proteins bind a generic amyloid structure.

371 **PTN and MDK are colocolized with transthyretin (TTR) amyloid in the human heart.**

372 Though the amyloid pulldown assay shows the ability of multiple M42 proteins to interact with a
373 generic amyloid structure, we wanted to orthogonally test this hypothesis by evaluating whether some of
374 these proteins may accumulate in other human amyloid diseases. For these studies we have focused on
375 in *situ* detection of MDK and PTN, as the antibodies for these robustly detect these proteins in formalin

fixed human tissues. As shown in Figure 8B we find that both MDK and PTN co-localize with TTR amyloid in the heart (the third most prominent human amyloid disease) [41]. A series of TTR cardiac amyloid cases show consistent co-localization of both MDK and PTN with the TTR amyloid fibrils (data not shown).

DEPs in CRND8 mice in the context of AD genetic studies.

Previous transcriptomic studies of APP mice have suggested that very highly upregulated DEGs are enriched for genes under AD GWAS loci or known genetic risk factors for AD [42]. To examine whether DEPs in the CRND8 mice might provide similar insights, we integrated data from three previous GWAS studies of AD to evaluate whether DEPs in CRND8 mice reflect some aspects of the genetic architecture of human AD (Table S1, Figure 9A) [43-45]. Integration of the 18M CRND8 TMT-MS data with these AD genetic studies show that many established AD risk genes and prioritized GWAS loci (e.g., *APOE, BIN1, TREM2, CLU, SORL1, ACE, ADAM17, SORT1, INPP5D)* are DEPS in the 18M CRND8 mice. Abca1, recently implicated as genetic risk factor for AD, is also a DEP in both the 12m and 18M CRND8 cohorts [46]. Notably multiple M42+ proteins besides APOE show nominal significance in the GWAS studies including *COL25A1, SMOC1, HTRA1, DMP1, MDK, SDC4, SPOCK2, NXPH1*, and *C1QTNF4*, the latter of which lies in the *CELF1* locus and shows the highest p value of M42 members for AD association. Finally, we note that Grn, Sppl2a, Tmem106b and Notch3 are all DEPs in the 18M CRND8 proteome. *GRN* and *TMEM106B* are genetically associated with FTD-GRN, and SPPL2A is known to cleave TMEM106B potentially linking it to the biology of FTD-GRN [47,48]. Further, *NOTCH3* mutations are associated with CADASIL [49]. Given debate over genetic pleiotropy or inclusion of non-AD dementia in the large GWAS studies (clinical phenocopy inclusion) [50,51], these data suggest there are biological links between proteins implicated in FTD and CADASIL and amyloid pathology in AD. A final intriguing observation from these data is that multiple proteins near the *APOE l*ocus are DEPs in the CRND8 mice. There is conservation of the extended *APOE* locus between mice and humans, and such data may point to complex biology around the *APOE* locus that could contribute to AD risk.

DEPs in CRND8 mice in the context of AD CSF biomarker studies

We also evaluated the 18M cohort CRND8 DEPs in the context of human AD CSF biomarker studies, for this integration we chose a recent data set in which AD and control CSF were compared using a highly similar proteomic pipeline for both TMT-MS data generation and analysis [52]. However, we would note that this data shows significant overlaps with other large scale proteomic analyses of AD versus control CSF [52-62]. Of the 1839 in the human CSF proteomes 257 of these are significantly altered and of these 62 are significantly changed in the 18M CRND8 mice brains. 39 of these changes are congruent in directionality between the mouse brain and human CSF and 23 are discordant in directionality (Figure 9B, Table S13). Notably, 29 of the 18M DEPs are significantly altered in the same direction in human AD brain as in the mouse model, irrespective of direction of change in CSF, and only 5 show a discordant directionality with human AD brain change. Overall, these data support a hypothesis that some significant and reproducible changes in human CSF may reflect changes in the brain related to amyloid.

DISCUSSION

By integrating newly generated deep TMT proteomic data from CRND8 mice brains with previously generated large-scale data from human AD brain, we have begun to define the Aβ/Aβ amyloid "responsome" that is partially conserved between this mouse model of Aβ deposition and human AD [9,10]. Within select protein modules, DEP and overall protein changes are highly concordant; however, the presence of multiple discordant protein network modules and modules that are simply not concordant, reinforce the concept that these transgenic mice are incomplete models of AD [9,10,30]. Nevertheless, these data and analyses establish a paradigm for contextualizing changes that occur in human AD and provide an unbiased view of the degree to which a model system reflects, or does not reflect, the complex proteomic changes in the human AD brain. Indeed, there is much debate about what defines a "better

422 mouse model", these data suggest that a comparative omics approach particularly those that analyze the
423 proteome, can provide a less biased manner to address this question [63,64].

424 As discussed in detail below, we have primarily focused validation studies on M42, the most
425 concordant module between human and mice, a module that in humans correlates best with amyloid and
426 tau pathologies and strongly correlates with cognitive status [9,10]. However, we document other
427 concordant modules and discordant or non-concordant modules as well. This modular framework may
428 offer initial insights into what aspects of AD pathology the mice mimic and what modules they do not, but
429 validation and contextualization of these will be required to better understand how these modules fit into
430 the complex architecture of AD pathology [2].

431 As CRND8 mice do not show overt neuronal loss [65], the finding that numerous modules relating to
432 neuronal and synaptic function (M1, M4, M5, M22, M33) show conservation is intriguing. Numerous APP
433 models, including CRND8 mice have been shown to have synaptic alterations[66-68], and in many cases these
434 alterations occur at relatively early ages [63,69,70] . Notably, our data show a progressive impact on synaptic
435 protein modules as assessed by eigenprotein levels. However, for the majority of human and mouse
436 proteins in these modules the magnitude of change as assessed by TMT-MS is quite small. Of interest,
437 neuritin (Nrn1) and small glutamine-rich tetratricopeptide repeat-containing protein β (Sgtb) which are
438 implicated in cognitive resilience to AD pathologies are both consistently downregulated DEPs in the older
439 CRND8 cohorts [71,72] . Nevertheless, these studies highlight the disconnect between Aβ amyloid deposition
440 models and human AD, as these models do not progress to an overt neurodegenerative state and lack
441 tangle pathology.

442 Several of the eigenprotein changes in the CRND8 brains assessed in the context of the human AD
443 modular framework show a consistent alteration in directionality and an increased separation between
444 Tg and non-Tg from 6M to 18M (e.g., M42, M28, M11, M12, M4, M23). Other modules, such as M3
445 (Myelination, down at 6M and up at 12/18M) and M15 (Kinase Activity, up at 6M, down at 12/18M) show
446 discordant directionality across the cohorts. Notably, for myelination there is evidence in other APP mice
447 models that there are temporal changes in oligodendrocyte lineages and myelin that may be consistent
448 with this data [73-75] and, more generally, there is growing evidence for oligodendrocyte lineage and myelin
449 alterations in AD [76-78] and other tauopathies [76,79]. However, these specific proteomic changes need to i) be
450 validated in this model and ii) further contextualized by refining these proteomic and validation studies
451 through inclusion of a broader cross-sectional series of ages and additional models with differential
452 temporal sequence of amyloid deposition.

453 We also may need to refine how we view concordant, non-concordant, and discordant changes
454 between the model and human protein modular networks. A good example of this is M21, the
455 MHC/immune module, though the correlation within this module not significant, in general most proteins
456 in this module are upregulated in both human and mice, however, in humans the protein upregulation of
457 immune module is much less robust, although transcriptome upregulation is significant in both human
458 and mouse brains in the context of AD [11,80]. This data suggests that mice respond to amyloid deposition
459 with a more robust innate immune response than humans, perhaps because of i) the compressed time
460 frame for amyloid deposition in these models ii) impacts of aging on the human brain which may alter
461 baseline immune status [81,82] or iii) inherent interspecies differences in synthesis and clearance of these
462 proteins.

463 More broadly, future studies will be needed to guide our understanding of the proteomic changes in
464 mouse models that mimic human AD and those that do not. Similar deep proteomic studies on tau mice
465 might inform on protein modules more related to neurofibrillary pathology. We also should consider that
466 discordant modules in mice such as upregulation of M9 (Golgi) that includes ER to Golgi trafficking

467 proteins and lysosomal hydrolases and proteases, might serve protective functions that could impact the
468 appearance of downstream pathologies and overt neurodegeneration in the models [83,84].

469 To build a highly significant deep TMT-MS proteome from human AD brain required hundreds of
470 samples [9,10], in contrast we find that using small cohorts of CRND8 mice that we can generate highly
471 reproducible data. Further by looking at cohorts of different ages we can infer changes that might be
472 attributable to transgene overexpression versus increasing level of Aβ deposition. The CRND8 mouse is a
473 robust and aggressive model of amyloid deposition [65]. CRND8 mice have shown a very reproducible
474 phenotype across many studies, with no easily discernable sex-based impacts on pathological phenotypes
475 [39,68,85]. Notably our data is highly consistent with previously published proteomic data on 5X FAD mice,
476 but because of the depth, multiple ages, and larger groups sizes we appear to be cataloging a larger
477 number of proteomic changes [14,29]. From a translational point of view, these data reinforce the notion
478 that preclinical studies probing impacts of therapies targeting amyloid or pathologies downstream of
479 amyloid should not just be tested in younger mice with limited amyloid deposition but should also be
480 evaluated in the context of impacts on older mice with extensive amyloid deposition.

481 For the reasons described previously, we focused validation efforts on the M42+ module. We had
482 known from previous studies that several of the core M42 members including APP, APOE and COL25A1
483 accumulate in amyloid plaques [86-90]. Here we provide additional evidence that many of the core human
484 M42 module are present in plaques in mice (Mdk, Ntn1, Smoc1, Sdc4, Olfml3, Sfrp1, Spock1, Frzb, Htra11,
485 Slit2), we also show that many other proteins emerging from the CRND8 proteome (Vtn, Dmp1, Ndp,
486 Rev3l, Hgf, HHipl1, S100a6, Bmp6, Ctss, Sema3e, Apod, Egfl8, C1qtnf4, Smoc2, Nog and Slit3) are also
487 present in the plaques in mice. A subset of these M42+ proteins also are found in CAA, others in dystrophic
488 processes around plaques and others in reactive astrocytes. We have successfully localized a smaller
489 number of these proteins to plaques and other pathological features in humans. Given the conserved
490 protein changes in mice and humans seen by proteomic analyses, this discrepancy may be attributable to
491 fixation conditions and epitope exposure, which may differ between mice and humans. Our current data
492 showing how fixation conditions can alter the pathologies detected by select antibodies in mice, highlight
493 the importance of developing multiple high-quality antibodies to extend and further validate these initial
494 pathological assignments.

495 Notably, two proteins Egfl8 and Hgf were only detected and present as DEPs in the CRND8 proteome,
496 but both HGF and EGFL8 appear to be plaque components in humans. Such findings serve as an exemplar
497 of the power of utilizing a model system to inform on human pathology. Further, these studies broadly
498 serve as a strong affirmation of the power of WGCNA to inform pathobiology of a complex disease [91].
499 Indeed, M42 is the most conserved protein module network between CRND8 mice and human AD and
500 shows the strongest correlation with amyloid and cognitive decline in humans [9,10]; these validation studies
501 highlight its direct links relevant to amyloid pathology or response to amyloid pathology.

502 Some of the more nuanced data emerging from these validation studies relate to the unique patterns
503 of localization of these proteins within fibrillar plaques. This feature has been most rigorously studied for
504 Mdk and Ptn which show unique and reciprocal distributions in the CRND8 plaques, and distinct
505 distributions in human plaques. Overall, there appear to be four general patterns of staining. The first
506 pattern is like Mdk, whereby the core of plaques is labeled most intensely, the second pattern, like Ptn,
507 shows more intense peripheral staining of the plaque, a third pattern, such as seen with Sdc4, shows a
508 very homogenous staining of the entire plaque and a fourth pattern, such as seen with Egfl8, shows patchy
509 non-homogenous staining. Such data along with data showing that only a subset of parenchymal plaque
510 associated proteins are detected in CAA, raises many questions about the nature of these interactions
511 and the differences and similarities of not only CAA and plaque amyloid, but also even the concept that
512 structural interactions may vary even within a single plaque. Direct studies of the human CAA proteome
513 have also found increased levels of OLFML3, PTN and HTR1A, along with other known CAA components

514 (e.g., APOE, CLU, APCS) [92,93]. Further study of CAA and cerebral autosomal-dominant arteriopathy with
515 subcortical infarcts and leukoencephalopathy (CADASIL) vessels' proteomes shows overlap with each
516 other, but also reveal extensive and broad overlap with many M42 DEPs [92,94]. As Notch3 and Htra1 are
517 increased DEPs in CRND8 mice, and we have been able to detect Htra1 in vessels, further study of CAA
518 and its impact on the proteome is warranted. Indeed, there is emerging evidence that sequestration of
519 HTRA1, a serine protease, with NOTCH3 in CADASIL leads to HTRA1 loss of function and accumulation of
520 select HTRA1 substrates [92,94]. Such data could account for the similarities between CADASIL and cerebral
521 autosomal recessive arteriopathy with subcortical infarcts and leukoencephalopathy (CARASIL), the latter
522 of which is caused by heterozygous loss of function mutations in *HTRA1*. Such data suggest that HTRA1
523 accumulation in CAA and in plaques might have similar impacts and contribute to CAA driven vascular
524 dysfunction in AD.

525 The data showing that overexpression of Mdk or PTN in the CRND8 brain results in increased CAA and
526 parenchymal Aβ amyloid suggests that these proteins have a direct impact on amyloid deposition, and
527 therefore represent novel therapeutic targets in AD. As both proteins can accelerate aggregation of Aβ
528 and bind preexisting amyloid fibrils *in vitro* we hypothesize they act as amyloid chaperones likely directly
529 impacting the rate of Aβ aggregation. However, Mdk is known to have impacts on myeloid cell lineages
530 and its co-accumulation in plaques could theoretically impact microglial mediated clearance either
531 through gain or loss of function [95,96] Ptn, which signals largely through the same receptors as Mdk, could
532 have similar impacts as well [97]. Thus, it is also plausible that these proteins may also influence cell
533 mediated clearance of Aβ. More broadly, additional studies will be needed to evaluate the impact of not
534 only Mdk and Ptn but the many co-accumulating proteins on not amyloid deposition itself, but also the
535 cellular responses to the deposits. Though a previous study had noted that a Mdk knockout crossed into
536 an APP transgenic line resulted in increased amyloid deposition, we would note this data is simply
537 anecdotal [98]. Non-Tg mice Mdk and Ptn knockouts were studied, and claimed to increase amyloid
538 deposition, but in that study the antibody 6E10, which is highly selective for human Aβ was used to stain
539 "plaques". Thus, such results are likely artifactual.

540 HS and HSPGs along with chondroitin sulfate proteoglycans (CSPGs) have long been implicated in the
541 biology of AD and other amyloid deposits [99]. HS and select HSPGs core proteins (e.g., HSPG2, ACAN) have
542 been shown to accumulate in plaques or dystrophic neurites. HSPGs have also been reported to accelerate
543 Aβ aggregation and mediate internalization of extracellular tau [100]. In these proteomic studies, we detect
544 HSPG2, ACAN, and multiple CSPGs but they are minimally altered in either mice or the human AD
545 proteome (Table S1). In contrast, in human AD, GPC4,5; SPOCK1-3; and SDC2,4 are much more robust
546 DEPs and many of these are core M42 module members. In CRND8 mice Gpc1,5; Spock1-3 and Sdc2,4 are
547 also robust DEPs (Table S1). Further, gene ontology strongly demonstrates heparin and glycosaminoglycan
548 biology related biological processes upregulation in aged CRND8 mice brains (Figure 1).

549 We have not systematically evaluated heparin binding as a surrogate for HS/HSPG binding of many of
550 the M42+ proteins studied here, but we find MDK and PTN secreted from mammalians cells bind robustly
551 to heparin. We do find that a subset of the M42+ proteins secreted by human embryonic kidney 293
552 (HEK293) cells bind Aβ42 amyloid and a non-human, non-homologous amyloid fibrils [36,37]. This subset of
553 M42+ proteins was pragmatically chosen simply based on proteins which were secreted and detectable
554 in the media of transiently transfected HEK293 cells. This data led us to explore whether MDK and PTN
555 might be components of peripheral amyloids and we find both accumulate in TTR cardiac amyloid.
556 Neither have been previously detected, even in extensive laser capture proteomic studies of cardiac
557 amyloid deposits [101]. As HS/HSPGs are common components of amyloids, these studies suggest that there
558 may be very complex multipartite structural interactions between amyloid, HS/HSPGs and these co-
559 accumulating proteins which may prove challenging to unravel.

560 Given the intensive studies of both Aβ amyloid and peripheral amyloids, it is somewhat surprising that
561 we and others are finding numerous additional proteins co-accumulating with amyloid [14,28,29,101,102]. In
562 both the human and mouse studies brain tissue was extracted with 8M urea; thus, we are studying the
563 total detectable urea solubilized proteome and not the detergent insoluble proteome. Indeed, for Mdk
564 and Ptn in mice brains we find no gross change in solubility, despite the large increase in the Tg mouse
565 brains. Following SDS-extraction, no residual protein is detected in the Urea fraction. These initial
566 solubility studies likely explain why many of these proteins are not detected in detergent insoluble
567 fractions typically used to isolate amyloid, they simply may not be there.

568 Our current data and data from others reveal numerous proteins that co-deposit with Aβ amyloid.
569 Further, given the large number of proteins showing age progressive increases in the CRND8 mice brain,
570 it is highly likely that over time many additional proteins will be found to accumulate with Aβ amyloid and
571 perhaps other disease relevant amyloids as well. Indeed, two recently identified components of Aβ
572 plaques, Pycard and Mfge8, are increased DEPs in our data, but in the 18M old CRND8 cohort rank 296th
573 and 300th in terms of log2 Fc [103,104]. In the human AD proteome, PYCARD is significantly increased (log2
574 Fc=0.06), and MFGE8 is detected but not increased. Cleary not all proteins upregulated will be
575 components of plaques, but these data clearly point to biology of amyloid that is much more complex
576 than previously appreciated, and that the response to amyloid deposits may also be equally as complex.

577 Despite thousands of studies and numerous hypotheses, there is ongoing debate as to how amyloid
578 or Aβ aggregate pathology drives cellular dysfunction that leads to the neurodegenerative phase of AD
579 [2,7,8]. More generally, this debate extends to all amyloid disorders and how amyloid accumulation causes
580 tissue damage [34,41,105]. Indeed, extensive efforts have been made to identify more toxic species or
581 conformers (e.g., oligomer, protofibril, dimer, specific fibrillar conformer) [106]. Our current data, along with
582 previous studies of proteins that co-accumulate with amyloid, offer an alternative hypothesis to the
583 concept that amyloid or some distinct amyloid-like aggregate is a direct toxin [70,107]. We term this the
584 "amyloid scaffold" hypothesis (Figure S11) and posit that if amyloid deposits can scaffold the accumulation
585 of numerous proteins than perhaps the accumulation of these proteins mediates downstream
586 pathophysiology. Both toxic gain of function and loss of function mechanisms need to be considered.
587 Accumulation of proteins within amyloid deposits could lead to gain of normal function if these proteins
588 retain activity or if such binding activates a novel signaling pathway. Sequestration in the deposit could
589 result in loss of function and reduced levels in the surrounding tissue. If solubility of select proteins
590 accumulating in the amyloid deposit is not changed, then these proteins may retain signaling function.
591 Indeed, many of the proteins we detect in plaques and CAA are known signaling molecules and through
592 either loss or gain of function mechanisms their accumulation could impact dystrophic neurite and
593 reactive glia in the local plaque microenvironment or cells in the vessel wall. In the heart MDK, though
594 shown to have some cardioprotective effects, can also promote intimal hyperplasia whereas PTN have
595 been shown to have angiogenic effects [108-110]. Thus, this hypothesis may have relevance for peripheral
596 amyloidoses as well. There are also intriguing parallels between this concept of amyloid as a scaffold for
597 pathological process and functional amyloids which have been proposed to mediate their biological
598 effects in part through a scaffolding mechanism (reviewed in [111]).

599 As with many biologic responses, it is important to consider that the accumulation of proteins in the
600 plaque is not simply a bystander effect, but part of the response to amyloid as a danger associated
601 molecular pattern [81,112]. The amyloid "scaffold" and amyloid (or oligomer) as "direct toxin" hypotheses are
602 not mutually exclusive. Amyloid fibrils and oligomers are potent activators of microglia and myeloid cells
603 and soluble oligomeric and protofibrillar aggregates can mediate many impacts on different cells [30,70].
604 Proteins that interact with an amyloid or oligomer structure could be actively involved both in clearance,
605 coating, and neutralization of the structure to reduce toxicity, or some combination of these. Other

606 components may simply be bystanders, at least with respect to impacts on amyloid deposition, but once
607 present could still mediate pathology by altering signaling gradients. er.

608 There is extensive data that APOE and CLU interaction with Aβ/Aβ amyloid deposits alters the local
609 cellular response, and influence amyloid deposition itself[86-88,113,114] Because of their genetic association
610 with AD, they are also considered therapeutic targets, though it has been challenging to develop
611 therapeutic approaches that modulate APOE or CLU and show robust preclinical disease modifying
612 impacts [115]. We have not yet explored studies in knockout mice, however, overexpression studies suggest
613 that Mdk and PTN, like APOE and CLU, can increase amyloid deposition and both also increase CAA. It will
614 be intriguing to evaluate the impacts of the larger set of proteins that are now being shown to co-
615 accumulate. We might speculate that some will promote amyloid deposition, others might block it and
616 still others might simply bind without altering kinetics of deposition. Our initial data suggest that many of
617 these co-accumulating proteins could be considered as novel therapeutic targets, but additional probes
618 of their biology will be necessary to determine their role in disease and their druggability.

619 Integrating data from genetic studies of AD and the DEPs in the CRND8 mouse brain, reinforces links
620 between many established AD genes or prioritized genetic loci and AD risk genes and regulation of
621 Aβ catabolism and deposition or response to Aβ deposition. This integration also provides an additional
622 criterion that might be considered when prioritizing studies in loci with multiple candidate genes. Indeed,
623 multiple proteins that are within M42, co-deposit with amyloid, or both and show nominally significant
624 associations with AD. Integration of CRND8 proteome with AD CSF biomarkers shows that many proteins
625 significantly altered in human AD CSF are DEPs in the brains of an amyloid depositing mouse model. Again,
626 these data suggest that these CSF biomarkers might reflect the impacts of amyloid pathology on the AD
627 brain. With the approval of immunotherapies that can dramatically impact amyloid deposition it will be
628 intriguing to determine if this subset of CSF AD biomarkers is altered in response to such therapy. Recently
629 SMOC1 and SPON1, two core M42 members have been found to be altered in concert with decreases in
630 Aβ42/40 ratios in the CSF of individuals with dominantly inherited AD [57]. Further, Smoc1 is a highly
631 reproducible highly upregulated AD CSF biomarker [53,57,61,116].

632 In summary, this contextualized understanding of AD and APP mouse model proteomic changes
633 provides insights into the true molecular complexity of AD pathogenesis and informs on biomarkers and
634 therapeutic targets related to amyloid deposition. Though we have i) validated some of the more robust
635 protein changes in the proteomic analyses, ii) provided pathological insight related to a subset of these
636 proteins, and iii) generated initial modeling and biochemical data to support potential pathobiological
637 roles, there is still much to be learned about amyloid and its role in AD pathophysiology and in other
638 amyloid disorders. Clearly, future integrative omic studies can build off and refine these current studies,
639 especially by incorporating models of additional pathologies relevant to AD and other amyloid disorders.

640 **Limitations of the study**

641 We commented on the many limitations of this multifaceted study in the results and discussion, but
642 several overarching limitations are highlighted here. First, the pathological validation studies vary with
643 respect to the confidence in the findings. Classic criteria suggest two antibodies or antisera to two distinct
644 epitopes of the target protein are needed to confirm presence in pathological setting. A subset of the
645 pathological findings is based on a single antibody or antisera. However, we would note that this criterion
646 was often utilized in an era when additional data (e.g., proteomic based) was lacking. Second, we do not
647 have extensive proteomic data from human brains with amyloid deposition prior to the presence of other
648 pathologies. Thus, we have limited our integration of the mouse data to human brain data which has a
649 spectrum of AD pathologies. This fact limits inference as to which proteomic changes in humans are truly
650 amyloid driven. Third, the lack of analyses of a group young enough to lack amyloid deposition or
651 alternatively a manipulation that alters amyloid loads, impose some interpretative limitations on the data

652 with respect to changes driven by amyloid or mutant APP overexpression. Nevertheless, given the
653 multiple layers of orthogonal and integrative data used in this study we believe that this study begins to
654 capture and contextualize proteomic changes in AD and a mouse model of amyloid deposition in a way
655 that will inform downstream studies for many years.

656

657 **REFERNCES**

658 1. Hardy, J., and Selkoe, D.J. (2002). The amyloid hypothesis of Alzheimer's disease: progress
659 and problems on the road to therapeutics. Science *297*, 353-356.
660 2. Golde, T.E. (2022). Alzheimer's disease - the journey of a healthy brain into organ failure.
661 Mol Neurodegener *17*, 18. 10.1186/s13024-022-00523-1.
662 3. Budd Haeberlein, S., Aisen, P.S., Barkhof, F., Chalkias, S., Chen, T., Cohen, S., Dent, G.,
663 Hansson, O., Harrison, K., von Hehn, C., et al. (2022). Two Randomized Phase 3 Studies of
664 Aducanumab in Early Alzheimer's Disease. J Prev Alzheimers Dis *9*, 197-210.
665 10.14283/jpad.2022.30.
666 4. Sims, J.R., Zimmer, J.A., Evans, C.D., Lu, M., Ardayfio, P., Sparks, J., Wessels, A.M.,
667 Shcherbinin, S., Wang, H., Monkul Nery, E.S., et al. (2023). Donanemab in Early
668 Symptomatic Alzheimer Disease: The TRAILBLAZER-ALZ 2 Randomized Clinical Trial.
669 JAMA. 10.1001/jama.2023.13239.
670 5. van Dyck, C.H., Swanson, C.J., Aisen, P., Bateman, R.J., Chen, C., Gee, M., Kanekiyo, M., Li,
671 D., Reyderman, L., Cohen, S., et al. (2023). Lecanemab in Early Alzheimer's Disease. N Engl
672 J Med *388*, 9-21. 10.1056/NEJMoa2212948.
673 6. Golde, T.E., Schneider, L.S., and Koo, E.H. (2011). Anti-abeta therapeutics in Alzheimer's
674 disease: the need for a paradigm shift. Neuron *69*, 203-213. S0896-6273(11)00003-1
675 [pii]10.1016/j.neuron.2011.01.002.
676 7. Murdock, M.H., and Tsai, L.H. (2023). Insights into Alzheimer's disease from single-cell
677 genomic approaches. Nat Neurosci *26*, 181-195. 10.1038/s41593-022-01222-2.
678 8. Long, J.M., and Holtzman, D.M. (2019). Alzheimer Disease: An Update on Pathobiology
679 and Treatment Strategies. Cell *179*, 312-339. 10.1016/j.cell.2019.09.001.
680 9. Johnson, E.C.B., Carter, E.K., Dammer, E.B., Duong, D.M., Gerasimov, E.S., Liu, Y., Liu, J.,
681 Betarbet, R., Ping, L., Yin, L., et al. (2022). Large-scale deep multi-layer analysis of
682 Alzheimer's disease brain reveals strong proteomic disease-related changes not observed
683 at the RNA level. Nat Neurosci *25*, 213-225. 10.1038/s41593-021-00999-y.
684 10. Johnson, E.C.B., Dammer, E.B., Duong, D.M., Ping, L., Zhou, M., Yin, L., Higginbotham, L.A.,
685 Guajardo, A., White, B., Troncoso, J.C., et al. (2020). Large-scale proteomic analysis of
686 Alzheimer's disease brain and cerebrospinal fluid reveals early changes in energy
687 metabolism associated with microglia and astrocyte activation. Nat Med *26*, 769-780.
688 10.1038/s41591-020-0815-6.
689 11. Wan, Y.W., Al-Ouran, R., Mangleburg, C.G., Perumal, T.M., Lee, T.V., Allison, K., Swarup,
690 V., Funk, C.C., Gaiteri, C., Allen, M., et al. (2020). Meta-Analysis of the Alzheimer's Disease
691 Human Brain Transcriptome and Functional Dissection in Mouse Models. Cell Rep *32*,
692 107908. 10.1016/j.celrep.2020.107908.
693 12. Allen, M., Carrasquillo, M.M., Funk, C., Heavner, B.D., Zou, F., Younkin, C.S., Burgess, J.D.,
694 Chai, H.S., Crook, J., Eddy, J.A., et al. (2016). Human whole genome genotype and
695 transcriptome data for Alzheimer's and other neurodegenerative diseases. Sci Data *3*,
696 160089. 10.1038/sdata.2016.89.
697 13. Wang, X., Allen, M., Is, O., Reddy, J.S., Tutor-New, F.Q., Castanedes Casey, M.,
698 Carrasquillo, M.M., Oatman, S.R., Min, Y., Asmann, Y.W., et al. (2021). Alzheimer's disease
699 and progressive supranuclear palsy share similar transcriptomic changes in distinct brain
700 regions. J Clin Invest. 10.1172/JCI149904.

701 14. Bai, B., Wang, X., Li, Y., Chen, P.C., Yu, K., Dey, K.K., Yarbro, J.M., Han, X., Lutz, B.M., Rao,
702 S., et al. (2020). Deep Multilayer Brain Proteomics Identifies Molecular Networks in
703 Alzheimer's Disease Progression. Neuron *106*, 700. 10.1016/j.neuron.2020.04.031.
704 15. Bai, B., Hales, C.M., Chen, P.C., Gozal, Y., Dammer, E.B., Fritz, J.J., Wang, X., Xia, Q., Duong,
705 D.M., Street, C., et al. (2013). U1 small nuclear ribonucleoprotein complex and RNA
706 splicing alterations in Alzheimer's disease. Proc Natl Acad Sci U S A *110*, 16562-16567.
707 10.1073/pnas.1310249110.
708 16. Zhang, B., Gaiteri, C., Bodea, L.G., Wang, Z., McElwee, J., Podtelezhnikov, A.A., Zhang, C.,
709 Xie, T., Tran, L., Dobrin, R., et al. (2013). Integrated systems approach identifies genetic
710 nodes and networks in late-onset Alzheimer's disease. Cell *153*, 707-720.
711 10.1016/j.cell.2013.03.030.
712 17. Rayaprolu, S., Higginbotham, L., Bagchi, P., Watson, C.M., Zhang, T., Levey, A.I., Rangaraju,
713 S., and Seyfried, N.T. (2021). Systems-based proteomics to resolve the biology of
714 Alzheimer's disease beyond amyloid and tau. Neuropsychopharmacology *46*, 98-115.
715 10.1038/s41386-020-00840-3.
716 18. Drummond, E., Kavanagh, T., Pires, G., Marta-Ariza, M., Kanshin, E., Nayak, S., Faustin, A.,
717 Berdah, V., Ueberheide, B., and Wisniewski, T. (2022). The amyloid plaque proteome in
718 early onset Alzheimer's disease and Down syndrome. Acta Neuropathol Commun *10*, 53.
719 10.1186/s40478-022-01356-1.
720 19. De Jager, P.L., Yang, H.S., and Bennett, D.A. (2018). Deconstructing and targeting the
721 genomic architecture of human neurodegeneration. Nat Neurosci *21*, 1310-1317.
722 10.1038/s41593-018-0240-z.
723 20. Xiong, X., James, B.T., Boix, C.A., Park, Y.P., Galani, K., Victor, M.B., Sun, N., Hou, L., Ho,
724 L.L., Mantero, J., et al. (2023). Epigenomic dissection of Alzheimer's disease pinpoints
725 causal variants and reveals epigenome erosion. Cell *186*, 4422-4437 e4421.
726 10.1016/j.cell.2023.08.040.
727 21. Sun, N., Victor, M.B., Park, Y.P., Xiong, X., Scannail, A.N., Leary, N., Prosper, S.,
728 Viswanathan, S., Luna, X., Boix, C.A., et al. (2023). Human microglial state dynamics in
729 Alzheimer's disease progression. Cell *186*, 4386-4403 e4329. 10.1016/j.cell.2023.08.037.
730 22. Sun, N., Akay, L.A., Murdock, M.H., Park, Y., Galiana-Melendez, F., Bubnys, A., Galani, K.,
731 Mathys, H., Jiang, X., Ng, A.P., et al. (2023). Single-nucleus multiregion transcriptomic
732 analysis of brain vasculature in Alzheimer's disease. Nat Neurosci *26*, 970-982.
733 10.1038/s41593-023-01334-3.
734 23. Mathys, H., Peng, Z., Boix, C.A., Victor, M.B., Leary, N., Babu, S., Abdelhady, G., Jiang, X.,
735 Ng, A.P., Ghafari, K., et al. (2023). Single-cell atlas reveals correlates of high cognitive
736 function, dementia, and resilience to Alzheimer's disease pathology. Cell *186*, 4365-4385
737 e4327. 10.1016/j.cell.2023.08.039.
738 24. Wang, X., Allen, M., Li, S., Quicksall, Z.S., Patel, T.A., Carnwath, T.P., Reddy, J.S.,
739 Carrasquillo, M.M., Lincoln, S.J., Nguyen, T.T., et al. (2020). Deciphering cellular
740 transcriptional alterations in Alzheimer's disease brains. Mol Neurodegener *15*, 38.
741 10.1186/s13024-020-00392-6.
742 25. Cao, X., and Sudhof, T.C. (2001). A transcriptionally active complex of APP with Fe65 and
743 histone acetyltransferase Tip60. Science *293*, 115-120.

744 26. Balklava, Z., Niehage, C., Currinn, H., Mellor, L., Guscott, B., Poulin, G., Hoflack, B., and
745 Wassmer, T. (2015). The Amyloid Precursor Protein Controls PIKfyve Function. PLoS One
746 *10*, e0130485. 10.1371/journal.pone.0130485.
747 27. Zhang, T., Yu, J., Wang, G., and Zhang, R. (2021). Amyloid precursor protein binds with
748 TNFRSF21 to induce neural inflammation in Alzheimer's Disease. Eur J Pharm Sci *157*,
749 105598. 10.1016/j.ejps.2020.105598.
750 28. Askenazi, M., Kavanagh, T., Pires, G., Ueberheide, B., Wisniewski, T., and Drummond, E.
751 (2023). Compilation of reported protein changes in the brain in Alzheimer's disease. Nat
752 Commun *14*, 4466. 10.1038/s41467-023-40208-x.
753 29. Bai, B., Vanderwall, D., Li, Y., Wang, X., Poudel, S., Wang, H., Dey, K.K., Chen, P.C., Yang,
754 K., and Peng, J. (2021). Proteomic landscape of Alzheimer's Disease: novel insights into
755 pathogenesis and biomarker discovery. Mol Neurodegener *16*, 55. 10.1186/s13024-021-
756 00474-z.
757 30. McFarland, K.N., Ceballos, C., Rosario, A., Ladd, T., Moore, B., Golde, G., Wang, X., Allen,
758 M., Ertekin-Taner, N., Funk, C.C., et al. (2021). Microglia show differential transcriptomic
759 response to Abeta peptide aggregates ex vivo and in vivo. Life Sci Alliance *4*.
760 10.26508/lsa.202101108.
761 31. Winkler, C., and Yao, S. (2014). The midkine family of growth factors: diverse roles in
762 nervous system formation and maintenance. Br J Pharmacol *171*, 905-912.
763 10.1111/bph.12462.
764 32. Herradon, G., and Perez-Garcia, C. (2014). Targeting midkine and pleiotrophin signalling
765 pathways in addiction and neurodegenerative disorders: recent progress and
766 perspectives. Br J Pharmacol *171*, 837-848. 10.1111/bph.12312.
767 33. Ting, L., Rad, R., Gygi, S.P., and Haas, W. (2011). MS3 eliminates ratio distortion in isobaric
768 multiplexed quantitative proteomics. Nat Methods *8*, 937-940. 10.1038/nmeth.1714.
769 34. Glenner, G.G. (1980). Amyloid deposits and amyloidosis. The New England of Medicine
770 *302*, 1283-1292.
771 35. Yao, Z., van Velthoven, C.T.J., Nguyen, T.N., Goldy, J., Sedeno-Cortes, A.E., Baftizadeh, F.,
772 Bertagnolli, D., Casper, T., Chiang, M., Crichton, K., et al. (2021). A taxonomy of
773 transcriptomic cell types across the isocortex and hippocampal formation. Cell *184*, 3222-
774 3241 e3226. 10.1016/j.cell.2021.04.021.
775 36. Luckey, M., Hernandez, J., Arlaud, G., Forsyth, V.T., Ruigrok, R.W., and Mitraki, A. (2000).
776 A peptide from the adenovirus fiber shaft forms amyloid-type fibrils. FEBS Lett *468*, 23-
777 27.
778 37. Papanikolopoulou, K., Schoehn, G., Forge, V., Forsyth, V.T., Riekel, C., Hernandez, J.F.,
779 Ruigrok, R.W., and Mitraki, A. (2005). Amyloid fibril formation from sequences of a natural
780 beta-structured fibrous protein, the adenovirus fiber. J Biol Chem *280*, 2481-2490.
781 38. Levites, Y., Jansen, K., Smithson, L.A., Dakin, R., Holloway, V.M., Das, P., and Golde, T.E.
782 (2006). Intracranial adeno-associated virus-mediated delivery of anti-pan amyloid beta,
783 amyloid beta40, and amyloid beta42 single-chain variable fragments attenuates plaque
784 pathology in amyloid precursor protein mice. J Neurosci *26*, 11923-11928. 26/46/11923
785 [pii]10.1523/JNEUROSCI.2795-06.2006.
786 39. Chakrabarty, P., Li, A., Ladd, T.B., Strickland, M.R., Koller, E.J., Burgess, J.D., Funk, C.C.,
787 Cruz, P.E., Allen, M., Yaroshenko, M., et al. (2018). TLR5 decoy receptor as a novel anti-

788 amyloid therapeutic for Alzheimer's disease. J Exp Med *215*, 2247-2264.
789 10.1084/jem.20180484.
790 40. Lessard, C.B., Malnik, S.L., Zhou, Y., Ladd, T.B., Cruz, P.E., Ran, Y., Mahan, T.E., Chakrabaty,
791 P., Holtzman, D.M., Ulrich, J.D., et al. (2018). High-affinity interactions and signal
792 transduction between Abeta oligomers and TREM2. EMBO Mol Med *10*.
793 10.15252/emmm.201809027.
794 41. Eisenberg, D., and Jucker, M. (2012). The amyloid state of proteins in human diseases.
795 Cell *148*, 1188-1203. 10.1016/j.cell.2012.02.022.
796 42. Matarin, M., Salih, D.A., Yasvoina, M., Cummings, D.M., Guelfi, S., Liu, W., Nahaboo Solim,
797 M.A., Moens, T.G., Paublete, R.M., Ali, S.S., et al. (2015). A genome-wide gene-expression
798 analysis and database in transgenic mice during development of amyloid or tau
799 pathology. Cell Rep *10*, 633-644. 10.1016/j.celrep.2014.12.041.
800 43. Kunkle, B.W., Grenier-Boley, B., Sims, R., Bis, J.C., Damotte, V., Naj, A.C., Boland, A.,
801 Vronskaya, M., van der Lee, S.J., Amlie-Wolf, A., et al. (2019). Genetic meta-analysis of
802 diagnosed Alzheimer's disease identifies new risk loci and implicates Abeta, tau, immunity
803 and lipid processing. Nat Genet *51*, 414-430. 10.1038/s41588-019-0358-2.
804 44. Bellenguez, C., Kucukali, F., Jansen, I.E., Kleineidam, L., Moreno-Grau, S., Amin, N., Naj,
805 A.C., Campos-Martin, R., Grenier-Boley, B., Andrade, V., et al. (2022). New insights into
806 the genetic etiology of Alzheimer's disease and related dementias. Nat Genet *54*, 412-
807 436. 10.1038/s41588-022-01024-z.
808 45. Lambert, J.C., Ibrahim-Verbaas, C.A., Harold, D., Naj, A.C., Sims, R., Bellenguez, C.,
809 DeStafano, A.L., Bis, J.C., Beecham, G.W., Grenier-Boley, B., et al. (2013). Meta-analysis of
810 74,046 individuals identifies 11 new susceptibility loci for Alzheimer's disease. Nat Genet
811 *45*, 1452-1458. 10.1038/ng.2802.
812 46. Holstege, H., Hulsman, M., Charbonnier, C., Grenier-Boley, B., Quenez, O., Grozeva, D.,
813 van Rooij, J.G.J., Sims, R., Ahmad, S., Amin, N., et al. (2022). Exome sequencing identifies
814 rare damaging variants in ATP8B4 and ABCA1 as risk factors for Alzheimer's disease. Nat
815 Genet *54*, 1786-1794. 10.1038/s41588-022-01208-7.
816 47. Rademakers, R., Neumann, M., and Mackenzie, I.R. (2012). Advances in understanding
817 the molecular basis of frontotemporal dementia. Nat Rev Neurol *8*, 423-434.
818 10.1038/nrneurol.2012.117.
819 48. Brady, O.A., Zhou, X., and Hu, F. (2014). Regulated intramembrane proteolysis of the
820 frontotemporal lobar degeneration risk factor, TMEM106B, by signal peptide peptidase-
821 like 2a (SPPL2a). J Biol Chem *289*, 19670-19680. 10.1074/jbc.M113.515700.
822 49. Chabriat, H., Joutel, A., Dichgans, M., Tournier-Lasserve, E., and Bousser, M.G. (2009).
823 Cadasil. Lancet Neurol *8*, 643-653. 10.1016/S1474-4422(09)70127-9.
824 50. Escott-Price, V., and Hardy, J. (2022). Genome-wide association studies for Alzheimer's
825 disease: bigger is not always better. Brain Commun *4*, fcac125.
826 10.1093/braincomms/fcac125.
827 51. Andrews, S.J., Fulton-Howard, B., and Goate, A. (2020). Interpretation of risk loci from
828 genome-wide association studies of Alzheimer's disease. Lancet Neurol *19*, 326-335.
829 10.1016/S1474-4422(19)30435-1.
830 52. Modeste, E.S., Ping, L., Watson, C.M., Duong, D.M., Dammer, E.B., Johnson, E.C.B.,
831 Roberts, B.R., Lah, J.J., Levey, A.I., and Seyfried, N.T. (2023). Quantitative proteomics of

832 cerebrospinal fluid from African Americans and Caucasians reveals shared and divergent
833 changes in Alzheimer's disease. Mol Neurodegener *18*, 48. 10.1186/s13024-023-00638-z.
834 53. Watson, C.M., Dammer, E.B., Ping, L., Duong, D.M., Modeste, E., Carter, E.K., Johnson,
835 E.C.B., Levey, A.I., Lah, J.J., Roberts, B.R., and Seyfried, N.T. (2023). Quantitative Mass
836 Spectrometry Analysis of Cerebrospinal Fluid Protein Biomarkers in Alzheimer's Disease.
837 Sci Data *10*, 261. 10.1038/s41597-023-02158-3.
838 54. van Zalm, P.W., Ahmed, S., Fatou, B., Schreiber, R., Barnaby, O., Boxer, A., Zetterberg, H.,
839 Steen, J.A., and Steen, H. (2023). Meta-analysis of published cerebrospinal fluid
840 proteomics data identifies and validates metabolic enzyme panel as Alzheimer's disease
841 biomarkers. Cell Rep Med *4*, 101005. 10.1016/j.xcrm.2023.101005.
842 55. Sung, Y.J., Yang, C., Norton, J., Johnson, M., Fagan, A., Bateman, R.J., Perrin, R.J., Morris,
843 J.C., Farlow, M.R., Chhatwal, J.P., et al. (2023). Proteomics of brain, CSF, and plasma
844 identifies molecular signatures for distinguishing sporadic and genetic Alzheimer's
845 disease. Sci Transl Med *15*, eabq5923. 10.1126/scitranslmed.abq5923.
846 56. Panyard, D.J., McKetney, J., Deming, Y.K., Morrow, A.R., Ennis, G.E., Jonaitis, E.M., Van
847 Hulle, C.A., Yang, C., Sung, Y.J., Ali, M., et al. (2023). Large-scale proteome and
848 metabolome analysis of CSF implicates altered glucose and carbon metabolism and
849 succinylcarnitine in Alzheimer's disease. Alzheimers Dement. 10.1002/alz.13130.
850 57. Johnson, E.C.B., Bian, S., Haque, R.U., Carter, E.K., Watson, C.M., Gordon, B.A., Ping, L.,
851 Duong, D.M., Epstein, M.P., McDade, E., et al. (2023). Cerebrospinal fluid proteomics
852 define the natural history of autosomal dominant Alzheimer's disease. Nat Med *29*, 1979-
853 1988. 10.1038/s41591-023-02476-4.
854 58. Visser, P.J., Reus, L.M., Gobom, J., Jansen, I., Dicks, E., van der Lee, S.J., Tsolaki, M., Verhey,
855 F.R.J., Popp, J., Martinez-Lage, P., et al. (2022). Cerebrospinal fluid tau levels are
856 associated with abnormal neuronal plasticity markers in Alzheimer's disease. Mol
857 Neurodegener *17*, 27. 10.1186/s13024-022-00521-3.
858 59. Delvenne, A., Gobom, J., Tijms, B., Bos, I., Reus, L.M., Dobricic, V., Kate, M.T., Verhey, F.,
859 Ramakers, I., Scheltens, P., et al. (2022). Cerebrospinal fluid proteomic profiling of
860 individuals with mild cognitive impairment and suspected non-Alzheimer's disease
861 pathophysiology. Alzheimers Dement. 10.1002/alz.12713.
862 60. Del Campo, M., Peeters, C.F.W., Johnson, E.C.B., Vermunt, L., Hok, A.H.Y.S., van Nee, M.,
863 Chen-Plotkin, A., Irwin, D.J., Hu, W.T., Lah, J.J., et al. (2022). CSF proteome profiling across
864 the Alzheimer's disease spectrum reflects the multifactorial nature of the disease and
865 identifies specific biomarker panels. Nat Aging *2*, 1040-1053. 10.1038/s43587-022-00300-
866 1.
867 61. Dammer, E.B., Ping, L., Duong, D.M., Modeste, E.S., Seyfried, N.T., Lah, J.J., Levey, A.I., and
868 Johnson, E.C.B. (2022). Multi-platform proteomic analysis of Alzheimer's disease
869 cerebrospinal fluid and plasma reveals network biomarkers associated with proteostasis
870 and the matrisome. Alzheimers Res Ther *14*, 174. 10.1186/s13195-022-01113-5.
871 62. Higginbotham, L., Ping, L., Dammer, E.B., Duong, D.M., Zhou, M., Gearing, M., Hurst, C.,
872 Glass, J.D., Factor, S.A., Johnson, E.C.B., et al. (2020). Integrated proteomics reveals brain-
873 based cerebrospinal fluid biomarkers in asymptomatic and symptomatic Alzheimer's
874 disease. Sci Adv *6*. 10.1126/sciadv.aaz9360.

63. Dawson, T.M., Golde, T.E., and Lagier-Tourenne, C. (2018). Animal models of neurodegenerative diseases. Nat Neurosci *21*, 1370-1379. 10.1038/s41593-018-0236-8.
64. Drummond, E., and Wisniewski, T. (2017). Alzheimer's disease: experimental models and reality. Acta Neuropathol *133*, 155-175. 10.1007/s00401-016-1662-x.
65. Chishti, M.A., Yang, D.S., Janus, C., Phinney, A.L., Horne, P., Pearson, J., Strome, R., Zuker, N., Loukides, J., French, J., et al. (2001). Early-onset amyloid deposition and cognitive deficits in transgenic mice expressing a double mutant form of amyloid precursor protein 695. J Biol Chem *276*, 21562-21570.
66. Wykes, R., Kalmbach, A., Eliava, M., and Waters, J. (2012). Changes in the physiology of CA1 hippocampal pyramidal neurons in preplaque CRND8 mice. Neurobiol Aging *33*, 1609-1623. 10.1016/j.neurobiolaging.2011.05.001.
67. Jolas, T., Zhang, X.S., Zhang, Q., Wong, G., Del Vecchio, R., Gold, L., and Priestley, T. (2002). Long-term potentiation is increased in the CA1 area of the hippocampus of APP(swe/ind) CRND8 mice. Neurobiol Dis *11*, 394-409.
68. Chakrabarty, P., Li, A., Ceballos-Diaz, C., Eddy, J.A., Funk, C.C., Moore, B., DiNunno, N., Rosario, A.M., Cruz, P.E., Verbeeck, C., et al. (2015). IL-10 alters immunoproteostasis in APP mice, increasing plaque burden and worsening cognitive behavior. Neuron *85*, 519-533. 10.1016/j.neuron.2014.11.020.
69. Palop, J.J., and Mucke, L. (2010). Amyloid-beta-induced neuronal dysfunction in Alzheimer's disease: from synapses toward neural networks. Nat Neurosci *13*, 812-818. 10.1038/nn.2583.
70. Selkoe, D.J., and Hardy, J. (2016). The amyloid hypothesis of Alzheimer's disease at 25 years. EMBO Mol Med *8*, 595-608. 10.15252/emmm.201606210.
71. Yu, L., Tasaki, S., Schneider, J.A., Arfanakis, K., Duong, D.M., Wingo, A.P., Wingo, T.S., Kearns, N., Thatcher, G.R.J., Seyfried, N.T., et al. (2020). Cortical Proteins Associated With Cognitive Resilience in Community-Dwelling Older Persons. JAMA Psychiatry *77*, 1172-1180. 10.1001/jamapsychiatry.2020.1807.
72. Hurst, C.D., Dunn, A.R., Dammer, E.B., Duong, D.M., Seyfried, N.T., Kaczorowski, C.C., and Johnson, E.C.B. (2023). Genetic background influences the 5XFAD Alzheimer's disease mouse model brain proteome. bioRxiv. 10.1101/2023.06.12.544646.
73. Mitew, S., Kirkcaldie, M.T., Halliday, G.M., Shepherd, C.E., Vickers, J.C., and Dickson, T.C. (2010). Focal demyelination in Alzheimer's disease and transgenic mouse models. Acta Neuropathol *119*, 567-577. 10.1007/s00401-010-0657-2.
74. Desai, M.K., Mastrangelo, M.A., Ryan, D.A., Sudol, K.L., Narrow, W.C., and Bowers, W.J. (2010). Early oligodendrocyte/myelin pathology in Alzheimer's disease mice constitutes a novel therapeutic target. Am J Pathol *177*, 1422-1435. 10.2353/ajpath.2010.100087.
75. Desai, M.K., Sudol, K.L., Janelsins, M.C., Mastrangelo, M.A., Frazer, M.E., and Bowers, W.J. (2009). Triple-transgenic Alzheimer's disease mice exhibit region-specific abnormalities in brain myelination patterns prior to appearance of amyloid and tau pathology. Glia *57*, 54-65. 10.1002/glia.20734.
76. Allen, M., Wang, X., Burgess, J.D., Watzlawik, J., Serie, D.J., Younkin, C.S., Nguyen, T., Malphrus, K.G., Lincoln, S., Carrasquillo, M.M., et al. (2018). Conserved brain myelination networks are altered in Alzheimer's and other neurodegenerative diseases. Alzheimers Dement *14*, 352-366. 10.1016/j.jalz.2017.09.012.

919 77. McKenzie, A.T., Moyon, S., Wang, M., Katsyv, I., Song, W.M., Zhou, X., Dammer, E.B.,
920 Duong, D.M., Aaker, J., Zhao, Y., et al. (2017). Multiscale network modeling of
921 oligodendrocytes reveals molecular components of myelin dysregulation in Alzheimer's
922 disease. Mol Neurodegener *12*, 82. 10.1186/s13024-017-0219-3.
923 78. Nasrabady, S.E., Rizvi, B., Goldman, J.E., and Brickman, A.M. (2018). White matter changes
924 in Alzheimer's disease: a focus on myelin and oligodendrocytes. Acta Neuropathol
925 Commun *6*, 22. 10.1186/s40478-018-0515-3.
926 79. Min, Y., Wang, X., Is, O., Patel, T.A., Gao, J., Reddy, J.S., Quicksall, Z.S., Nguyen, T., Lin, S.,
927 Tutor-New, F.Q., et al. (2023). Cross species systems biology discovers glial DDR2, STOM,
928 and KANK2 as therapeutic targets in progressive supranuclear palsy. Nat Commun *14*,
929 6801. 10.1038/s41467-023-42626-3.
930 80. Wang, X., Allen, M., Is, O., Reddy, J.S., Tutor-New, F.Q., Castanedes Casey, M.,
931 Carrasquillo, M.M., Oatman, S.R., Min, Y., Asmann, Y.W., et al. (2022). Alzheimer's disease
932 and progressive supranuclear palsy share similar transcriptomic changes in distinct brain
933 regions. J Clin Invest *132*. 10.1172/JCI149904.
934 81. Golde, T.E. (2019). Harnessing Immunoproteostasis to Treat Neurodegenerative
935 Disorders. Neuron *101*, 1003-1015. 10.1016/j.neuron.2019.02.027.
936 82. Patel, T., Carnwath, T.P., Wang, X., Allen, M., Lincoln, S.J., Lewis-Tuffin, L.J., Quicksall, Z.S.,
937 Lin, S., Tutor-New, F.Q., Ho, C.C.G., et al. (2022). Transcriptional landscape of human
938 microglia implicates age, sex, and APOE-related immunometabolic pathway
939 perturbations. Aging Cell *21*, e13606. 10.1111/acel.13606.
940 83. Van Acker, Z.P., Perdok, A., Bretou, M., and Annaert, W. (2021). The microglial lysosomal
941 system in Alzheimer's disease: Guardian against proteinopathy. Ageing Res Rev *71*,
942 101444. 10.1016/j.arr.2021.101444.
943 84. Pimplikar, S.W., Nixon, R.A., Robakis, N.K., Shen, J., and Tsai, L.H. (2010). Amyloid-
944 independent mechanisms in Alzheimer's disease pathogenesis. J Neurosci *30*, 14946-
945 14954. 10.1523/JNEUROSCI.4305-10.2010.
946 85. Ibanez, K.R., McFarland, K.N., Phillips, J., Allen, M., Lessard, C.B., Zobel, L., De La Cruz, E.G.,
947 Shah, S., Vo, Q., Wang, X., et al. (2022). Deletion of Abi3/Gngt2 influences age-progressive
948 amyloid beta and tau pathologies in distinctive ways. Alzheimers Res Ther *14*, 104.
949 10.1186/s13195-022-01044-1.
950 86. Castellano, J.M., Kim, J., Stewart, F.R., Jiang, H., DeMattos, R.B., Patterson, B.W., Fagan,
951 A.M., Morris, J.C., Mawuenyega, K.G., Cruchaga, C., et al. (2011). Human apoE isoforms
952 differentially regulate brain amyloid-beta peptide clearance. Sci Transl Med *3*, 89ra57.
953 10.1126/scitranslmed.3002156.
954 87. Holtzman, D.M. (2004). In vivo effects of ApoE and clusterin on amyloid-beta metabolism
955 and neuropathology. J Mol Neurosci *23*, 247-254.
956 88. Fagan, A.M., Watson, M., Parsadanian, M., Bales, K.R., Paul, S.M., and Holtzman, D.M.
957 (2002). Human and murine ApoE markedly alters A beta metabolism before and after
958 plaque formation in a mouse model of Alzheimer's disease. Neurobiol Dis *9*, 305-318.
959 89. Soderberg, L., Zhukareva, V., Bogdanovic, N., Hashimoto, T., Winblad, B., Iwatsubo, T.,
960 Lee, V.M., Trojanowski, J.Q., and Naslund, J. (2003). Molecular identification of AMY, an
961 Alzheimer disease amyloid-associated protein. J Neuropathol Exp Neurol *62*, 1108-1117.
962 10.1093/jnen/62.11.1108.

963 90. Hashimoto, T., Wakabayashi, T., Watanabe, A., Kowa, H., Hosoda, R., Nakamura, A.,
964 Kanazawa, I., Arai, T., Takio, K., Mann, D.M., and Iwatsubo, T. (2002). CLAC: a novel
965 Alzheimer amyloid plaque component derived from a transmembrane precursor, CLAC-
966 P/collagen type XXV. EMBO J *21*, 1524-1534. 10.1093/emboj/21.7.1524.
967 91. Langfelder, P., and Horvath, S. (2008). WGCNA: an R package for weighted correlation
968 network analysis. BMC Bioinformatics *9*, 559. 10.1186/1471-2105-9-559.
969 92. Zellner, A., Muller, S.A., Lindner, B., Beaufort, N., Rozemuller, A.J.M., Arzberger, T.,
970 Gassen, N.C., Lichtenthaler, S.F., Kuster, B., Haffner, C., and Dichgans, M. (2022).
971 Proteomic profiling in cerebral amyloid angiopathy reveals an overlap with CADASIL
972 highlighting accumulation of HTRA1 and its substrates. Acta Neuropathol Commun *10*, 6.
973 10.1186/s40478-021-01303-6.
974 93. Hondius, D.C., Eigenhuis, K.N., Morrema, T.H.J., van der Schors, R.C., van Nierop, P.,
975 Bugiani, M., Li, K.W., Hoozemans, J.J.M., Smit, A.B., and Rozemuller, A.J.M. (2018).
976 Proteomics analysis identifies new markers associated with capillary cerebral amyloid
977 angiopathy in Alzheimer's disease. Acta Neuropathol Commun *6*, 46. 10.1186/s40478-
978 018-0540-2.
979 94. Zellner, A., Scharrer, E., Arzberger, T., Oka, C., Domenga-Denier, V., Joutel, A.,
980 Lichtenthaler, S.F., Muller, S.A., Dichgans, M., and Haffner, C. (2018). CADASIL brain
981 vessels show a HTRA1 loss-of-function profile. Acta Neuropathol *136*, 111-125.
982 10.1007/s00401-018-1853-8.
983 95. Cerezo-Wallis, D., Contreras-Alcalde, M., Troule, K., Catena, X., Mucientes, C., Calvo, T.G.,
984 Canon, E., Tejedo, C., Pennacchi, P.C., Hogan, S., et al. (2020). Midkine rewires the
985 melanoma microenvironment toward a tolerogenic and immune-resistant state. Nat Med
986 *26*, 1865-1877. 10.1038/s41591-020-1073-3.
987 96. Tang, Y., Kwiatkowski, D.J., and Henske, E.P. (2022). Midkine expression by stem-like
988 tumor cells drives persistence to mTOR inhibition and an immune-suppressive
989 microenvironment. Nat Commun *13*, 5018. 10.1038/s41467-022-32673-7.
990 97. Shen, D., Podolnikova, N.P., Yakubenko, V.P., Ardell, C.L., Balabiyev, A., Ugarova, T.P., and
991 Wang, X. (2017). Pleiotrophin, a multifunctional cytokine and growth factor, induces
992 leukocyte responses through the integrin Mac-1. J Biol Chem *292*, 18848-18861.
993 10.1074/jbc.M116.773713.
994 98. Muramatsu, H., Yokoi, K., Chen, L., Ichihara-Tanaka, K., Kimura, T., and Muramatsu, T.
995 (2011). Midkine as a factor to counteract the deposition of amyloid beta-peptide plaques:
996 in vitro analysis and examination in knockout mice. Int Arch Med *4*, 1. 10.1186/1755-
997 7682-4-1.
998 99. Snow, A.D., Cummings, J.A., and Lake, T. (2021). The Unifying Hypothesis of Alzheimer's
999 Disease: Heparan Sulfate Proteoglycans/Glycosaminoglycans Are Key as First
1000 Hypothesized Over 30 Years Ago. Front Aging Neurosci *13*, 710683.
1001 10.3389/fnagi.2021.710683.
1002 100. Vaquer-Alicea, J., and Diamond, M.I. (2019). Propagation of Protein Aggregation in
1003 Neurodegenerative Diseases. Annu Rev Biochem *88*, 785-810. 10.1146/annurev-
1004 biochem-061516-045049.
1005 101. Kourelis, T.V., Dasari, S.S., Dispenzieri, A., Maleszewski, J.J., Redfield, M.M., Fayyaz, A.U.,
1006 Grogan, M., Ramirez-Alvarado, M., Abou Ezzeddine, O.F., and McPhail, E.D. (2020). A

1007 Proteomic Atlas of Cardiac Amyloid Plaques. JACC CardioOncol *2*, 632-643.
1008 10.1016/j.jaccao.2020.08.013.
1009 102. Rahman, M.M., and Lendel, C. (2021). Extracellular protein components of amyloid
1010 plaques and their roles in Alzheimer's disease pathology. Mol Neurodegener *16*, 59.
1011 10.1186/s13024-021-00465-0.
1012 103. Wagner, J., Degenhardt, K., Veit, M., Louros, N., Konstantoulea, K., Skodras, A., Wild, K.,
1013 Liu, P., Obermuller, U., Bansal, V., et al. (2022). Medin co-aggregates with vascular
1014 amyloid-beta in Alzheimer's disease. Nature *612*, 123-131. 10.1038/s41586-022-05440-3.
1015 104. Venegas, C., Kumar, S., Franklin, B.S., Dierkes, T., Brinkschulte, R., Tejera, D., Vieira-
1016 Saecker, A., Schwartz, S., Santarelli, F., Kummer, M.P., et al. (2017). Microglia-derived ASC
1017 specks cross-seed amyloid-beta in Alzheimer's disease. Nature *552*, 355-361.
1018 10.1038/nature25158.
1019 105. Yakupova, E.I., Bobyleva, L.G., Shumeyko, S.A., Vikhlyantsev, I.M., and Bobylev, A.G.
1020 (2021). Amyloids: The History of Toxicity and Functionality. Biology (Basel) *10*.
1021 10.3390/biology10050394.
1022 106. Walsh, D.M., and Selkoe, D.J. (2004). Deciphering the molecular basis of memory failure
1023 in Alzheimer's disease. Neuron *44*, 181-193.
1024 107. Dobson, C.M., Knowles, T.P.J., and Vendruscolo, M. (2020). The Amyloid Phenomenon
1025 and Its Significance in Biology and Medicine. Cold Spring Harb Perspect Biol *12*.
1026 10.1101/cshperspect.a033878.
1027 108. Papadimitriou, E., Mourkogianni, E., Ntenekou, D., Christopoulou, M., Koutsioumpa, M.,
1028 and Lamprou, M. (2022). On the role of pleiotrophin and its receptors in development
1029 and angiogenesis. Int J Dev Biol *66*, 115-124. 10.1387/ijdb.210122ep.
1030 109. Weckbach, L.T., Grabmaier, U., Uhl, A., Gess, S., Boehm, F., Zehrer, A., Pick, R.,
1031 Salvermoser, M., Czermak, T., Pircher, J., et al. (2019). Midkine drives cardiac
1032 inflammation by promoting neutrophil trafficking and NETosis in myocarditis. J Exp Med
1033 *216*, 350-368. 10.1084/jem.20181102.
1034 110. Woulfe, K.C., and Sucharov, C.C. (2017). Midkine's Role in Cardiac Pathology. J Cardiovasc
1035 Dev Dis *4*. 10.3390/jcdd4030013.
1036 111. Rubel, M.S., Fedotov, S.A., Grizel, A.V., Sopova, J.V., Malikova, O.A., Chernoff, Y.O., and
1037 Rubel, A.A. (2020). Functional Mammalian Amyloids and Amyloid-Like Proteins. Life
1038 (Basel) *10*. 10.3390/life10090156.
1039 112. Venegas, C., and Heneka, M.T. (2017). Danger-associated molecular patterns in
1040 Alzheimer's disease. J Leukoc Biol *101*, 87-98. 10.1189/jlb.3MR0416-204R.
1041 113. Pinals, R.L., and Tsai, L.H. (2022). Building in vitro models of the brain to understand the
1042 role of APOE in Alzheimer's disease. Life Sci Alliance *5*. 10.26508/lsa.202201542.
1043 114. Martens, Y.A., Zhao, N., Liu, C.C., Kanekiyo, T., Yang, A.J., Goate, A.M., Holtzman, D.M.,
1044 and Bu, G. (2022). ApoE Cascade Hypothesis in the pathogenesis of Alzheimer's disease
1045 and related dementias. Neuron *110*, 1304-1317. 10.1016/j.neuron.2022.03.004.
1046 115. Xiong, M., Jiang, H., Serrano, J.R., Gonzales, E.R., Wang, C., Gratuze, M., Hoyle, R., Bien-
1047 Ly, N., Silverman, A.P., Sullivan, P.M., et al. (2021). APOE immunotherapy reduces cerebral
1048 amyloid angiopathy and amyloid plaques while improving cerebrovascular function. Sci
1049 Transl Med *13*. 10.1126/scitranslmed.abd7522.

116. Wang, H., Dey, K.K., Chen, P.C., Li, Y., Niu, M., Cho, J.H., Wang, X., Bai, B., Jiao, Y., Chepyala, S.R., et al. (2020). Integrated analysis of ultra-deep proteomes in cortex, cerebrospinal fluid and serum reveals a mitochondrial signature in Alzheimer's disease. Mol Neurodegener *15*, 43. 10.1186/s13024-020-00384-6.
117. Moore, B.D., Ran, Y., Goodwin, M.S., Komatineni, K., McFarland, K.N., Dillon, K., Charles, C., Ryu, D., Liu, X., Prokop, S., et al. (2023). A C1qTNF3 collagen domain fusion chaperones diverse secreted proteins and anti-Aβ scFvs: applications for gene therapies. Molecular Therapy Methods & Clinical Development. DOI:https://doi.org/10.1016/j.omtm.2023.101146.
118. Chakrabarty, P., Jansen-West, K., Beccard, A., Ceballos-Diaz, C., Levites, Y., Verbeeck, C., Zubair, A.C., Dickson, D., Golde, T.E., and Das, P. (2010). Massive gliosis induced by interleukin-6 suppresses Abeta deposition in vivo: evidence against inflammation as a driving force for amyloid deposition. FASEB J *24*, 548-559. fj.09-141754 [pii]10.1096/fj.09-141754.
119. Xu, G., Ran, Y., Fromholt, S.E., Fu, C., Yachnis, A.T., Golde, T.E., and Borchelt, D.R. (2015). Murine Abeta over-production produces diffuse and compact Alzheimer-type amyloid deposits. Acta Neuropathol Commun *3*, 72. 10.1186/s40478-015-0252-9.
120. Levites, Y., Das, P., Price, R.W., Rochette, M.J., Kostura, L.A., McGowan, E.M., Murphy, M.P., and Golde, T.E. (2006). Anti-Abeta42- and anti-Abeta40-specific mAbs attenuate amyloid deposition in an Alzheimer disease mouse model. J Clin Invest *116*, 193-201. 10.1172/JCI25410.
121. Moore, B.D., Levites, Y., Xu, G., Hampton, H., Adamo, M.F., Croft, C.L., Futch, H.S., Moran, C., Fromholt, S., Janus, C., et al. (2022). Soluble brain homogenates from diverse human and mouse sources preferentially seed diffuse Abeta plaque pathology when injected into newborn mouse hosts. Free Neuropathol *3*. 10.17879/freeneuropathology-2022-3766.
122. Naiki, H., Higuchi, K., Nakakuki, K., and Takeda, T. (1991). Kinetic analysis of amyloid fibril polymerization in vitro. Lab Invest *65*, 104-110.
123. Young, M.D., Wakefield, M.J., Smyth, G.K., and Oshlack, A. (2010). Gene ontology analysis for RNA-seq: accounting for selection bias. Genome Biol *11*, R14. 10.1186/gb-2010-11-2-r14.
124. Dobin, A., Davis, C.A., Schlesinger, F., Drenkow, J., Zaleski, C., Jha, S., Batut, P., Chaisson, M., and Gingeras, T.R. (2013). STAR: ultrafast universal RNA-seq aligner. Bioinformatics *29*, 15-21. 10.1093/bioinformatics/bts635.
125. Lawrence, M., Huber, W., Pages, H., Aboyoun, P., Carlson, M., Gentleman, R., Morgan, M.T., and Carey, V.J. (2013). Software for computing and annotating genomic ranges. PLoS Comput Biol *9*, e1003118. 10.1371/journal.pcbi.1003118.
126. Love, M.I., Huber, W., and Anders, S. (2014). Moderated estimation of fold change and dispersion for RNA-seq data with DESeq2. Genome Biol *15*, 550. 10.1186/s13059-014-0550-8.
127. Nikolayeva, O., and Robinson, M.D. (2014). edgeR for differential RNA-seq and ChIP-seq analysis: an application to stem cell biology. Methods Mol Biol *1150*, 45-79. 10.1007/978-1-4939-0512-6_3.

1094 **METHODS**

1095 Cloning and cell culture. All cDNAs used were synthesized by Genscript (Piscataway, NJ) and subcloned
1096 into pCDNA3.1 vector, the rAAV2-CBA expression vector pCTR4 [117], or both. All cDNAs incorporated a FLAG
1097 epitope tag (DYKDDDDK) on the -COOH terminal. To overexpress the genes, 2.7 µg plasmid were
1098 transiently transfected into HEK 293T cells in a 6-well dish using polyethylenimine (PEI). Media was
1099 replaced with FBS free Opti-MEM after 18 hr incubation. Cells and conditioned media were collected after
1100 another 24 hr incubation. Bis-Tris precast gels (Bio-Rad, Hercules, CA) were used for all SDS-PAGE. 50 µg
1101 cell lysate by total protein and 30 µl media of each sample were loaded. Western blot was developed
1102 using monoclonal anti-FLAG M2 antibody and anti-β-actin (Sigma-Aldrich, Inc, St. Louis, MO).

1103 Animal models and neonatal injections. All animal procedures were approved by the Institutional Animal
1104 Care and Use Committee in accordance with NIH guidelines. CRND8 mice were bred in house and housed
1105 three to five to a cage and maintained on ad libitum food and water with a 12hr light/dark cyclev.
1106 Intracerebroventricular injections of recombinant adeno-associated virus (rAAVs) were carried out on day
1107 P0 as described previously[118]. Two microliters of rAAV2/1 encoding Mdk and PTN was administrated
1108 bilaterally into the cerebral ventricle. Mice injected with rAAV encoding MDK and PTN were aged 3 or 6
1109 months and euthanized, brains were harvested and one hemibrain was fixed overnight in 4%
1110 paraformaldehyde at 4°C followed by processing and paraffin embedding for immunohistochemical
1111 staining. The other hemibrain was snap frozen in isopentane on dry-ice and then stored at -80°C until it
1112 was thawed and homogenized for ELISA measurements of Aβ peptide levels.

1113 Mouse Brain Histology and immunohistochemistry. Paraffin sections (5 µm) were used for all histology
1114 and immunohistochemistry studies. For various antibodies screens two hemibrains from the same mouse
1115 were fixed in EtOH or in 4% PFA (alternatively, in 10% Formalin) and embedded into the same block.
1116 Antibodies used are listed in Table S11. The slides were scanned by Aperio XT System (Leica Biosystems,
1117 Buffalo Grove, IL). Thio-S tissue staining methods were performed as previously described [119]. For studies
1118 in mice injected with pAAV-mMdk or pAAV-hPTN, embedded sections were immunohistochemically
1119 stained with a biotinylated pan-Aβ antibody Ab5 [120] (1:500) or anti-FLAG antibody (Sigma-Aldrich Inc, St.
1120 Louis, IL) and developed using Vectastain Elite ABC Kit (Vector Laboratories, Burlingame, CA) followed with
1121 3,3'-diaminobenzidine (DAB) substrate (Vector Laboratories, Burlingame, CA) and counterstained with
1122 hematoxylin. The slides were scanned by Aperio XT System and analyzed using the ImageScope program.
1123 In brief, at least three sections per sample, at least 30 µm apart, were imaged and plaque burden was
1124 quantified. For three-month old mice, plaque number was calculated by two independent observers.

1125 Human Tissue Histology and immunohistochemistry. 5 µm thick sections of formalin fixed or ethanol fixed,
1126 paraffin embedded postmortem brain tissue was deparaffinized in xylene twice for 5 minutes and
1127 followed by rehydration in descending ethanol series (100%, 100%, 90%, 70%) for 1 minute each. For
1128 Formic acid antigen retrieval, sections were immersed in a 70% Formic acid solution for 20 minutes (where
1129 indicated in Table S12). Sections were incubated in 0.1M Tris and 0.005% Tween (or Citrate buffer, where
1130 indicated in table below) at high pressure in a pressure cooker for 15 minutes, followed by incubation in
1131 a PBS/H_2O_2 solution with 10% Triton-x for 20 minutes to quench endogenous peroxidase. The sections
1132 were washed with tap water and then equilibrated to 0.1M Tris for 5 min before blocking in normal horse
1133 serum for 20 minutes, followed by blocking in 2% FBS/0.1 M Tris, (pH 7.6) for 5 minutes. After that, primary
1134 antibody, diluted in 2% FBS/0.1 M Tris, (pH 7.6) was applied to the section and incubated overnight at 4
1135 °C. Dilutions for each antisera are listed in Table S11. The next day, sections were quickly rinsed in 0.1M
1136 Tris and blocked in 2% FBS/0.1 M Tris, (pH 7.6) for 5 minutes before incubating with the secondary
1137 antibody (HRP-conjugated ImmPRESS Polymer Reagent, Vector Labs) for 30 minutes at room temperature.
1138 Following a quick wash in 0.1M Tris, the signal was developed using 3,3'-diaminobenzidin (DAB, Vector
1139 Lab SK-410) for 1-2 minutes and then sections were counterstained with hematoxylin (Mayer's version,
1140 Sigma Aldrich) for 1 minute. Next, sections were washed in tap water, and then dehydrated in an

1141 ascending series of ethanol (70%, 90%, 100%, 100%) for 1 minute each, followed by xylene (2 x 5 mins).
1142 Sections were coverslipped using Cytoseal 60 (Thermo Fisher) mounting media and dried overnight.
1143 Aβ ELISAs. After tissue harvesting, the left hemisphere was flash-frozen in isopentane. The frozen cortex
1144 was sequentially extracted with protease inhibitor cocktail (Roche, Basel, Switzerland) containing RIPA
1145 buffer, 2% SDS, and 70% formic acid (FA) as described previously at a concentration of 150 mg/ml. Aβ
1146 levels from the 2% SDS– and 70% FA–extracted samples were quantified using end-specific sandwich ELISA
1147 as previously described [121]. Aβ40 was captured with mAb 13.1.1 and detected by HRP-conjugated mAb5.
1148 Aβ42 was captured with mAb 2.1.3 and detected by HRP-conjugated mAb5. ELISA results were analyzed
1149 using SoftMax Pro software (Molecular Devices, San Jose, CA).
1150 Amyloid-β Aggregation Assay. The effect of midkine (MDK) and pleiotrophin (PTN) proteins on amyloid
1151 beta 1-42 ($A\beta_{1-42}$) aggregation was measured by *in vitro* thioflavin T (ThT) fluorescence assay, as previously
1152 described [122]. Recombinant human $A\beta_{1-42}$ (20 ng/µL equivalent to 5 µM) from rPeptide (A-1170-1) was
1153 incubated in Tris-buffered Saline (TBS; 150 mM NaCl, 50 mM Tris-HCl, pH 7.6), and 20 µM ThT in the
1154 presence or absence of purified recombinant MDK (1.25 ng/µl equivalent to 47 nM) from Sino Biological
1155 (10247-HNAB) or PTN (5 ng/µl equivalent to 327 nM) from R&D Systems (R&D252-PL-050). The final
1156 volume within each well was 100 µL. The assay was conducted in quadruplicates using chilled (4ºC) 96
1157 well black clear bottom plates (Corning, #3904). Fluorescence was captured at 420 Ex, 480 Em for 20 hours
1158 at 15 min intervals at 37ºC using Synergy H1 (Biotek) microplate reader. ThT alone (20 µM) was measured
1159 and subtracted as background fluorescence. A titration curve was also performed with fixed concentration
1160 of $A\beta_{1-42}$ (5 µM) and an increasing concentration of MDK (12 nM, 23 nM, 47 nM and 93 nM) or PTN (82
1161 nM 163 nM and 327 nM). Fluorescence intensities were graphed using GraphPad Prism.
1162 Pulldowns and Western Blot Analysis $A\beta_{1-42}$ fibrils prepared as described above (20 hr incubation) were
1163 precipitated by centrifugation at 10,000 x g. The pellet was resuspended in 8M urea buffer (8 M urea, 100
1164 mm $NaHPO_4$, pH 8.5) and boiled in Laemmli sample buffer (BioRad, 161-0737) at 98°C for 5 min. Proteins
1165 were resolved on Bolt 4-12% Bis-Tris gels (Thermo Fisher Scientific, NW04120BOX) followed by transfer
1166 to nitrocellulose membrane using iBlot 2 dry blotting system (ThermoFisher Scientific, IB21001).
1167 Membranes were incubated with StartingBlock buffer (ThermoFisher, 37543) for 30 min followed by
1168 overnight incubation at 4º in primary antibodies including Aβ (Novus, NBP11-97929), MDK (Abcam,
1169 #52637), and PTN (Abcam, #ab79411) antibodies. Membranes were washed with TBS containing 0.1%
1170 (v/v) Tween 20 (TBS-T) and incubated with fluorophore-conjugated secondary antibodies (Alexa Fluor-680
1171 or Alexa Fluor-800; Invitrogen) for 1 hr at room temperature. Membranes were subsequently washed
1172 three times with TBS-T and images were captured using an Odyssey Infrared Imaging System (LI-COR
1173 Biosciences).
1174 Statistical analysis
1175 Data were analyzed statistically according to the methods specified in each figure legend. Briefly, p values
1176 were obtained as specified by either a one-way ANOVA test with two groups, or for enrichment, by a
1177 Fisher's Exact test. P values were corrected for multiple testing were indicated by Benjamini-Hochberg
1178 FDR correction. For significance of Pearson correlations, Student's test was used.
1179 Proteomic Sample Processing
1180 Each tissue piece was individually homogenized in 300 uL of urea lysis buffer (8M urea, 100 mM $NaHPO_4$,
1181 pH 8.5), including 3 uL (100x stock) HALT protease and phosphatase inhibitor cocktail (Pierce). All
1182 homogenization was performed using a Bullet Blender (Next Advance) according to manufacturer
1183 protocols. Briefly, each tissue piece was added to Urea lysis buffer in a 1.5 mL Rino tube (Next Advance)
1184 harboring 500 mg stainless steel beads (0.9-2 mm in diameter) and blended twice for 5-minute intervals
1185 in the cold room (4°C). Protein supernatants were transferred to 1.5 mL Eppendorf tubes and sonicated
1186 (Sonic Dismembrator, Fisher Scientific) 3 times for 5 s with 15 s intervals of rest at 30% amplitude to
1187 disrupt nucleic acids and subsequently vortexed. Protein concentration was determined by the
1188 bicinchoninic acid (BCA) method, and samples were frozen in aliquots at −80°C. Protein homogenates

1189 (100 ug) were diluted with 50 mM NH_4HCO_3 to a final concentration of less than 2M urea and then treated
1190 with 1 mM dithiothreitol (DTT) at 25°C for 30 minutes, followed by 5 mM iodoacetimide (IAA) at 25°C for
1191 30 minutes in the dark. Protein was digested with 1:100 (w/w) lysyl endopeptidase (Wako) at 25°C for 2
1192 hours and further digested overnight with 1:50 (w/w) trypsin (Promega) at 25°C. Resulting peptides were
1193 desalted with a Sep-Pak C18 column (Waters) and dried under vacuum.
1194 Tandem Mass Tag (TMT) Labeling
1195 Batches 1 and 2 were labeled using the TMT 11-plex kit (ThermoFisher 90406 – Lot# TG273545 and
1196 TG273555) while batch 3 was labeled with TMTPro (ThermoFisher A44520 – Lot# VH311511) according to
1197 manufacturer's protocol. For batches 1 and 2, each sample (containing 100 µg of peptides) was re-
1198 suspended in 100 mM TEAB buffer (100 µL). The TMT labeling reagents were equilibrated to room
1199 temperature, and anhydrous ACN (256 µL) was added to each reagent channel. Each channel was gently
1200 vortexed for 5 min, and then 41 µL from each TMT channel was transferred to the peptide solutions and
1201 allowed to incubate for 1 h at room temperature. The reaction was quenched with 5% (vol/vol)
1202 hydroxylamine (8 µL) (Pierce). For batch 3, each sample (containing 100 µg of peptides) was re-suspended
1203 in 100 mM TEAB buffer (100 µL). The TMT labeling reagents were equilibrated to room temperature, and
1204 anhydrous ACN (200 µL) was added to each reagent channel. Each channel was gently vortexed for 5 min,
1205 and then 20 µL from each TMT channel was transferred to the peptide solutions and allowed to incubate
1206 for 1 h at room temperature. All channels for each batch were then combined (batch 1 used all 11
1207 channels, batch 2 utilized only 10 channel and batch 3 utilized only 8 channels) and dried by SpeedVac
1208 (LabConco) to approximately 150 µL and diluted with 1 mL of 0.1% (vol/vol) TFA, then acidified to a final
1209 concentration of 1% (vol/vol) FA and 0.1% (vol/vol) TFA. Peptides were desalted with a 200 mg C18 Sep-
1210 Pak column (Waters). Each Sep-Pak column was activated with 3 mL of methanol, washed with 3 mL of
1211 50% (vol/vol) ACN, and equilibrated with 2×3 mL of 0.1% TFA. The samples were then loaded, and each
1212 column was washed with 2×3 mL 0.1% (vol/vol) TFA, followed by 2 mL of 1% (vol/vol) FA. Elution was
1213 performed with 2 volumes of 1.5 mL 50% (vol/vol) ACN. The eluates were then dried to completeness.
1214 High pH Fractionation
1215 For batches 1 and 2, dried samples were re-suspended in high pH loading buffer (0.07% vol/vol NH_4OH,
1216 0.045% vol/vol FA, 2% vol/vol ACN) and loaded onto an Agilent ZORBAX 300 Extend-C18 column (2.1mm
1217 x 150 mm with 3.5 µm beads). An Agilent 1100 HPLC system was used to carry out the fractionation.
1218 Solvent A consisted of 0.0175% (vol/vol) NH4OH, 0.01125% (vol/vol) FA, and 2% (vol/vol) ACN; solvent B
1219 consisted of 0.0175% (vol/vol) NH4OH, 0.01125% (vol/vol) FA, and 90% (vol/vol) ACN. The sample elution
1220 was performed over a 58.6 min gradient with a flow rate of 0.4 mL/min. The gradient consisted of 100%
1221 solvent A for 2 min, then 0% to 12% solvent B over 6 min, then 12% to 40 % over 28 min, then 40% to 44%
1222 over 4 min, then 44% to 60% over 5 min, and then held constant at 60% solvent B for 13.6 min. A total of
1223 96 individual equal volume fractions were collected across the gradient and subsequently pooled by
1224 concatenation into 24 fractions. For batch 3, dried samples were re-suspended in high pH loading buffer
1225 (0.07% vol/vol NH_4OH, 0.045% vol/vol FA, 2% vol/vol ACN) and loaded onto a Waters BEH 1.7 um 2.1mm
1226 by 150mm. A Thermo Vanquish was used to carry out the fractionation. Solvent A consisted of 0.0175%
1227 (vol/vol) NH_4OH, 0.01125% (vol/vol) FA, and 2% (vol/vol) ACN; solvent B consisted of 0.0175% (vol/vol)
1228 NH_4OH, 0.01125% (vol/vol) FA, and 90% (vol/vol) ACN. The sample elution was performed over a 25 min
1229 gradient with a flow rate of 0.6 mL/min. A total of 192 individual equal volume fractions were collected
1230 across the gradient and subsequently pooled by concatenation into 96 fractions. All fractions were dried
1231 to completeness using a SpeedVac.
1232 Liquid Chromatography Tandem Mass Spectrometry
1233 For batches 1 and 2, each of the 24 high-pH peptide fractions was resuspended in loading buffer (0.1% FA,
1234 0.03% TFA, 1% ACN). Peptide eluents were separated on a self-packed C18 (1.9 µm Dr. Maisch, Germany)
1235 fused silica column (50 cm × 75µM internal diameter (ID), New Objective, Woburn, MA) by an Easy nLC
1236 1200 (Thermo Scientific) and monitored on a Q-Exactive HFX mass spectrometer (Thermo Scientific).

1237 Elution was performed over a 120-min gradient at a rate of 250 nL/min or 300 nL/min with buffer B ranging
1238 from 3% to 50% (buffer A: 0.1% FA in water, buffer B: 0.1 % FA in 80% ACN). For batch 1, the mass
1239 spectrometer was set to acquire data in positive ion mode using data-dependent acquisition with top 20
1240 cycles. Each cycle consisted of one full MS scan followed by a maximum of 20 MS/MS. Full MS scans were
1241 collected at a resolution of 120,000 (400-1600 m/z range, 1×10^6 AGC, 100 ms maximum ion injection
1242 time). All higher energy collision-induced dissociation (HCD) MS/MS spectra were acquired at a resolution
1243 of 45,000 (1.6 m/z isolation width, 0.5 m/z offset, 32% collision energy, 1×10^4 AGC target, 86 ms
1244 maximum ion time). Dynamic exclusion was set to exclude previously sequenced peaks for 20 seconds
1245 within a 10-ppm isolation window. For batch 2, the mass spectrometer was set to acquire data in positive
1246 ion mode using data-dependent acquisition with top 10 cycles. Each cycle consisted of one full MS scan
1247 followed by a maximum of 10 MS/MS. Full MS scans were collected at a resolution of 120,000 (400-1600
1248 m/z range, 3×10^6 AGC, 100 ms maximum ion injection time). All higher energy collision-induced
1249 dissociation (HCD) MS/MS spectra were acquired at a resolution of 45,000 (1.6 m/z isolation width, 0.5
1250 m/z offset, 30% collision energy, 1×10^4 AGC target, 86 ms maximum ion time). Dynamic exclusion was
1251 set to exclude previously sequenced peaks for 20 seconds within a 10-ppm isolation window.
1252 For batch 3, each of the 96 high-pH fractions was resuspended in loading buffer (0.1% FA, 0.03% TFA, 1%
1253 ACN). Peptide eluents were separated on a self-packed C18 (1.7 µm Water's BEH) fused silica column
1254 (laser pulled 15 cm × 150µM ID) by Ultimate 3000 RSLCnano (Thermo Scientific). Elution was performed
1255 over a 36-min gradient at a rate of 1ul/min with buffer B ranging from 3% to 50% (buffer A: 0.1% FA in
1256 water, buffer B: 0.1 % FA in 80% ACN). Mass spectrometry was performed with a high-field asymmetric
1257 waveform ion mobility spectrometry (FAIMS) Pro frontend equipped Orbitrap Eclipse (Thermo) in positive
1258 ion mode using data-dependent acquisition with 1.5 second top speed cycles for each FAIMS
1259 compensative voltage (CV). Each cycle consisted of one full MS scan followed by as many MS/MS events
1260 that could fit within the given 1.5 second cycle time limit. MS scans were collected at a resolution of
1261 120,000 (410-1600 m/z range, 4x10^5 AGC, 50 ms maximum ion injection time, FAIMS CV of -45 and -65).
1262 Only precursors with charge states between 2+ and 6+ were selected for MS/MS. All higher energy
1263 collision-induced dissociation (HCD) MS/MS spectra were acquired at a resolution of 30,000 (0.7 m/z
1264 isolation width, 35% collision energy, 1.25^5 AGC target, 54 ms maximum ion time, turboTMT on).
1265 Dynamic exclusion was set to exclude previously sequenced peaks for 20 seconds within a 10-ppm
1266 isolation window.
1267 Proteome Identification and Quantification with Proteome Discoverer
1268 All raw files were analyzed using Proteome Discoverer v2.5.0.400 (ThermoFisher Scientific). MS/MS
1269 spectra were compared to theoretical spectra in a search performed by the Sequest HT search engine,
1270 with parameters specified as: fully tryptic specificity, a maximum of two missed cleavages, a minimum
1271 peptide length of six, fixed modifications for TMT or TMTPro tags on lysine residues and peptide N-termini
1272 (respectively +229.163 or +304.207 Da), carbamidomethylation of cysteine (+57.021 Da), and dynamic
1273 modification of methionine oxidation (+15.995 Da) and N-terminal protein loss of methionine, methionine
1274 loss plus acetylation, or acetylation (-131.040 Da, -89.030 Da, or +42.011 Da, respectively); precursor mass
1275 tolerance was 20 ppm, and Fragment tolerance 0.05 Da. The FASTA database searched was downloaded
1276 from UniProt on August 15, 2020, and contained 91,413 entries, plus one added for human amyloid beta
1277 residues 6-28 (HDSGYEVHHQKLVFFAEDVGSNK). Correction for stable isotope labeling impurity of the TMT
1278 tags used in each of the 3 batches was performed. Proteins reported in the consensus workflow were
1279 filtered by Percolator to 0.005 FDR-passed 1,266,002 PSMs, 0.01 FDR-passed 310,145 peptide groups, and
1280 0.05 FDR-passed 49,656 proteins, including decoys in each case. Strict parsimony principles were followed
1281 to group peptides into proteins so that 11,681 protein parsimony groups represent the full results. A
1282 complete protein-level TMT reporter normalized abundance table is available in Table S3.
1283 Bioinformatic Analyses

Circular heatmap plot of eigenprotein-trait correlations (bicor), native eigenprotein -$\log_{10}$(p) for signed significance of AD vs control or synthetic eigenprotein Tg vs WT comparison, and the -$\log_{10}$(BH FDR) of cell type marker enrichment from the one-tailed Fisher's test p value was visualized using the R circlize package suite of functions using an in-house script. Synthetic eigenprotein calculations used the top 20 percent of hubs ranked by kME, a minimum of 4 hubs per module, calculating the first principal component of variance in those hubs [9] after mapping cross-species using the biomaRt R package getLDS function. Effect size correlation plots leveraged the WGCNA verboseScatterplot function for Pearson rho, least squares fit line, and Student's significance of the Pearson correlation. Boxplots were drawn using the base R boxplot function, with individual points overlain using the beeswarm package function of the same name. The stacked bar plot of percent differentially expressed proteins per module was executed using the DEXpercentStacked function available from https://www.github.com/edammer/parANOVA/ . Ensemble human AD GWAS MAGMA p values (Table S1) were determined as the mean -$\log_{10}$(p) gene-level risk for all genes reaching nominal significance in any of the three GWAS studies considered [43-45], following rollup of SNP-level GWAS summary statistics to the gene-level p value using MAGMA v1.09b.

Gene Ontology Analyses.

Gene ontology enrichment analysis were performed with goseq [123] to identify enrichment in gene ontology categories and KEGG pathways. For DEGs, up- and down-regulated gene lists will be analyzed separately. For WGCNA, gene lists from each module will be used as input. Over-represented P-values will be adjusted for multiple comparisons using the Benjamini–Hochberg (BH) adjustments for controlling false-discovery rates. An enrichment score will be calculated using an observed-over-expected ratio for each gene list. GO-BP categories and KEGG pathways were plotted if their BH adjusted FDR reached >= 0.05 and the number of DEGs within each category/pathway was greater than 4. Individual GO terms were grouped based on their similarity of gene composition computed using the Jaccard similarity index where J(A,B) = |size of A intersection B| / |size of A union B|. These groupings were then expert-annotated based on the overarching main function and theme of their constituent members into supergroups. The mean enrichment and p-values for the union of all member GO terms for each supergroup were calculated for graphing.

RNA extraction, sequencing and analyses for 18M mouse brains.RNA sequencing data for TgCRND8 transgenic mice was downloaded from Synapse (doi: https://doi.org/10.7303/syn3157182). RNA was extracted using the RNeasy mini extraction kit with on-column DNase treatment (QIAGEN). RNA quantity is determined with the Qubit RNA HS assay. RNA quality will be checked via the RNA Integrity Number (RIN) on an Agilent Bioanalyzer 2100 with the Eukaryote Total RNA Nano chip. Libraries will be generated polyA enrichment using the Illumina TruSeq Stranded mRNA library prep kit. Libraries will be sequenced on paired-end, 100 bp runs on the Nextseq 2000 (Illumina) utilizing a pooling strategy that minimized batch effects from extraction, library preparation.

IFASTQ files were aligned against the mouse genome (GRCm39) and GRCm39.107 annotation using STAR [124] to generate BAM files. Gene counts were generated from BAM files using Rsamtools (https://bioconductor.org/packages/release/bioc/html/SummarizedExperiment.html) and the summarizeOverlaps function with the GenomicAlignments package v1.36.0 [125] . Differential gene expression analysis was performed with DESeq2 package v1.40.2 using the "DESeq" function with default settings [126] which fits a generalized linear model for each gene. Subsequent Wald test P-values are adjusted for multiple comparisons using the Benjamini–Hochberg method (adjusted P-value). Pair-wise changes in gene expression levels between groups were used to identify DEGs. DEGs will be defined as an absolute log2 fold change ≥0.5 and an adjusted P-value ≤0.05.IFASTQ files were aligned against the mouse genome (GRCm39) and GRCm39.107 annotation using STAR [124] to generate BAM files. Gene counts were generated from BAM files using Rsamtools (https://bioconductor.org/packages/release/bioc/html/SummarizedExperiment.html) and the summarizeOverlaps function with the GenomicAlignments package v1.36.0 [125] . Differential gene

expression analysis was performed with DESeq2 package v1.40.2 using the “DESeq” function with default settings [126] which fits a generalized linear model for each gene. Subsequent Wald test P-values are adjusted for multiple comparisons using the Benjamini–Hochberg method (adjusted P-value). Pair-wise changes in gene expression levels between groups were used to identify DEGs.

AMP-AD brain transcriptome and proteomic datasets. Brain transcriptome dataset from Mayo Clinic on the AD Knowledge Portal was utilized for human vs mouse DEG comparisons). Human and CRND8 mouse brain RNA sequencing data was downloaded from Synapse (doi: https://doi.org/10. 7303/syn5550404; https://www.synapse.org/#!Synapse:syn17008858). Mayo RNAseq dataset comprises transcriptome measures from temporal cortex (TCX, superior temporal gyrus) and cerebellum (CER) the former of which was utilized in this study. For Non-Tg mice and CRND8 mice a sagitally dissected whole hemibrain was used. RNA isolation, data collection, sequencing alignment, counting and QC has been described in detail elsewhere [12,30,76]. EdgeR was used to reprocess both the mouse and human RNA sequencing data [127]. Mouse and human orthologues were identified in a two-step process. Most orthologous genes were first identified using http://alliancegenome.org/downloads, Database Version: 5.4.0 on Apr 20, 2023, with "Orthology Filter: Stringent". Then a manual curation of additional orthologues was conducted using the gOrth serac function on the g:profiler website (https://biit.cs.ut.ee/gprofiler/orth). Human brain proteomic data was utilized form previous publications. The human proteome data is available at Synapse (https://www.synapse.org/#!Synapse:syn20933797/wiki/596247).

1351 **FIGURE LEGENDS**
1352
1353 **Figure 1. TMT-MDS analysis and gene ontologies of CRND8 mice versus non-Tg brains.**
1354 (A) Volcano plot of the 6M CRND8 cohort.
1355 (B) Volcano plot of the 12M CRND8 cohort.
1356 (C) Volcano plot of the 18M CRND8 cohort.
1357 (D) Correlation of CRND8 brain DEPs between the 12M (x) and 18M cohorts (y).
1358 (E) Thematic grouping of gene ontology categories of DEPs increased in all CRND8 cohorts.
1359 (F) Thematic grouping of gene ontology categories of DEPs decreased in all CRND8 cohorts.
1360 (G) Thematic grouping of gene ontology categories of DEPs (log 2 Fc > 0.2) and increased by >2 fold in the
1361 18M CRND8 cohort relative to the 6M cohort.
1362 (H) Thematic grouping of gene ontology categories of DEPs (log 2 Fc > 1) and increased by >2 fold in the
1363 18M CRND8 cohort relative to the 6M cohort.
1364 (I) Thematic grouping of gene ontology categories of DEPs (log 2 Fc < -0.1) and decreased by >2 fold in the
1365 18M CRND8 cohort relative to the 6M cohort.
1366 Lists of all genes used for the gene ontology analyses are provided in Table S7.
1367
1368 **Figure 2. Integrated mouse and human brain proteome comparison reveals concordant and discordant**
1369 **changes between CRND8 mice brains and human AD.**
1370 (A) 7588 mouse orthologs of human brain proteins quantified in both proteomes of the consensus human
1371 AD brain proteome (AD vs. Ctrl) and the 18M mice (CRND8 Tg vs non-Tg) are compared by their effect size
1372 (log 2 Fc) in human (x) vs. mouse (y). Red numbers indicate number of proteins in each quadrant.
1373 (B) Proteins in panel A were filtered to retain only orthologs nominally significantly changed in both human
1374 and the 18M mice.
1375 (C) 6794 mouse orthologs of human brain proteins quantified in both proteomes of the consensus human
1376 AD brain proteome (AD vs. Control) and the 6M mice (CRND8 Tg vs non-Tg) are compared by their effect
1377 size in human (x) vs. mouse (y).
1378 (D) Proteins in panel C were filtered to retain only orthologs nominally significantly changed in both
1379 human and the 6M mice.
1380 (E) Overview of human consensus brain proteome mapping to the CRND8 mouse brain shows trait
1381 correlations in human (outer two tracks; red, positive correlation to white, no correlation, to blue,
1382 negative correlation), effect size directionality and significance for AD (third track from the outside), the
1383 effect size directionalities and significance for CRND8 Tg vs. non-Tg at 6M, 12M, and 18M in cognate
1384 mouse synthetic modules (Synth eigenproteins, EP), and hypergeometric overlap significance with cell
1385 type marker lists, indicating cell type enrichment of modules in the innermost track. Modules are
1386 numbered M1 to M44, ordered by bicor correlation relatedness (dendrogram), from M6, top left, to M37,
1387 top right, in a counterclockwise direction.
1388 (F) The 44 consensus modules were assessed for fraction of module member proteins achieving
1389 differentially expressed protein (DEP) status, discerning decreased DEPs in disease or Tg as blue, and
1390 increased DEPs as red in a stacked bar chart. Human and mouse bars for each module are shown side-by-
1391 side, left and right, respectively, above each module description. Descriptions below the numbered
1392 identifiers match the order of modules presented in the previous panel (*arrow*). The color of description
1393 text indicates concordant increases (red), decreases (blue), discordant in direction of change (gold), or
1394 non-concordant (black).
1395 (G) Mouse orthologs CRND8 18M Tg vs. non-Tg effect sizes are compared to the AD vs. Control effect sizes,
1396 module by module, with selected modules shown here. Pearson correlation rho and Student's significance
1397 of correlation are provided along with the number of orthologues mapping to each consensus module
1398 plotted. Text color of each module plot title matches the scheme described for the previous panel.

1399 **Figure 3. Consensus human AD brain synthetic module eigenproteins in mouse show transient and/or**
1400 **progressive CRND8 Tg effects more robust than those attributable to human AD.**
1401 Nine consensus human modules are shown for the network of healthy control, pathology-bearing
1402 asymptomatic AD (AsymAD), and symptomatic AD (AD) individuals totaling N=488 (*left panels*). To the
1403 right, the mouse orthologs of hub proteins for these modules were used to calculate the first principal
1404 component of variance in the 6M, 12M, and 18M mouse proteomes, allowing for extrapolation of the
1405 modules into Tg and non-Tg mice, determination of effect size by module in each mouse cohort, and the
1406 significance of Tg effect within each module. Significant one-way ANOVA p values are colored red. Note
1407 the Y-axis are different across ages, and in many modules the eigneprotin change between Tg and non-Tg
1408 mice increases dramatically with age.
1409
1410 **Figure 4. Mdk/MDK and Ptn/PTN colocalize with Aβ in amyloid plaques and CAA in CRND8 mice and**
1411 **human AD.**
1412 (A) Paraffin slides containing brain tissue from 15-18M CRND8 mice were stained with mouse anti-pan-
1413 Aβ, sheep anti-Mdk or rabbit anti-Ptn antibodies. Low magnification (scale 500 μm) images and high
1414 magnification (inset, scale 50 μm) were taken from cortex (plaques) and cerebellum (CAA).
1415 (B) Representative low magnification (scale 100 μm) and high magnification (inset, scale 30 μm) of
1416 postmortem paraffin embedded tissue sections of human frontal cortex from patients with high AD
1417 neuropathological changes stained for MDK and PTN.
1418 (C) Plaques on paraffin slides containing brain tissue from old CRND8 mice were stained with anti-Mdk
1419 and anti-Ptn antibodies and visualized with fluorescent secondary antibodies (anti-rabbit green and anti-
1420 sheep red), scale 50 μm.
1421 (D) Plaques and CAA on paraffin slides containing brain tissue from old CRND8 mice were stained with
1422 anti-pan-Aβ, anti-Mdk or anti-Ptn antibodies and visualized with Thio-S (green) or fluorescent secondary
1423 antibodies (anti-mouse red, anti-rabbit red, anti-sheep red), scale 50 μm.
1424
1425 **Figure 5. M42+ DEP colocalize with amyloid pathology.**
1426 Brain tissue from 15-18M CRND8 mice were stained with the anti-sera against the indicated proteins. Anti-
1427 pan-Aβ antibody served as a reference for amyloid pathology, secondary antibody alone – as a negative
1428 control. All proteins are listed in order of log 2 Fc (highest to lowest). Low magnification (scale 200 μm)
1429 images and high magnification (inset, scale 50 μm). See Figure S7 for non-Tg staining.
1430 (A) DEPs in amyloid plaques in the CRND8 cortex.
1431 (B) DEPs detected in CAA in the cerebellum.
1432 (C) DEPs detected in dystrophic processes surrounding amyloid plaques in the cortex.
1433 (D) Representative low magnification (scale 100 μm) and high magnification (inset, scale 30 μm) of
1434 postmortem paraffin embedded tissue sections of human frontal cortex from patients with high AD
1435 neuropathological changes stained for Aβ, EGFL8, C1QTNF4, COL25A1, HGF, APOD, SDC4, NTN1, SMOC2,
1436 OLFML3, SPOCK3, SPOCK1, SULF1, SFRP5 and SFRP1. There is selective staining of plaques by antisera for
1437 COL25A1, SDC4, NTN1, SMOC2, and EGFL8. Weaker staining of plaques and cellular staining is observed
1438 for HGF, C1QTNF4 and APOD. Dystrophic processes are stained with anti-sera to SPOCK3, SPOCK1
1439 OLFML3. Glial cells are detected with anti-sera to SULF1, SRRP5 and SFRP1.
1440
1441 **Figure 6. Mdk and PTN overexpression increase parenchymal Aβ amyloid deposition and CAA in 6M**
1442 **CRND8 mice.** Mice were intracerebrally injected with rAAV2/8-Mdk, rAAV2/8-PTN or not injected
1443 (control) at P0 and aged 6 months.
1444 (A, B) Representative images of cortex and hippocampus 9A) or CAA (B) stained with biotinylated anti-Aβ
1445 mAb 33.1.1 (anti-Aβ 1-16). Scale bar: 500 μm, 50 μm (inset). Quantification data of the entire brain plaque

count in three non-consecutive sections represented by a scatter dot plot of male (closed circle/square) and female (open circle/square) ± standard error of the mean. n=5-15. Statistical analyses by one-way ANOVA test (*, $p<0.05$; ***, $p<0.001$).

(C) RIPA, 2% SDS and 70% formic acid (FA) extracted Aβ42 and Aβ40levels were detected by ELISA and plotted as scatter dot plot of male (closed circle/square) and female (open circle/square) ± standard error of the mean. n=5-12. Aβ42 and Aβ40 levels were quantified with corresponding one-way ANOVA and paired comparison test (*, $p<0.05$; **, $p<0.01$, ***, $p<0.001$).

(D) MDK and PTN accelerate amyloid aggregation in vitro as detected by real time Thioflavin T (ThT) assay.

Figure 7. Amyloid binding and co-localization in TTR amyloids.

(A) M42+ proteins secreted into the media of transiently transfected HEK cells bind to Aβ42 and AVS amyloids. Data are representative of three independent experiments.

(B) Representative images of immunohistochemical stains for MDK, PTN or Thio-S on human cardiac amyloidosis sections. Scale bar, 50 µm.

ACKNOWLEDGEMENTS

Availability of data and materials

Raw mass spectrometry data and pre- and post-processed plasma protein abundance data and case traits related to this manuscript are available at https://synapse.org/CRND8. The results published here are in whole or in part based on data obtained from the AMP-AD Knowledge Portal (https://adknowledgeportal.synapse.org). The AMP-AD Knowledge Portal is a platform for accessing data, analyses and tools generated by the AMP-AD Target Discovery Program and other programs supported by the National Institute on Aging to enable open-science practices and accelerate translational learning. The data, analyses and tools are shared early in the research cycle without a publication embargo on secondary use. Data are available for general research use according to the following requirements for data access and data attribution (https://adknowledgeportal.synapse.org/#/DataAccess/Instructions).

AD Knowledge Portal: AMP-AD datasets: The results published here are in whole or in part based on data obtained from the AMP-AD Knowledge Portal (doi:https:// doi. org/ 10. 7303/ syn25 80853). Mayo Clinic: The Mayo RNAseq study data was led by Dr. Nilüfer Ertekin-Taner, Mayo Clinic, Jacksonville, FL as part of the multi-PI U01 AG046139 (MPIs Golde, Ertekin-Taner, Younkin, Price). Samples were provided from the following sources: The Mayo Clinic Brain Bank and Banner Sun Health Research Institute. Data collection was supported through funding by NIA grants P50 AG016574, R01 AG032990, U01 AG046139, R01 AG018023, U01 AG006576, U01 AG006786, R01 AG025711, R01 AG017216, R01 AG003949, NINDS grant R01 NS080820, CurePSP Foundation, and support from Mayo Foundation. Study data includes samples collected through the Sun Health Research Institute Brain and Body Donation Program of Sun City, Arizona. The Brain and Body Donation Program is supported by the National Institute of Neurological Disorders and Stroke (U24 NS072026 National Brain and Tissue Resource for Parkinson's Disease and Related Disorders), the National Institute on Aging (P30 AG19610 Arizona Alzheimer's Disease Core Center), the Arizona Department of Health Services (contract 211002, Arizona Alzheimer's Research Center), the Arizona Biomedical Research Commission (contracts 4001, 0011, 05-901 and 1001 to the Arizona Parkinson's Disease Consortium) and the Michael J. Fox Foundation for Parkinson's Research. For the human protein data All raw data, case traits and analyses (differential and co-expression) related to this manuscript are available at https://www.synapse.org/consensus. The results published here are in whole or in part based on data obtained from the AMP-AD Knowledge Portal (https://adknowledgeportal.synapse.org). The AMP-AD Knowledge Portal is a platform for accessing data,

analyses, and tools generated by the Accelerating Medicines Partnership (AMP-AD) Target Discovery Program and other National Institute on Aging (NIA)-supported programs to enable open-science practices and accelerate translational learning. The data, analyses and tools are shared early in the research cycle without a publication embargo on secondary use. Data is available for general research use according to the following requirements for data access and data attribution (https://adknowledgeportal.synapse.org/#/DataAccess/Instructions). ROSMAP resources can be requested at www.radc.rush.edu.

ACKNOWLEDGEMENTS

Author contributions: Conceptualization, TEG, NTS, SP, AIL, YL, ECBJ, ED; Methodology, TEG, YL, YR, DD, JG, NTS, MA, KD, DR, JT, CM, LP, AI, AE, BDM, KDD, AN, TI, FA, TL, KM, BM, MR, CF; Investigation, YL, EBD, YR, WT, DD, MA, JG, KL , JT-L, JP, AI, AE, BM, KM, AN; Formal Analysis, YL, KM, EBD, MR, CF, NTS, TEG, AN; Writing – Original Draft, TEG, YL, SP; Writing – Review & Editing, YL, EBD, DD, NET, JWK, AIL, KM, NTS, TEG, SP, FLH; Funding Acquisition, TEG, SP, NTS, YL AIL and; Resources, AIL, JWK, NTS, SP, TEG, ECBJ, FLH, JWK, JJ; All authors read and approved the final manuscript.

Funding: This study was supported by the following National Institutes of Health (NIH) funding mechanisms: P30AG066506, U01AG061357, U01AG046139 (TEG and NET), U01AG061357, RF1AG074569 (AIL and NTS), RF1AG062181 (NTS) and P30AG066511 (AIL) and the Foundations for the National Institute of Health AMP-AD 2.0 grant. This work was supported by the Deutsche Forschungsgemeinschaft (DFG, German Research Foundation) under Germany's Excellence Strategy NeuroCure– EXC-2049 – 390688087 to F.L.H., as well as HE 3130/6-1 to F.L.H. Additional support for these studies was provided by the NIA grants R01-AG061796 (NET), U19-AG074879 (NET), Alzheimer's Association Zenith Fellows Award (NET).

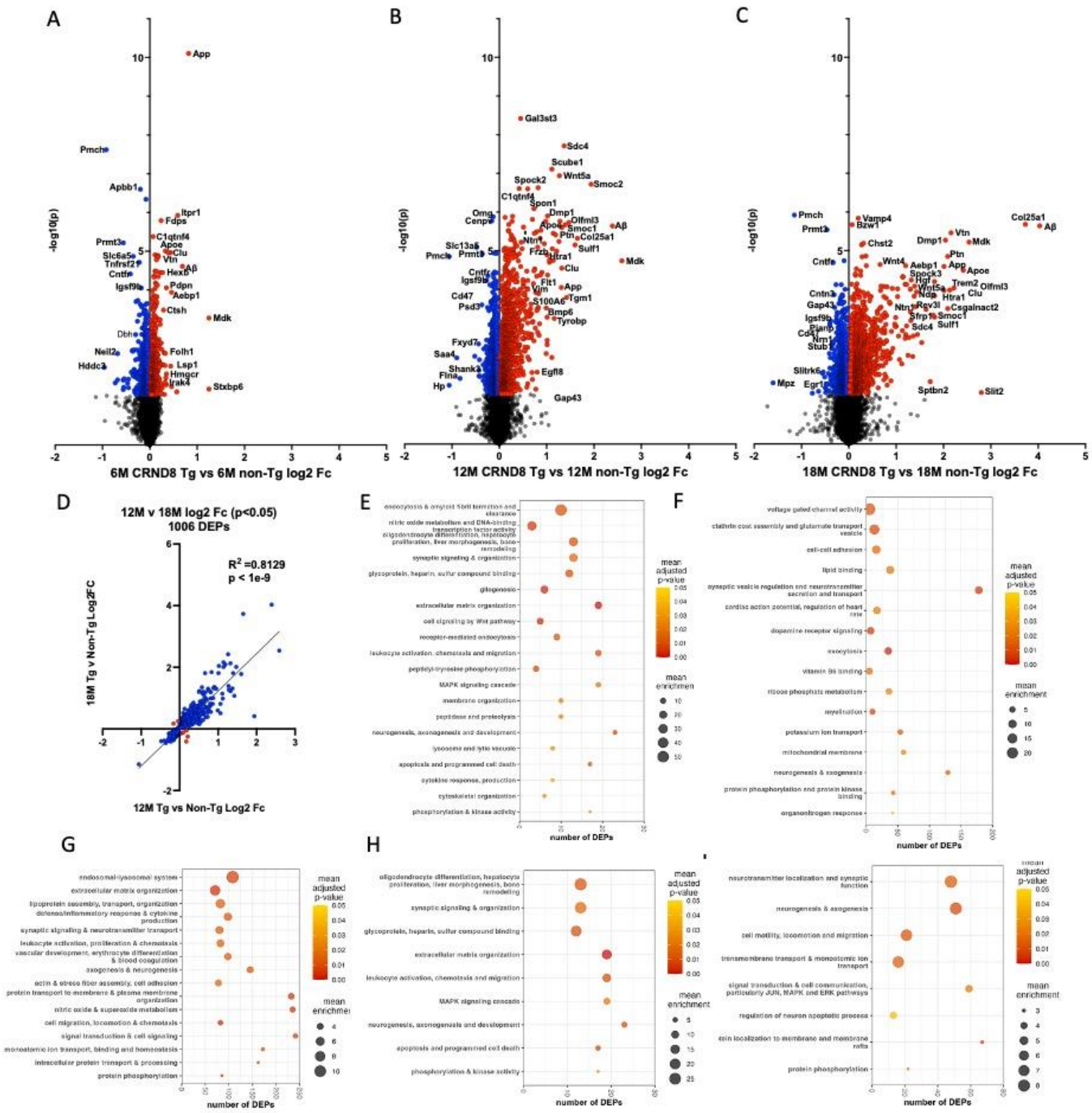

Figure 1. TMT-MDS analysis and gene ontologies of CRND8 mice versus non-Tg brains.

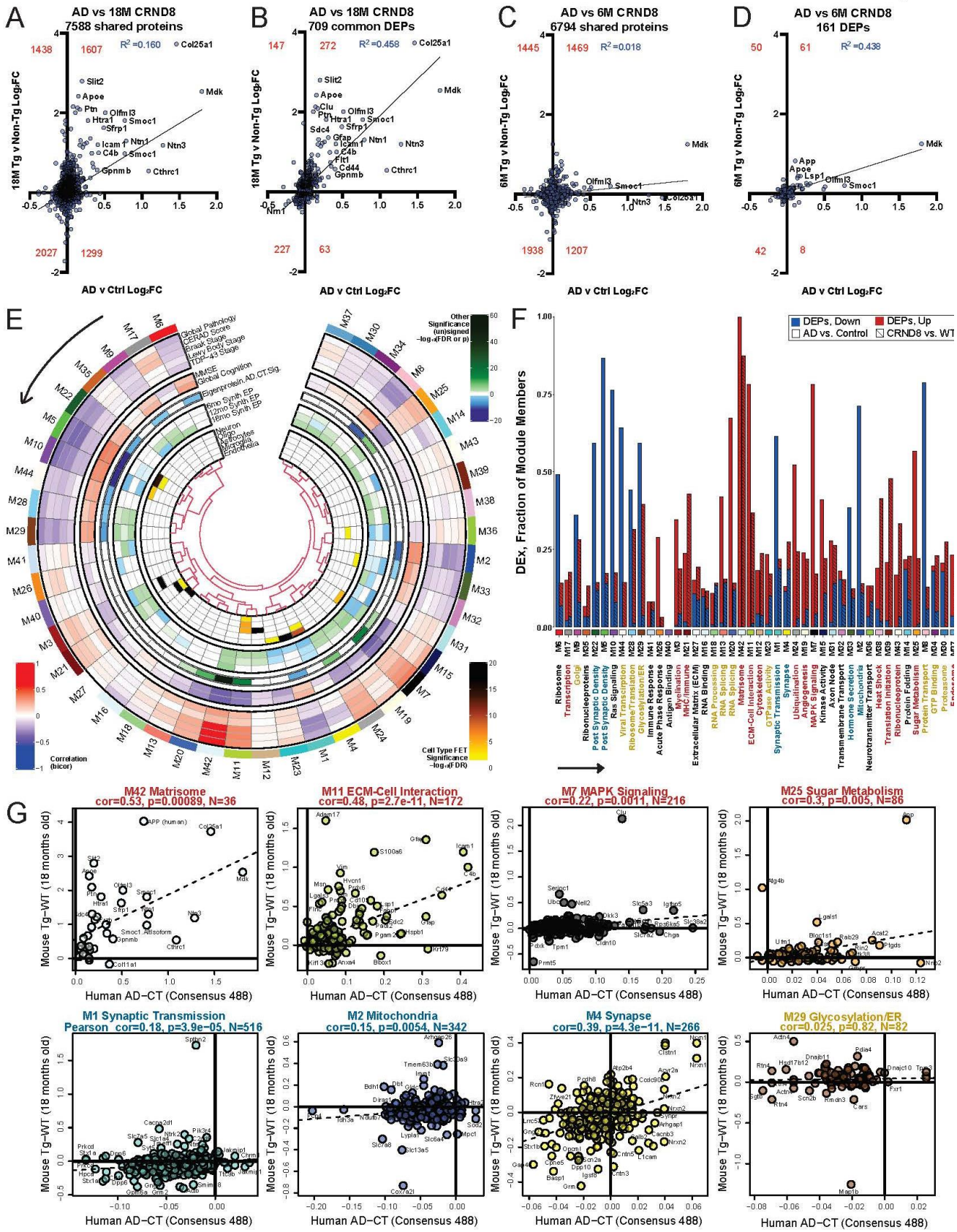

Figure 2. Integrated mouse and human brain proteome comparison reveals concordant and discordant changes between CRND8 mice brains and human AD.

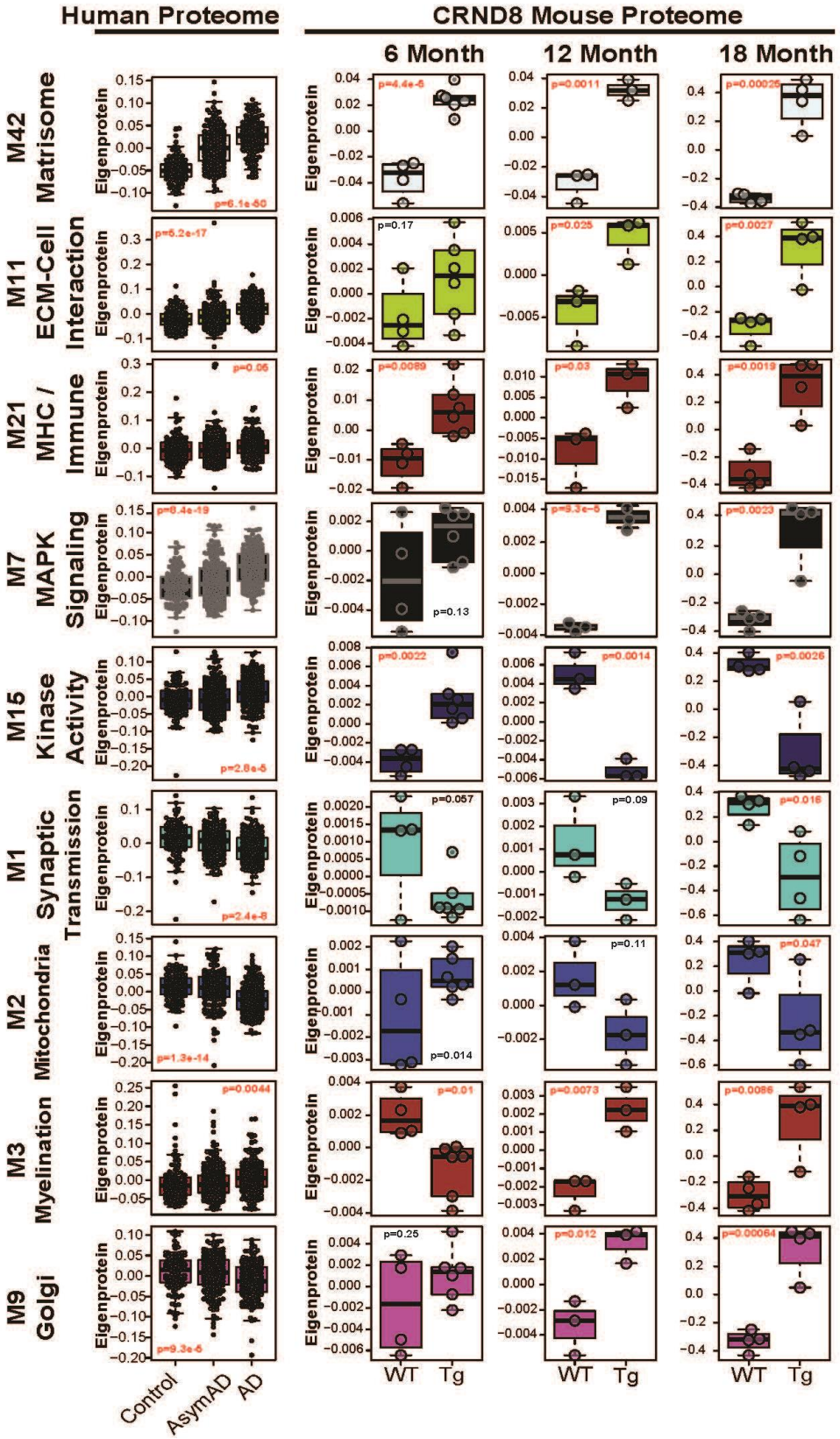

Figure 3. Consensus human AD brain synthetic module eigenproteins in mouse show transient and/or progressive CRND8 Tg effects more robust than those attributable to human AD.

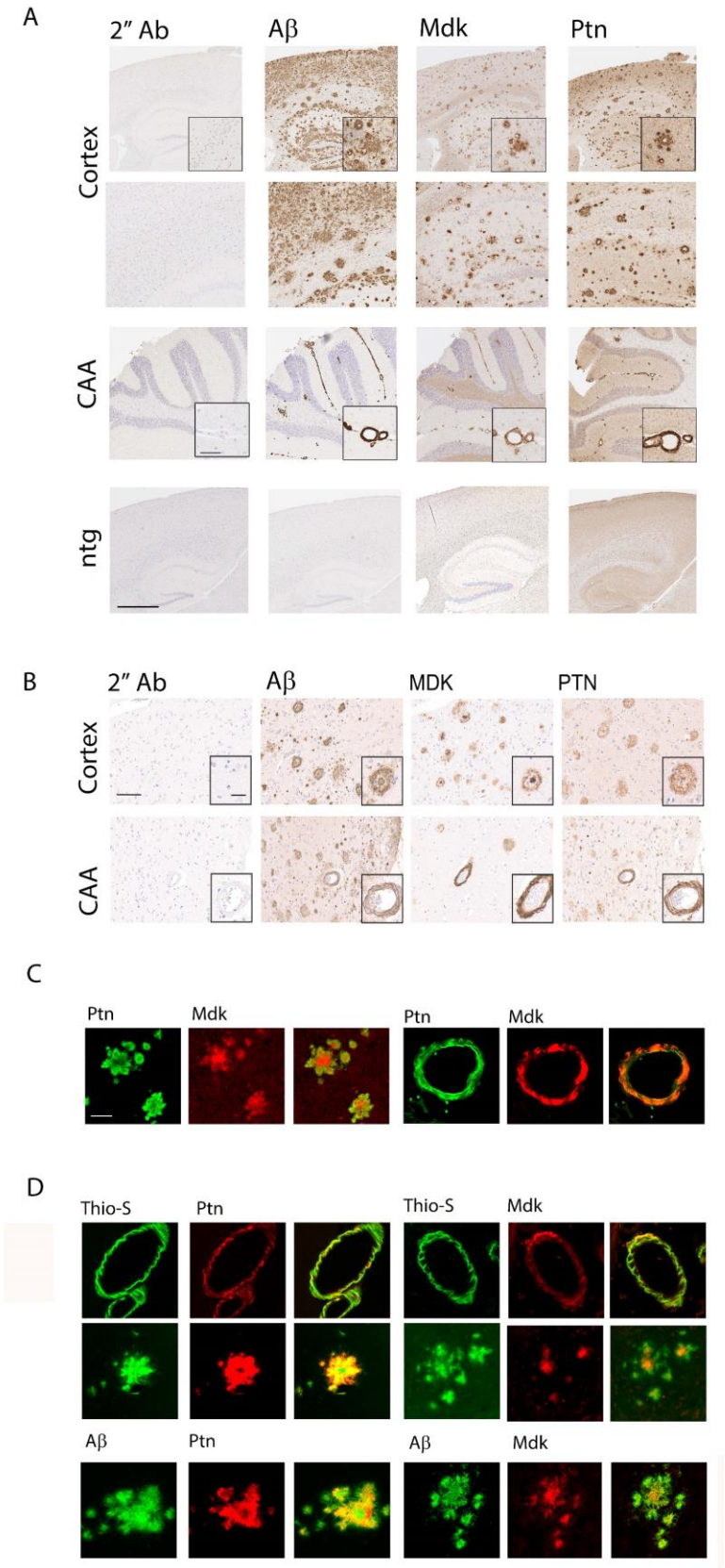

Figure 4. Mdk/MDK and Ptn/PTN colocalize with Aβ in amyloid plaques and CAA in CRND8 mice and human AD.

1

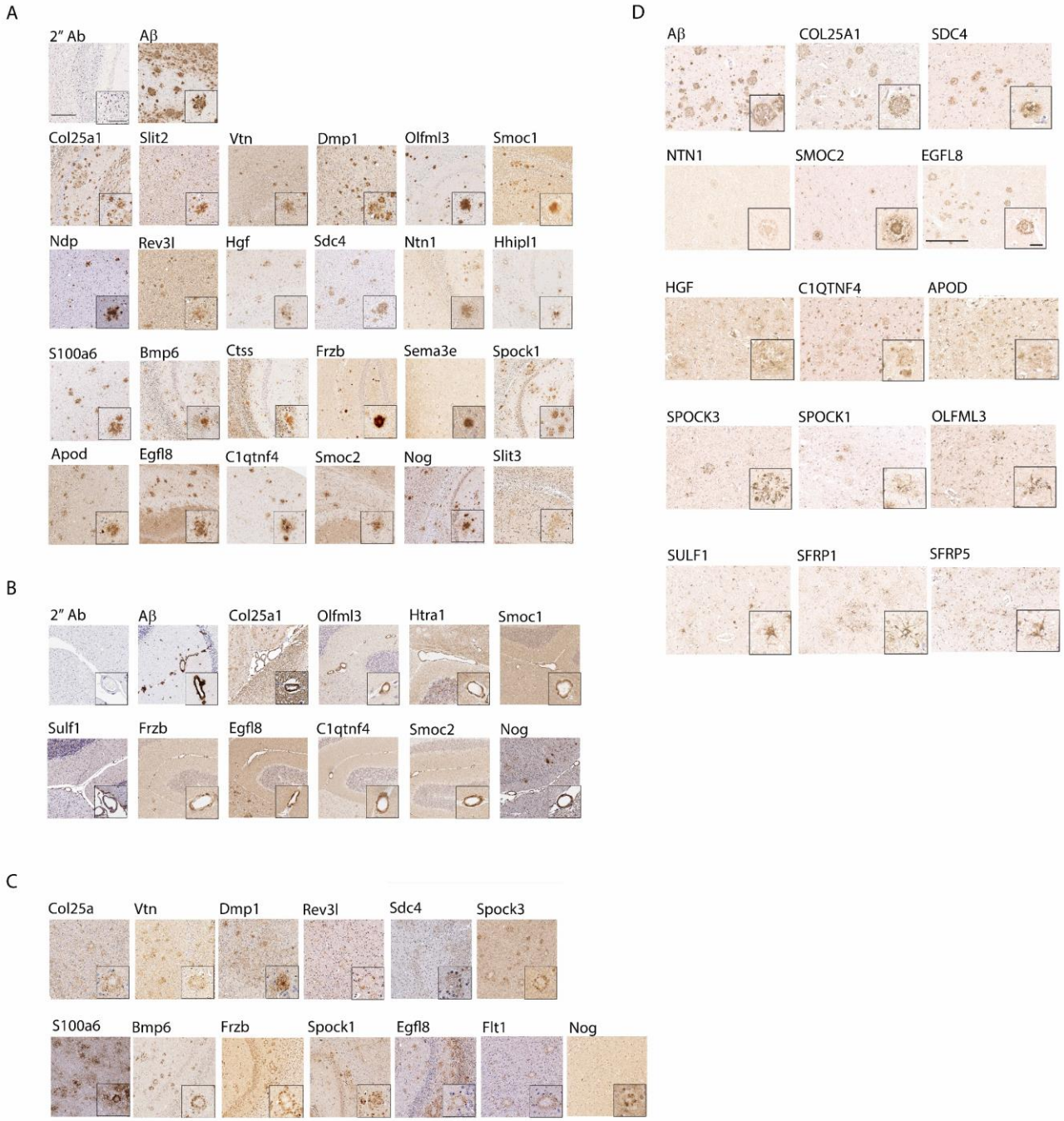

Figure 5. M42+ DEP colocalize with amyloid pathology.

1523

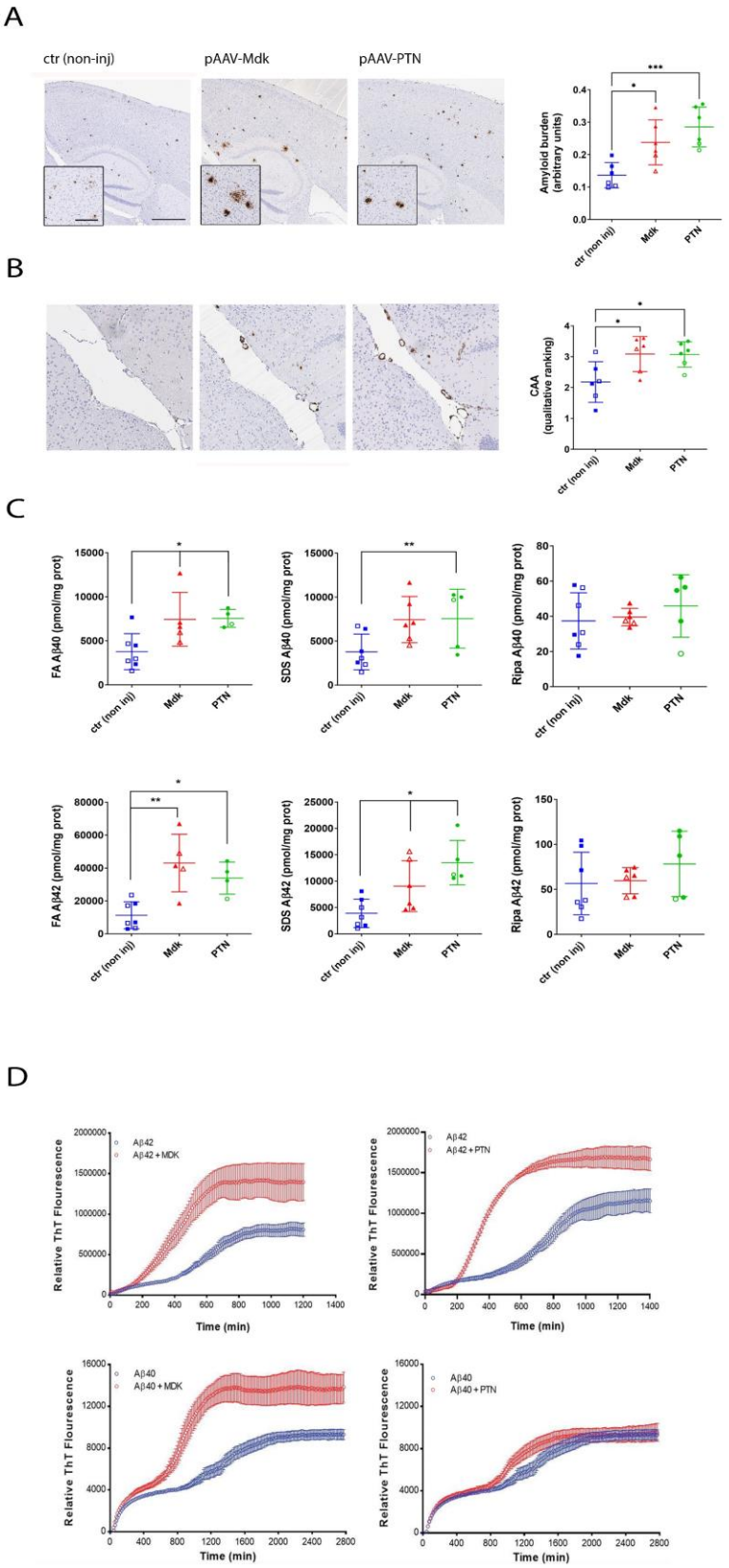

Figure 6. Mdk and PTN overexpression increase parenchymal Aβ amyloid deposition and CAA in 6M CRND8 mice.

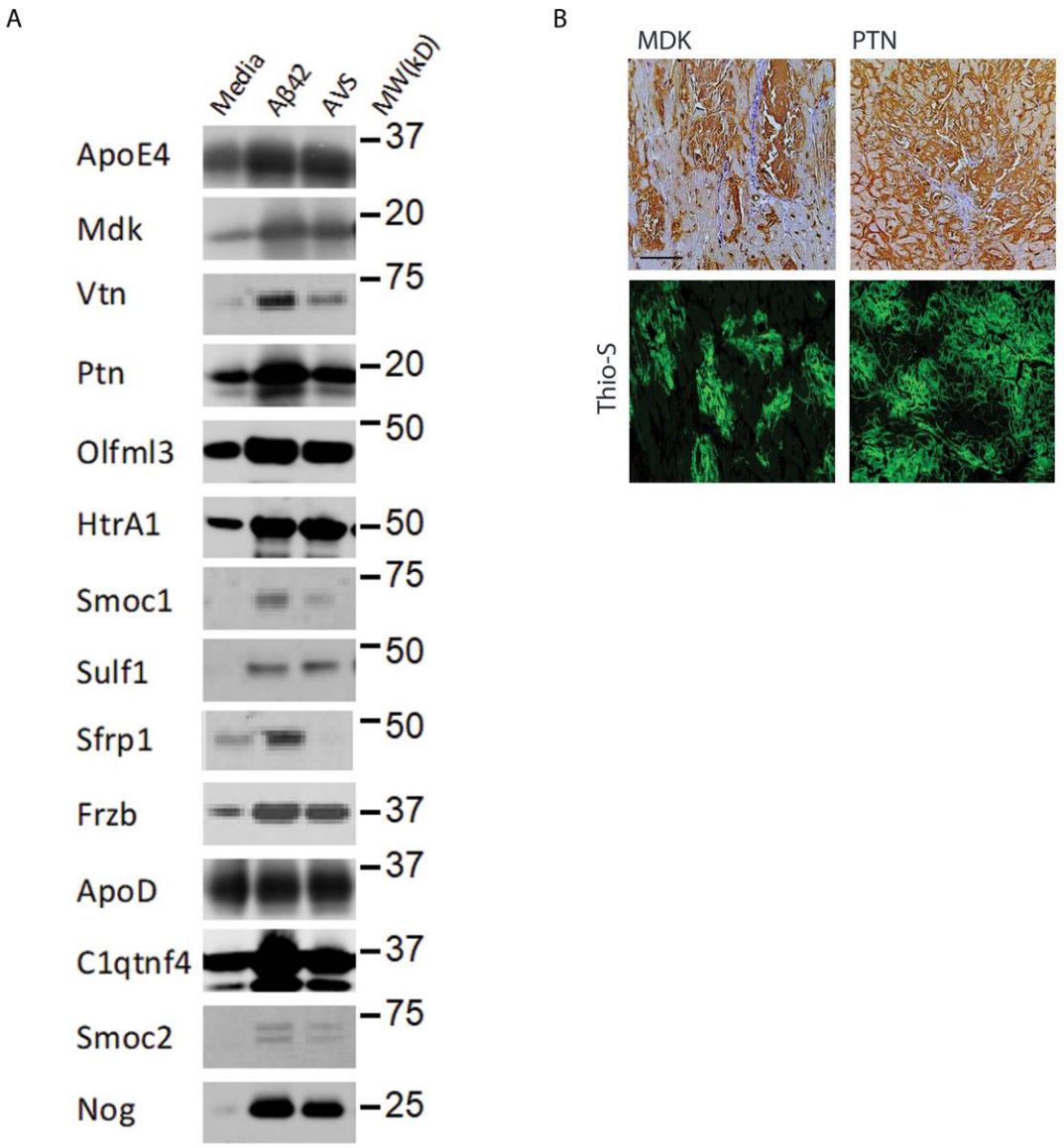

Figure 7. Amyloid binding and co-localization in TTR amyloids.

1525 Supplemental material

1526 **Figure legends**

1527 **Figure S1. Correlation of protein encoding mRNAs in 20M CRND8 mice (Tg versus non-Tg) and AD versus**
1528 **Control human Temporal Cortex.**

1529 Previously generated RNA expression data from human temporal cortex [12] and CRND8 mice brains [30] was
1530 reanalyzed using EdgeR and filtered for orthologues.

1531 (A) Plot of log2FC of human temporal cortex AD versus Control mRNA levels (x-axis) and 20M CRND8 of
1532 all orthologous protein coding RNA (y-axis).

1533 (B) Plot of log2FC of human temporal cortex AD versus Control mRNA levels (x-axis) and 20M CRND8 of
1534 all shared DEGs of protein coding genes (y-axis).

1535 Data used to generate these plots is found in Table S6.

1536

1537 **Figure S2. Effect size correlation for human AD vs control effect and mouse Tg effect at 18M shows**
1538 **varying concordance in each of the 44 consensus brain modules.**

1539 Panels are in rank size order from M1 to M44, with each title providing module number, description,
1540 Pearson correlation (rho), Student's significance of correlation, number of mouse orthologs mapped to
1541 the members of the human module, and all points labeled by the gene symbol of the mouse ortholog.
1542 *Modules also displayed in Figure 2 are labeled with an asterisk. Text color of each module plot title
1543 matches the scheme described in Figure 2F.

1544

1545 **Figure S3. Synthetic eigenproteins (modules) show trends across the three cohorts of aged Tg and non-**
1546 **Tg mice for all 44 consensus brain modules.** All 44 human modules were calculated as synthetic
1547 eigenproteins in the mouse proteomics and plotted as boxplots. Boxes represent the second to third
1548 interquartile range; whiskers represent the 5th to 95th percentiles; and the horizontal line within each box
1549 represents the median value.

1550

1551 **Figure S4. RNA-Protein AD or Tg Effect Size Correlation, in total and within modules.**

1552 (A) The correlation of Tg effect size in mouse proteome (x) to transcriptome (y) shown with a least squares
1553 trendline over a scatterplot of the effect sizes for 9319 mouse gene transcripts and corresponding proteins
1554 (Table S8). When more than one splicing isoform protein was present, the one with maximum variance
1555 was retained.

1556 (B) M42 protein (x) to transcriptome (y) effect size scatterplot with least squares trendline, Pearson
1557 correlation (rho), and Student's significance of correlation are shown for Tg vs non-Tg effect sizes (*left*),
1558 and in human AD vs. Control effect sizes (*right*).

1559 (C) M1 RNA-protein correspondence for Tg effect (*left*) and for the effect in human of AD vs. control (*right)*.

1560 (D) M21 RNA-protein correspondence for Tg effect (*left*) and for the human AD effect (*right*).

1561

1562 **Figure S5. Protein-RNA effect size correlation varies in mouse and human for all 44 consensus brain**
1563 **modules.**

1564 Gene product names label each point, with the module number (size rank), count of proteins mapped to
1565 mouse (*left*) from human (*right*), Pearson correlation rho and Student's significance of correlation given
1566 in each plot title.

1567

1568 **Figure S6. Mdk and Ptn colocalization with amyloid is age dependent, occurs in various AD transgenic**
1569 **mouse models but are enriched in soluble brain fractions.**

1570 (A) Paraffin slides containing brain tissue from 12M non-tg mice; 3, 6 and 12M CRND8 mice; 12M

1571 Tet.HuAPP, PrP.MoAβ and PrPHuAβ/PS1 mice were stained with mouse anti-pan-Aβ, sheep anti-Mdk or
1572 rabbit anti-Ptn antibodies. scale 50 mm.
1573 (B). Western blots detecting Mdk and Ptn in the urea extracts of 15M CRND8 mice and non-Tg control
1574 brains as shown by SDS-PAGE stained with anti-Mdk or anti-Ptn antibodies in total Urea extracts (first two
1575 lanes for each are male and second two lanes are females. Blots are representatives of three independent
1576 experiments.
1577 (C) Sequential extractions with TBS, RIPA, 2% SDS and 8M Urea, show that neither Mdk or Ptn become
1578 detergent insoluble. Blots are representatives of three independent experiments.
1579
1580 **Figure S7. non-Tg staining, fixation effects, co-localization, and astrocyte staining.**
1581 (A) DEP staining of 15-18M old non-Tg controls. Paraffin slides containing brain tissue from 15-18M non-
1582 Tg fixed in 4% paraformaldehyde (one hemibrain) or 10% ethanol (second hemibrain), were stained with
1583 anti-DEP antibodies. Low magnification (scale 500 μm) images were taken from cortex and hippocampus.
1584 (B) Fixation impacts localization, but impacts are dependent on the antisera used. Paraffin slides
1585 containing brain tissue from 15M CRND8 mice, fixed in 4% paraformaldehyde (one hemibrain) or 10%
1586 ethanol (second hemibrain), were stained with the indicated anti-DEP antibodies. Scale 200 μm.
1587 (C, D) Colocalization of DEP in plaques. Paraffin slides containing brain tissue from 15M TgCRND8 mice,
1588 were stained with either mouse anti-pan-Ab antibody or Thio-S and rabbit anti-DEP. Secondary
1589 fluorescent anti-mouse (green) and rabbit (red) antibodies were used. Colocalization was visualized by
1590 overlap of green and red colors to create yellow in plaques (C) or CAA (D) Scale 50 μm.
1591 (E) Select DEPs accumulate in astrocytes surrounding amyloid plaques. Paraffin slides containing brain
1592 tissue from 15-18M CRND8 mice were stained with anti-DEP antibodies. Scale 200 μm.
1593
1594 **Figure S8. Antibody validation studies and additional DEPS validated by Western blotting.**
1595 (A) Antibody validation. 293T HEK cells were transfected with plasmids containing FLAG-tagged cDNAs
1596 encoding M42+ DEP and gene expression in the media (SPOCK3, VTN, HTRA1) and lysates (all other genes)
1597 was detected on SDS-PAGE with 1 (anti-Flag) and 2 (anti-DEP sera). Non-transfected cells served as
1598 control. Representative blots of at least three independent experiments are shown. Sources of the
1599 antibodies are listed in Table S10, S11.
1600 **(**B) M42+ DEPs are detected in total UREA extracts from 15M CRND8 mice. Brain homogenates from Tg
1601 and age matched non-Tg mice were subjected to SDS-PAGE and stained with anti-DEP antibodies. (n=2;
1602 one male and one female).
1603
1604 **Figure S9. Midkine and Pleiotrophin overexpression increase formation of Aβ amyloid deposition and**
1605 **CAA in 3M CRND8 mice and 6M mouse data on gliosis.**
1606 Mice were intracerebrally injected with rAAV2/8-Mdk, rAAV2/8-PTN or not-injected (control) at P0 and
1607 aged 3 months.
1608 (A, B) Representative images of cortex and hippocampus (A) or CAA (B) stained with biotinylated anti-Aβ
1609 mAb 33.1.1 (anti-Aβ 1-16). Scale bar: 500 μm, 50 μm (inset). Quantification data of the entire brain plaque
1610 count in three non-consecutive sections represented by a scatter dot plot of male (closed circle/square)
1611 and female (open circle/square) ± standard error of the mean. n=5-15. Plaques were quantified with one-
1612 way ANOVA test (*, $p<0.05$; ***, $p<0.001$).
1613 (C) RIPA, 2% SDS and 70% formic acid (FA) extracted Aβ40 and Aβ42 levels were detected by ELISA and
1614 plotted as scatter dot plot of male (closed circle/square) and female (open circle/square) ± standard error
1615 of the mean. n=5-12. Aβ42 and Aβ40 levels were quantified with corresponding one-way ANOVA and
1616 paired comparison test (*, $p<0.05$; **, $p<0.01$, ***, $p<0.001$).

(D, E) Mdk and PTN overexpression induces astrocytosis and microgliosis in 6M CRND8 mice. Representative images of GFAP-reactive astrocyte (D) and Iba-1 reactive microglia (E) in 6-month-old TgCRND8 mice overexpressing Mdk or PTN genes. Quantitation of the Iba-1 or GFAP staining was performed in cortex and hippocampus combined area. N = 6 mice. Scale bar, 500 µm, 50 µm. Clear symbols denote female mice and filled symbols denote male mice. Data represents mean ± sem. One-way ANOVA; ***$p < 0.001$; **$p < 0.01$; *$p < 0.05$.

Figure S10. Mdk and PTN interact with heparin.
Flag-tagged Mdk and PTN secreted into the media of transiently transfected HEK cells binds to heparin-agarose beads.

Figure S11. Contextualization of CRND8 18M Proteome by integration with AD GWAS MAGMA p values and AD CSF proteomic changes.
(A) Volcano plot of log2 Fc of DEPs in the 18M CRND8 proteome versus the -log10p MAGMA AD GWAS values (Table S1). Red circles indite GWAS loci that have been prioritized for further study. Blue circles indicate M42+ DEPs that accumulate in the CRND8 proteome. APOE and CLU are denoted as known GWAS loci that accumulate with amyloid by circles with red interior with blue border.
(B) Volcano plot of the AD vs control CSF log 2 Fc derived from the Caucasian cohort in Modeste et. al 51, annotated by showing as colored symbols the overlapping DEPS in the CRND8 18M brain proteome. Red indicates a change that is concordant in direction between CSF and mouse brain. Yellow indicates a discordant change. M42 members are denoted by red squares. Grey triangles indicate significantly altered proteins in CSF that are either not detected in the 18M CRND8 proteome or not significantly changed (see Table S13).

Figure S12. A schematic illustrating the Amyloid Scaffold Hypothesis.

Supplemental Tables.

Table S1. Master stats table for all 3 age group batches, including MAGMA p values from AD GWAS and human brain data from Johnson et al[9].

Table S2. Unified 3 TMT batch traits

Table S3. TMT Normalized abundance

Table S4. TMT Normalized abundance 5% < FDR < 5%, Granular quantifications

Table S5. CRND8 3 age group batch statistics for proteins from table.

Table S6. Genes and mRNA expression (log2 Fc) from reprocessed AD TCx and 20M CRND8 mice used for Figure S1A.

Table S7. List of DEPS used in GO analysis in Figure 1.

Table S8. RNA-Seq Counts, Dispersion-normalized, with Statistics for 18M CRND8 vs 18M Non-tg

Table S9. Histopathology results summary CRND8 studies.

Table S10. Antibodies used in mice and staining conditions.

Table S11. Antibodies used in humans and staining conditions.

Table S12. List of peptides used to create new antibodies and list of antibodies/antisera that were tested from commercial sources that did not work on the pathological specimens.

Table S13. List of CSF proteins and DEPs in18M CNRD8 brains used for Figure 9B.

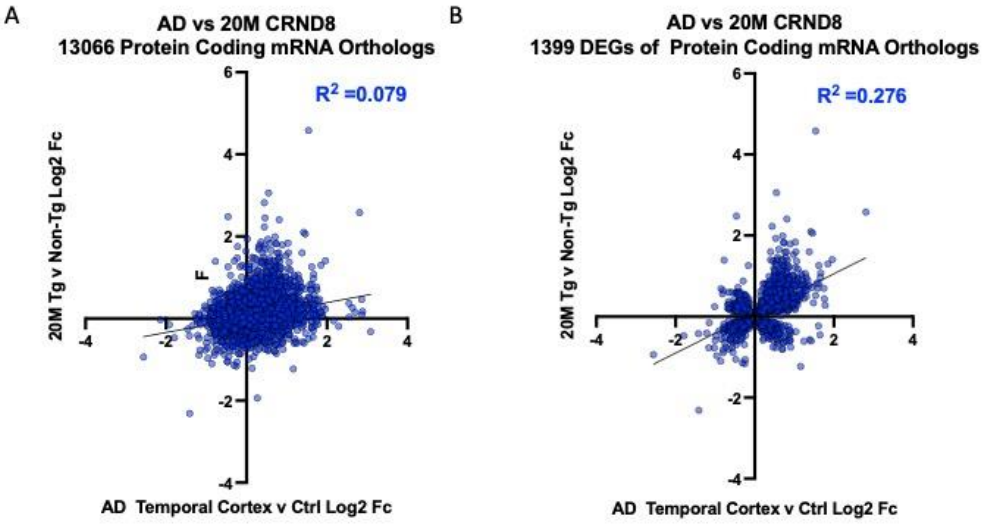

Figure S1. Correlation of protein encoding mRNAs in 20M CRND8 mice (Tg versus non-Tg) and AD versus Control human Temporal Cortex.

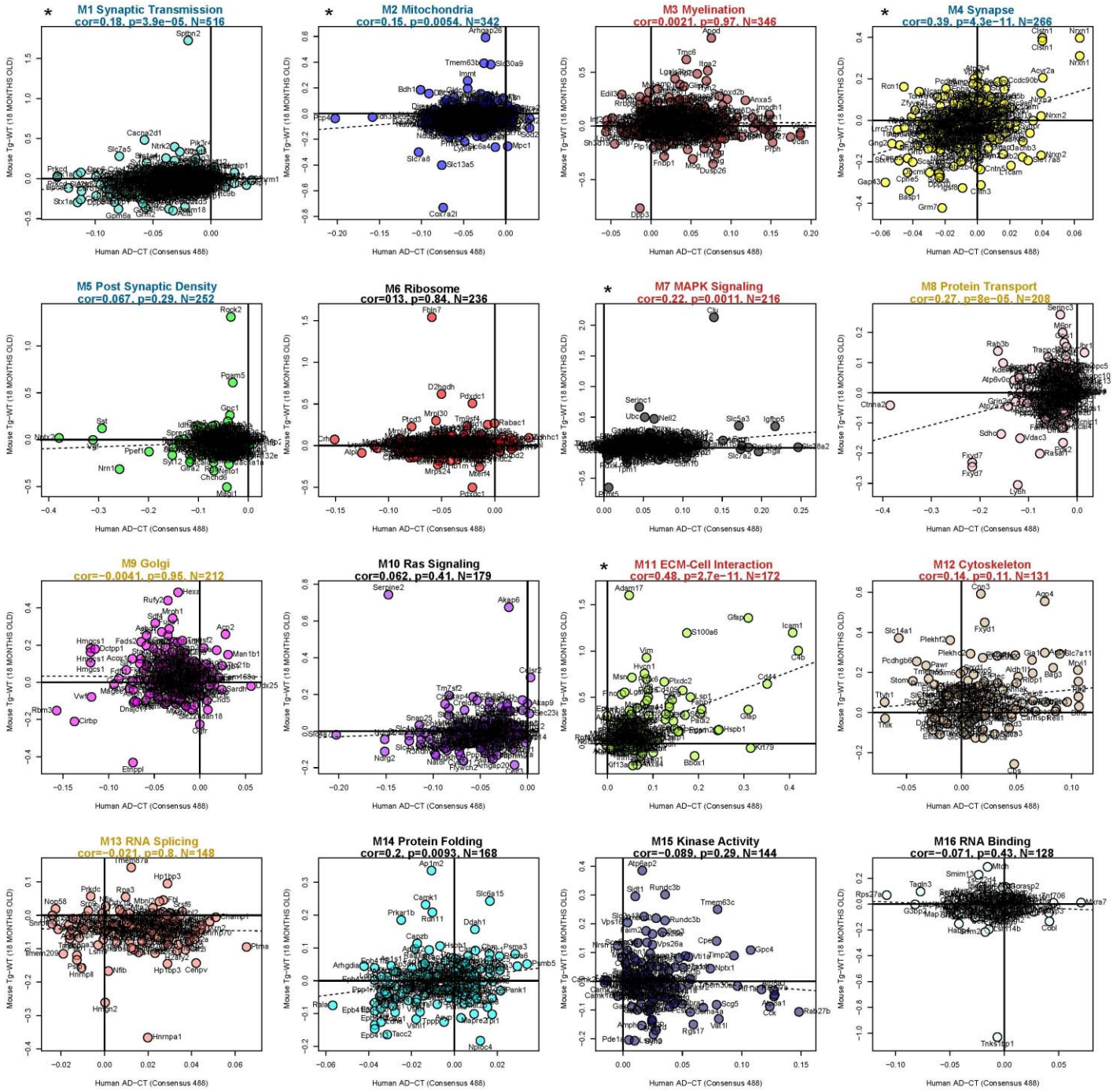

Figure S2. Effect size correlation for human AD vs control effect and mouse Tg effect at 18M shows varying concordance in each of the 44 consensus brain modules.

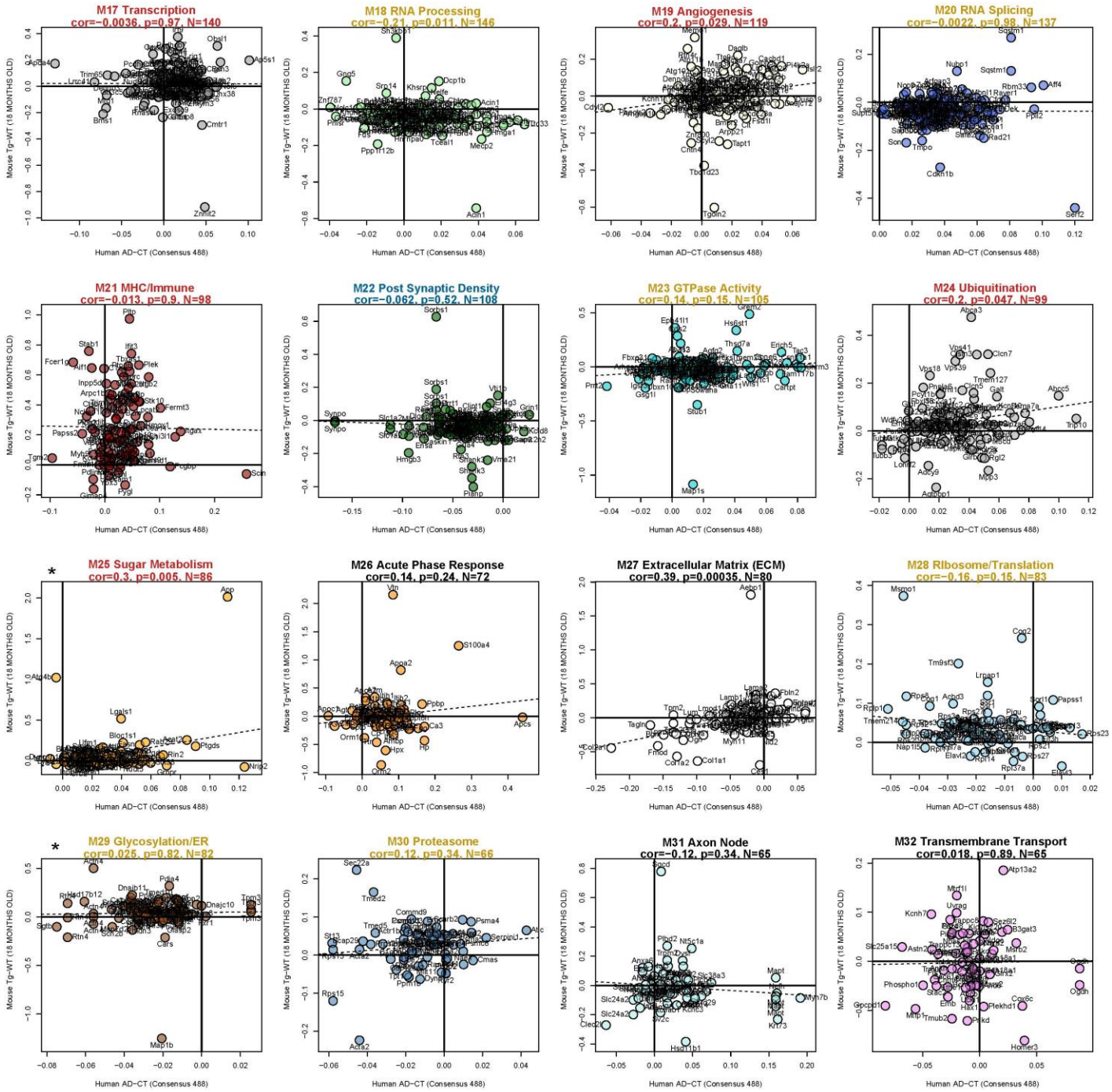

Figure S2 (cont.). Effect size correlation for human AD vs control effect and mouse Tg effect at 18M shows varying concordance in each of the 44 consensus brain modules.

1

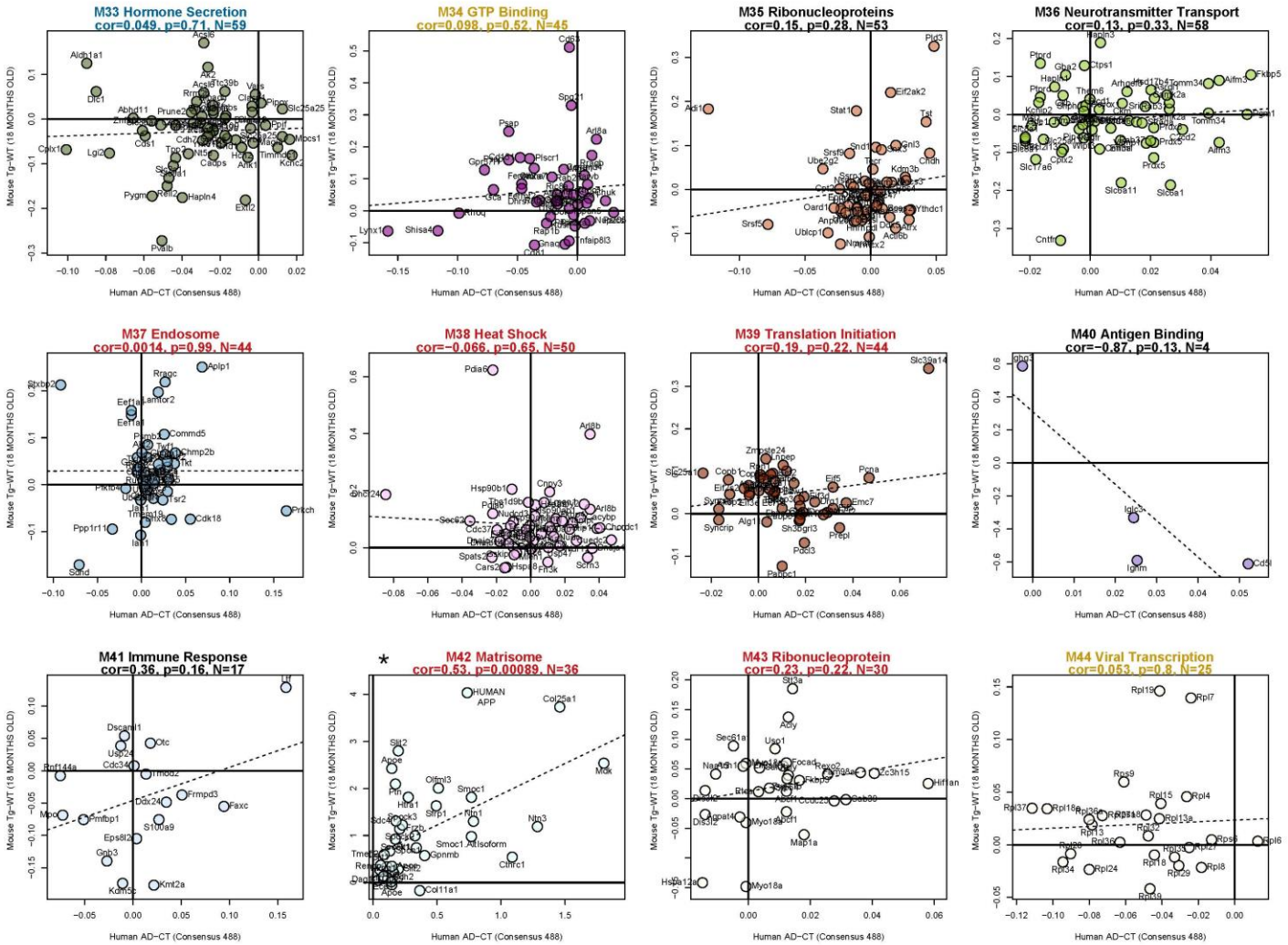

Figure S2 (cont.). Effect size correlation for human AD vs control effect and mouse Tg effect at 18M shows varying concordance in each of the 44 consensus brain modules.

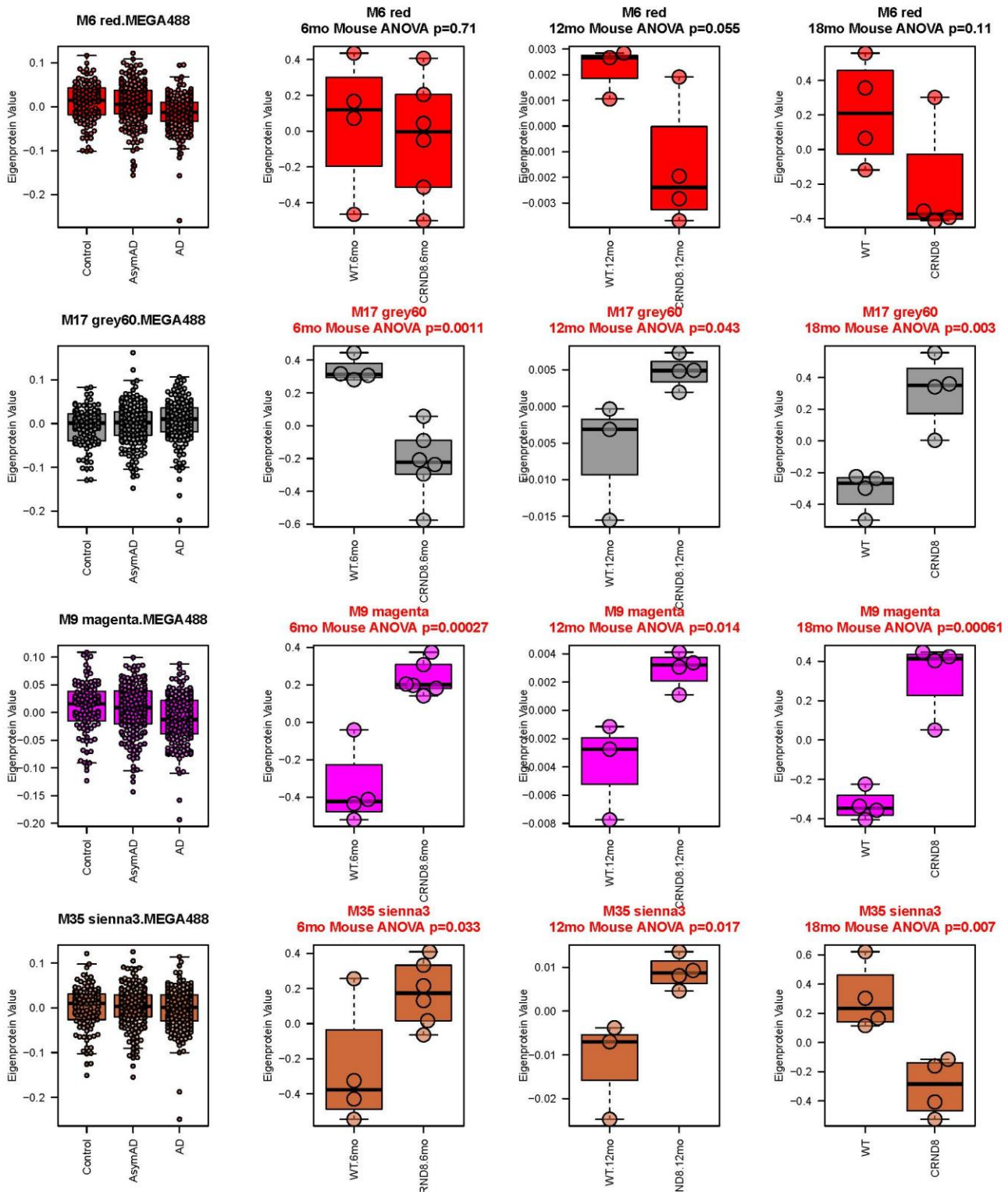

Figure S3. Synthetic eigenproteins (modules) show trends across the three cohorts of aged Tg and non-Tg mice for all 44 consensus brain modules.

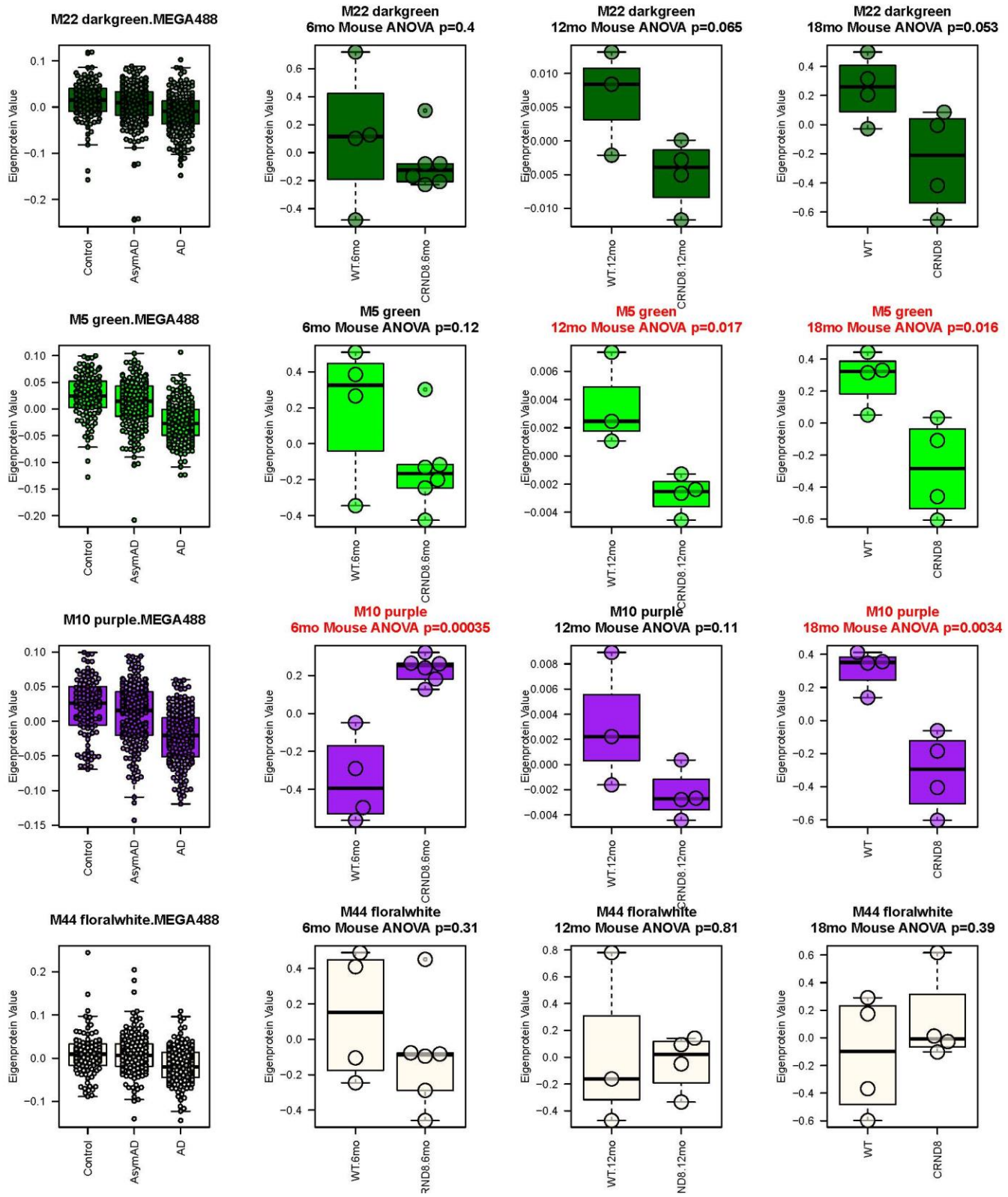

Figure S3 (cont.). Synthetic eigenproteins (modules) show trends across the three cohorts of aged Tg and non-Tg mice for all 44 consensus brain modules.

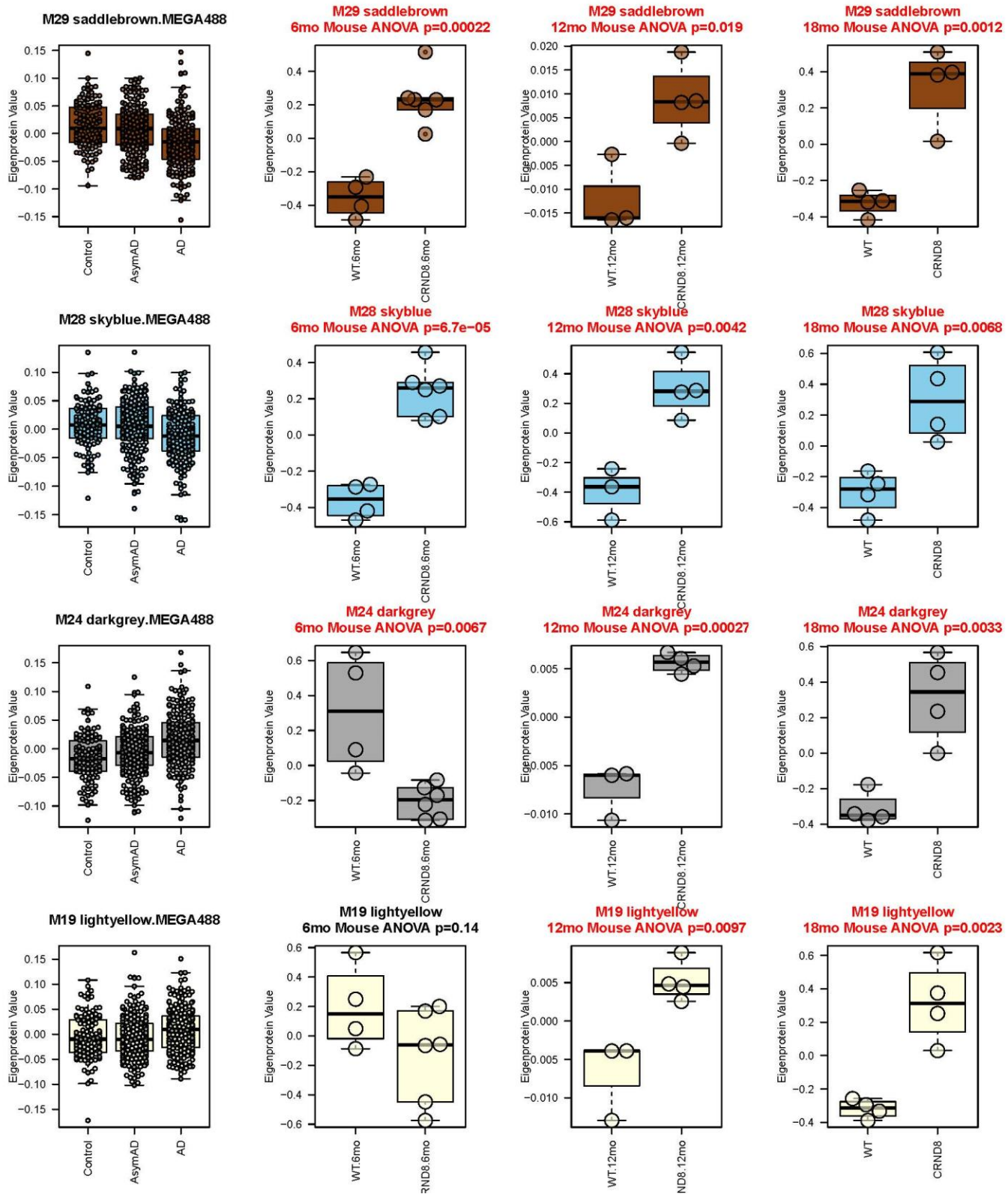

Figure S3 (cont.). Synthetic eigenproteins (modules) show trends across the three cohorts of aged Tg and non-Tg mice for all 44 consensus brain modules.

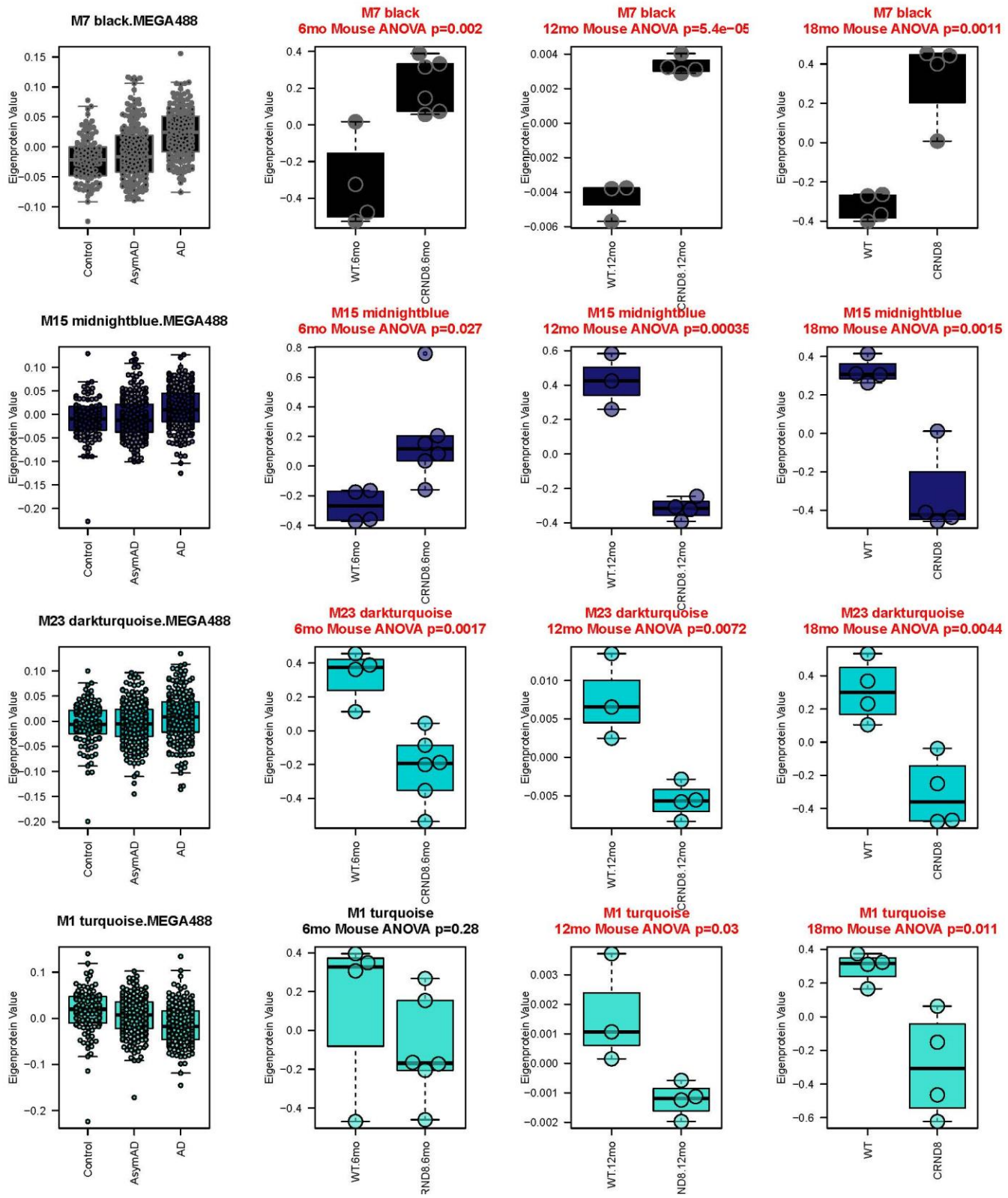

Figure S3 (cont.). Synthetic eigenproteins (modules) show trends across the three cohorts of aged Tg and non-Tg mice for all 44 consensus brain modules.

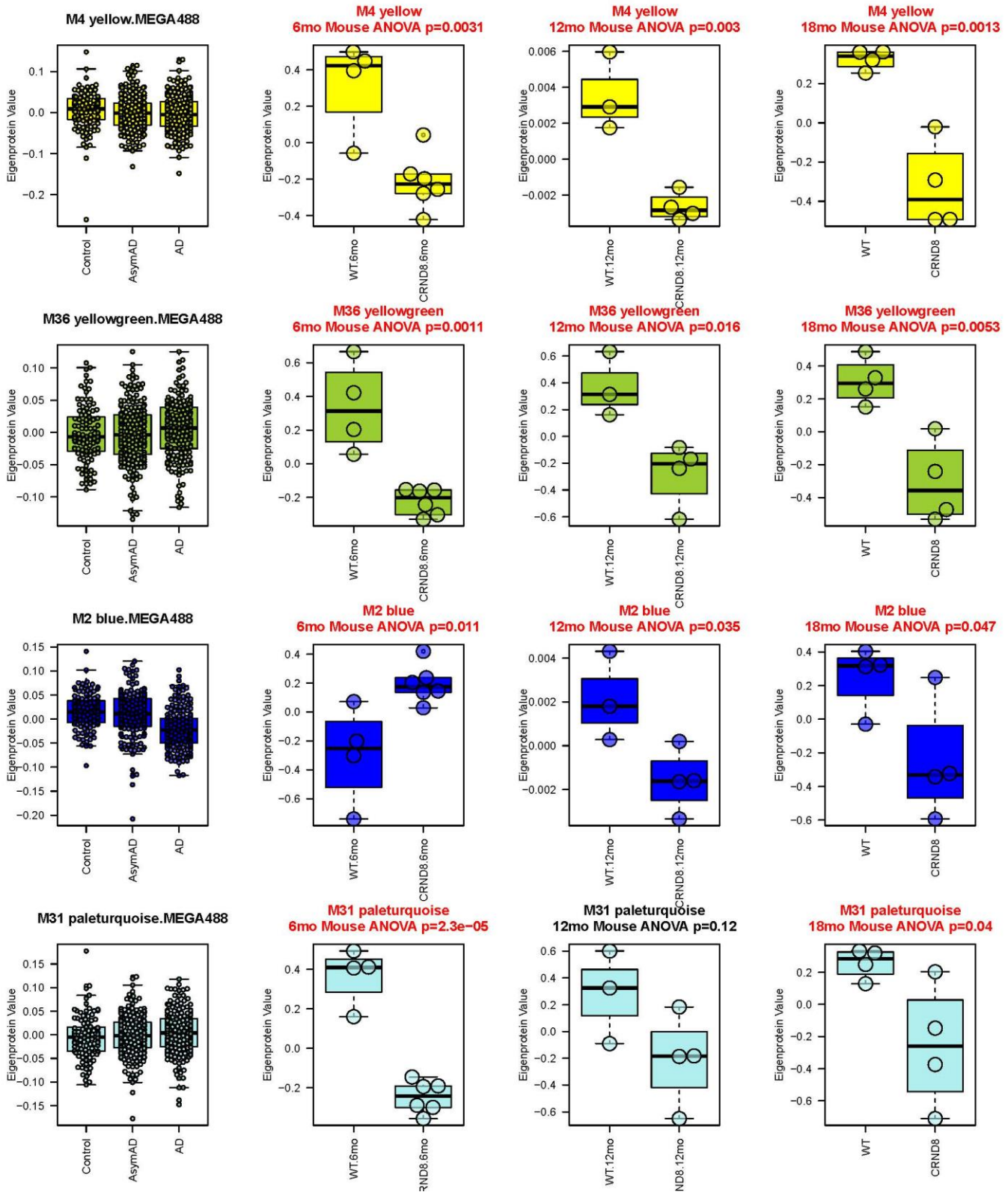

Figure S3 (cont.). Synthetic eigenproteins (modules) show trends across the three cohorts of aged Tg and non-Tg mice for all 44 consensus brain modules.

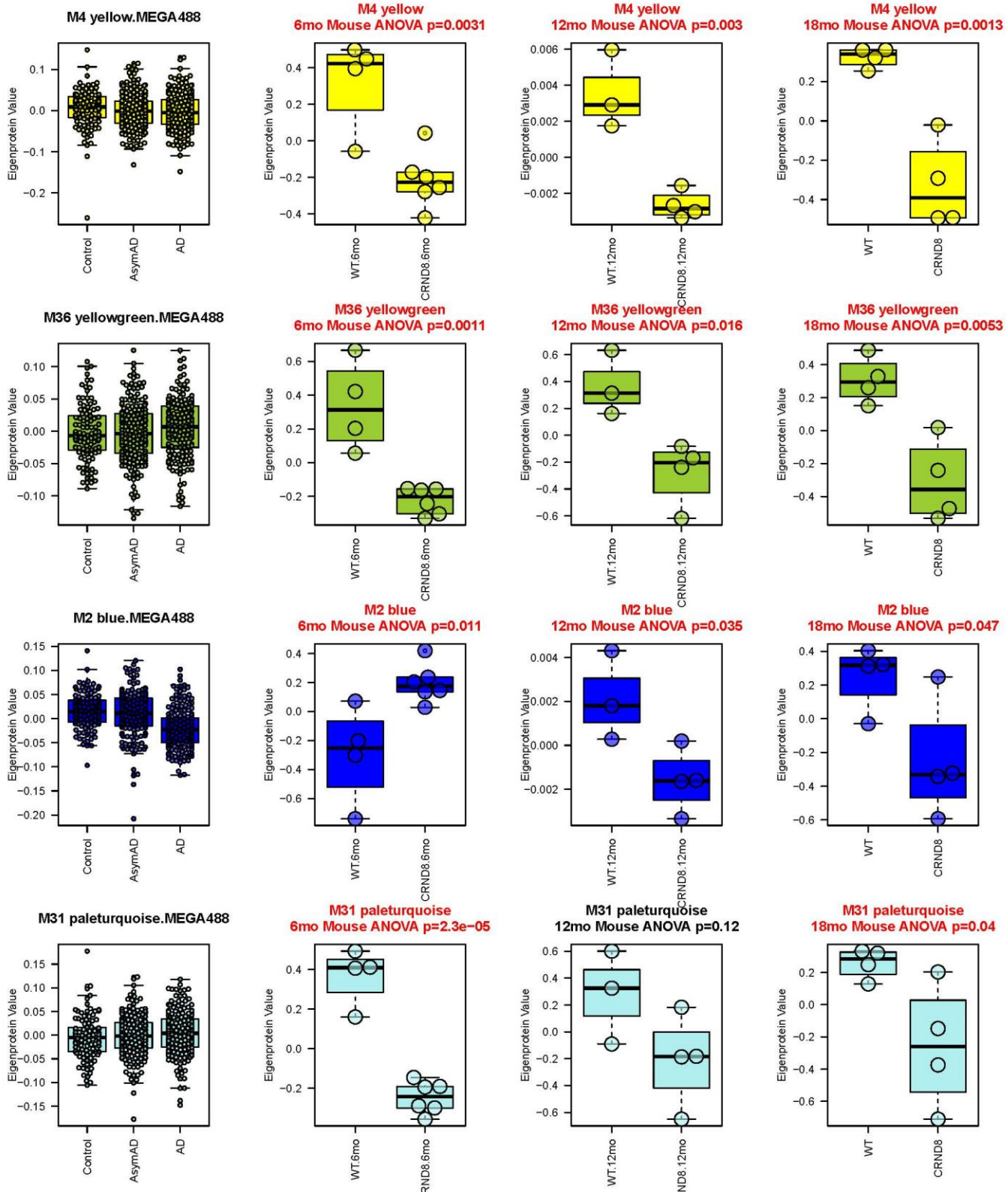

Figure S3 (cont.). Synthetic eigenproteins (modules) show trends across the three cohorts of aged Tg and non-Tg mice for all 44 consensus brain modules.

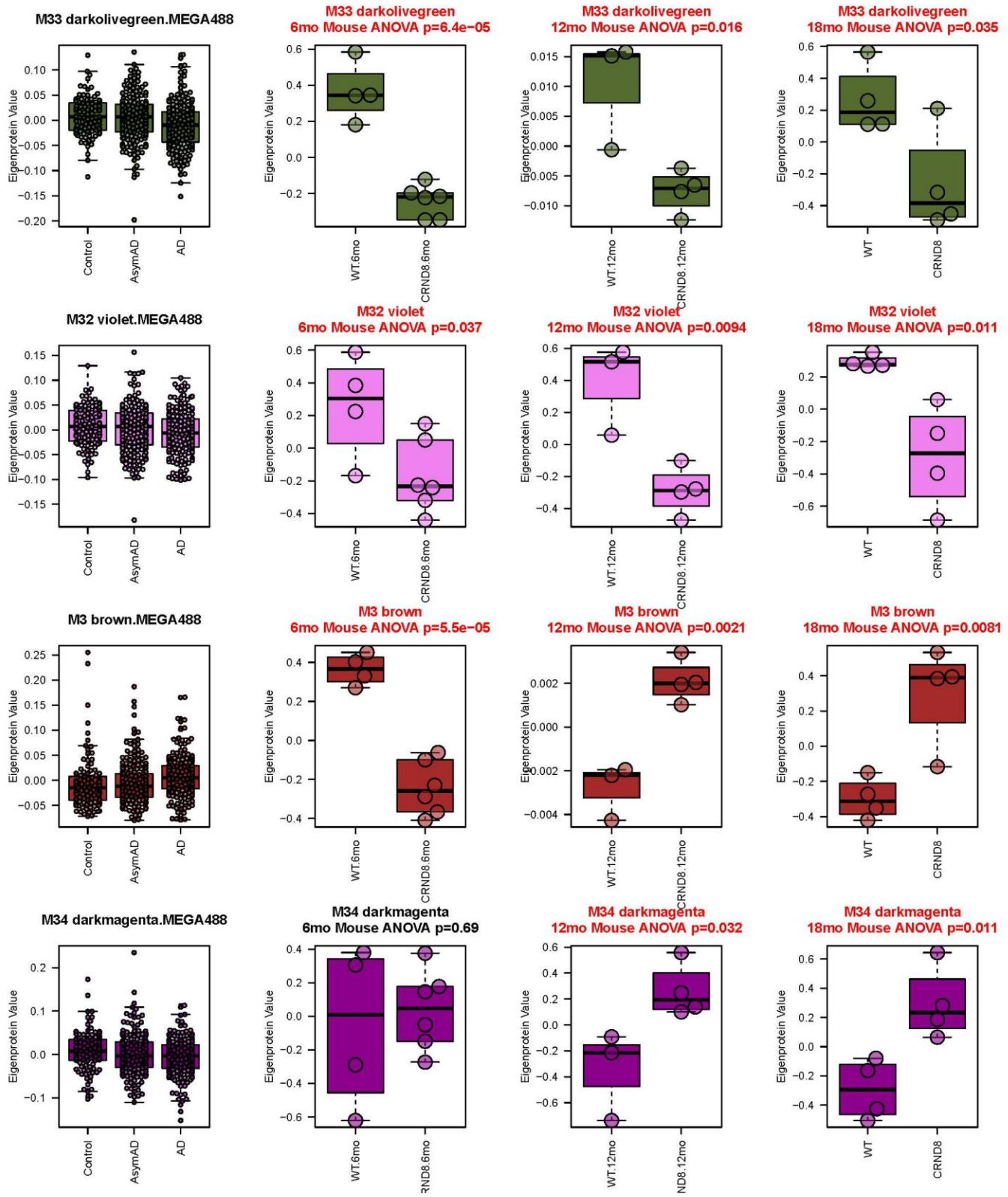

Figure S3 (cont.). Synthetic eigenproteins (modules) show trends across the three cohorts of aged Tg and non-Tg mice for all 44 consensus brain modules.

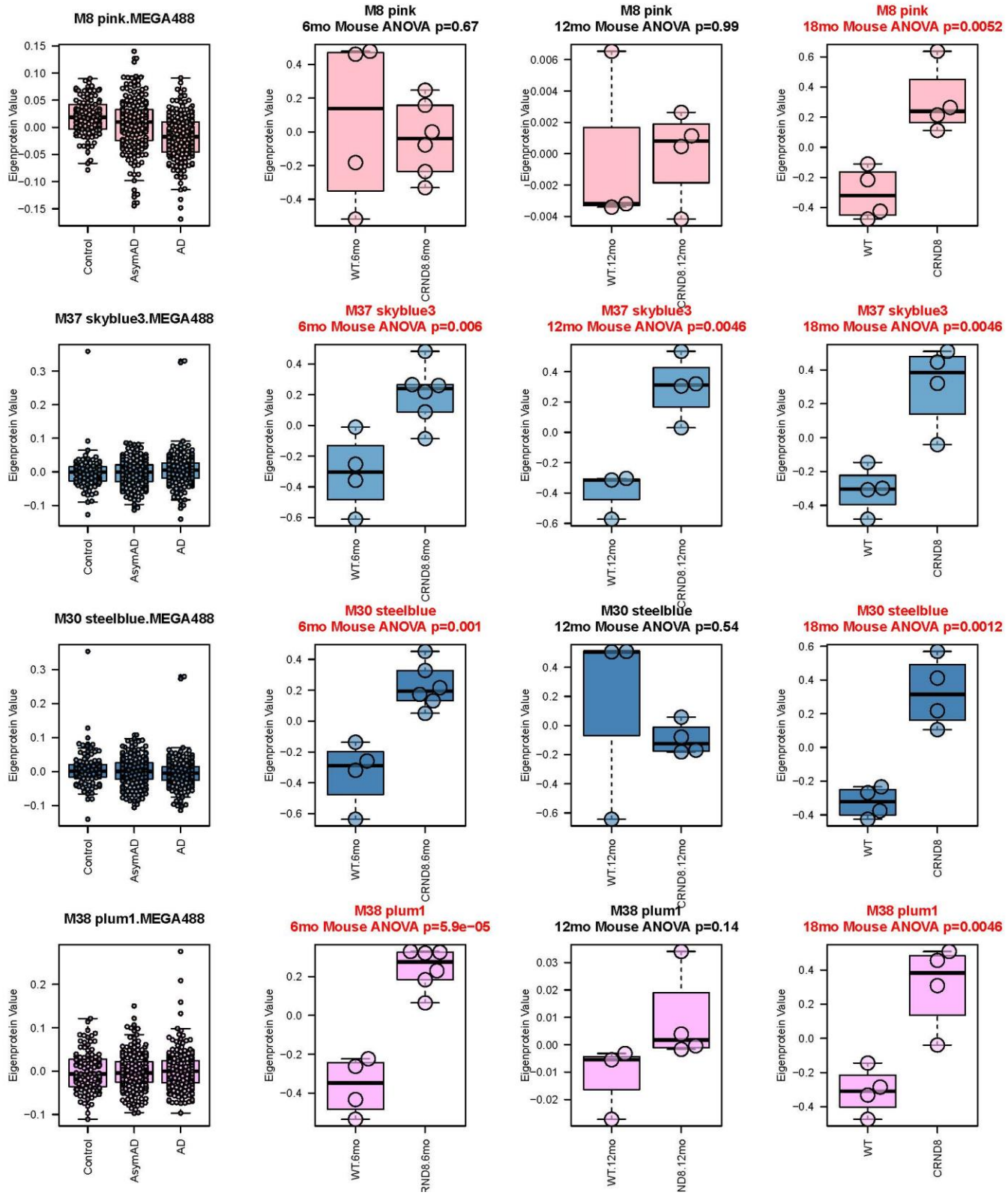

Figure S3 (cont.). Synthetic eigenproteins (modules) show trends across the three cohorts of aged Tg and non-Tg mice for all 44 consensus brain modules.

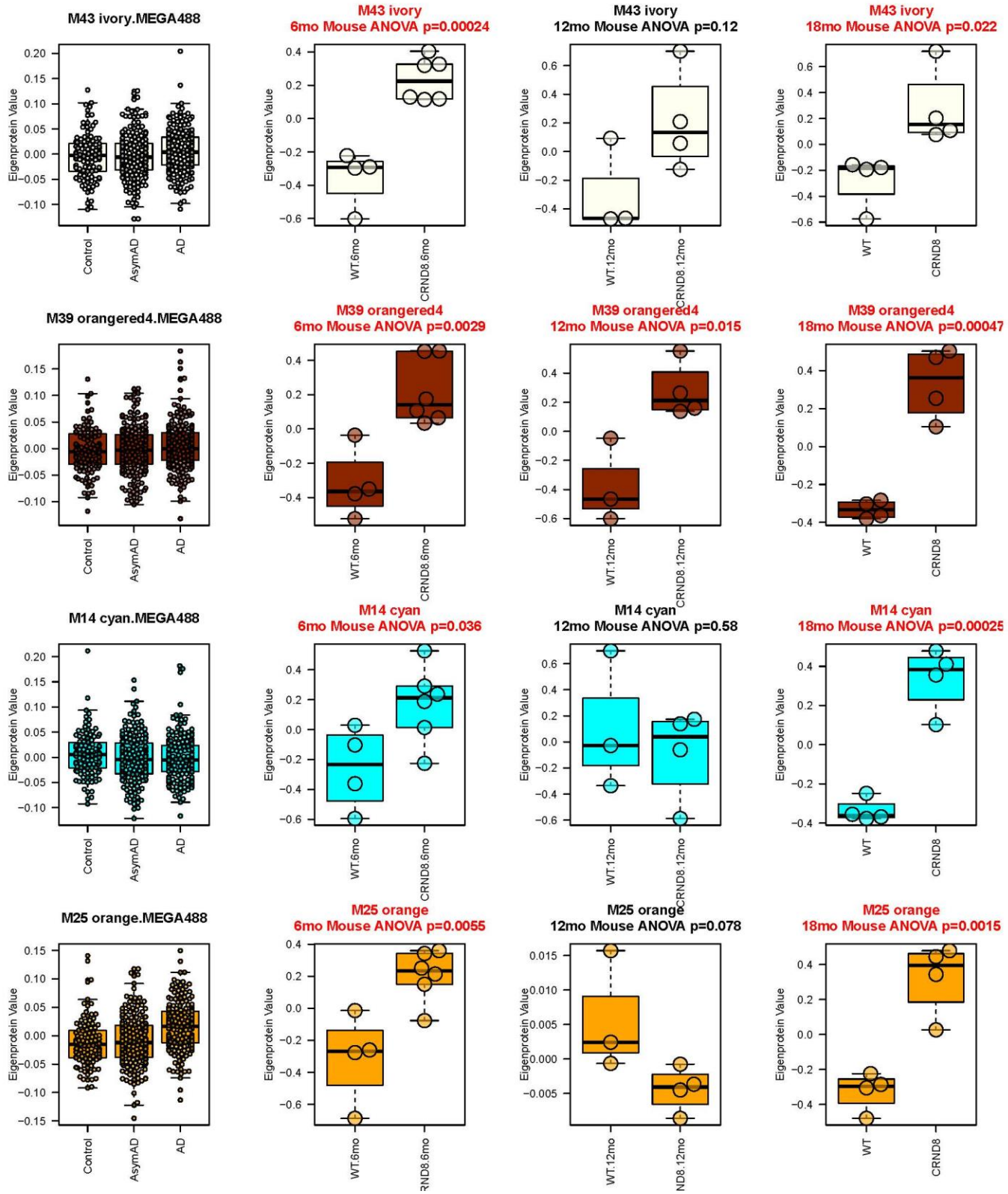

Figure S3 (cont.). Synthetic eigenproteins (modules) show trends across the three cohorts of aged Tg and non-Tg mice for all 44 consensus brain modules.

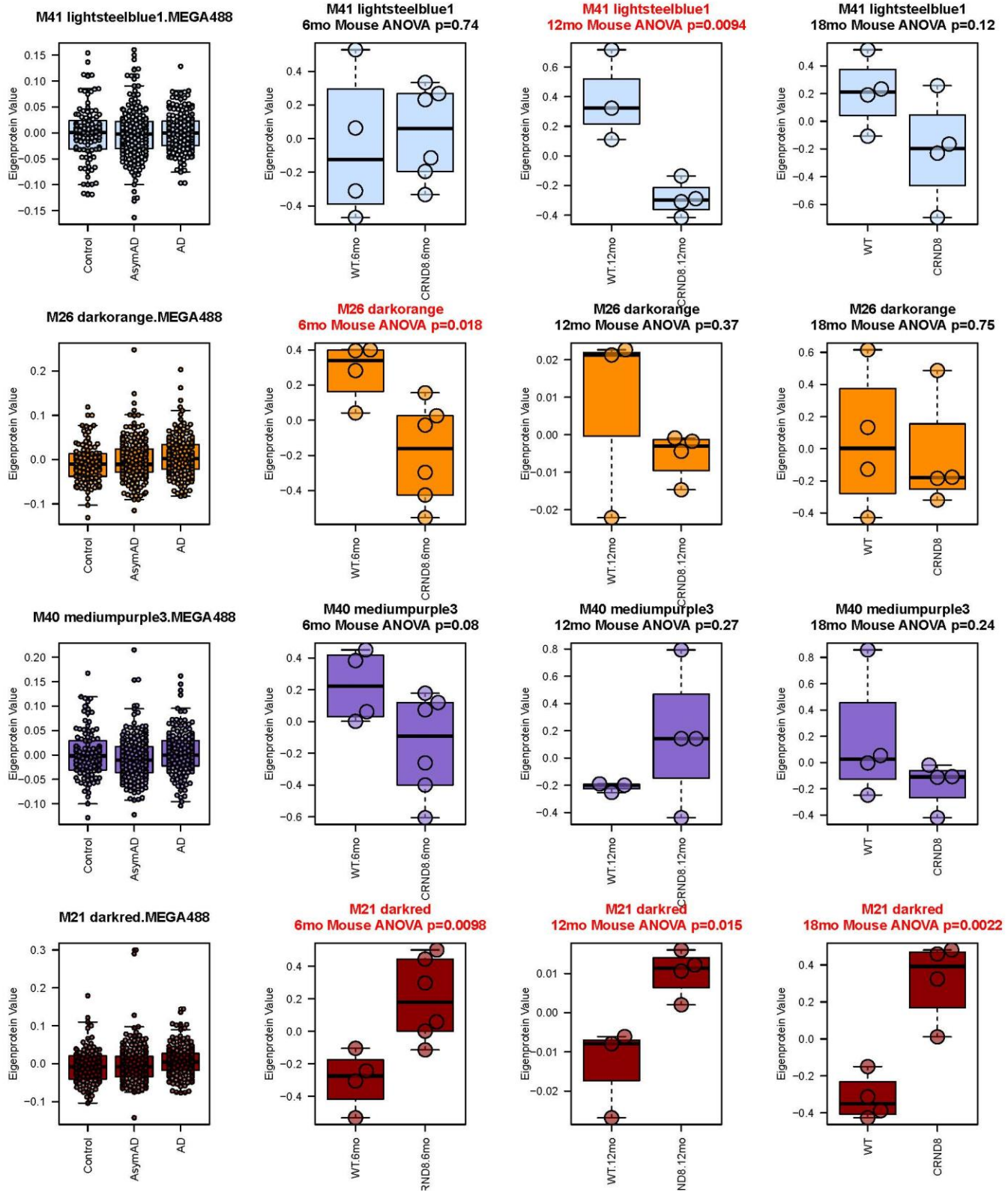

Figure S3 (cont.). Synthetic eigenproteins (modules) show trends across the three cohorts of aged Tg and non-Tg mice for all 44 consensus brain modules.

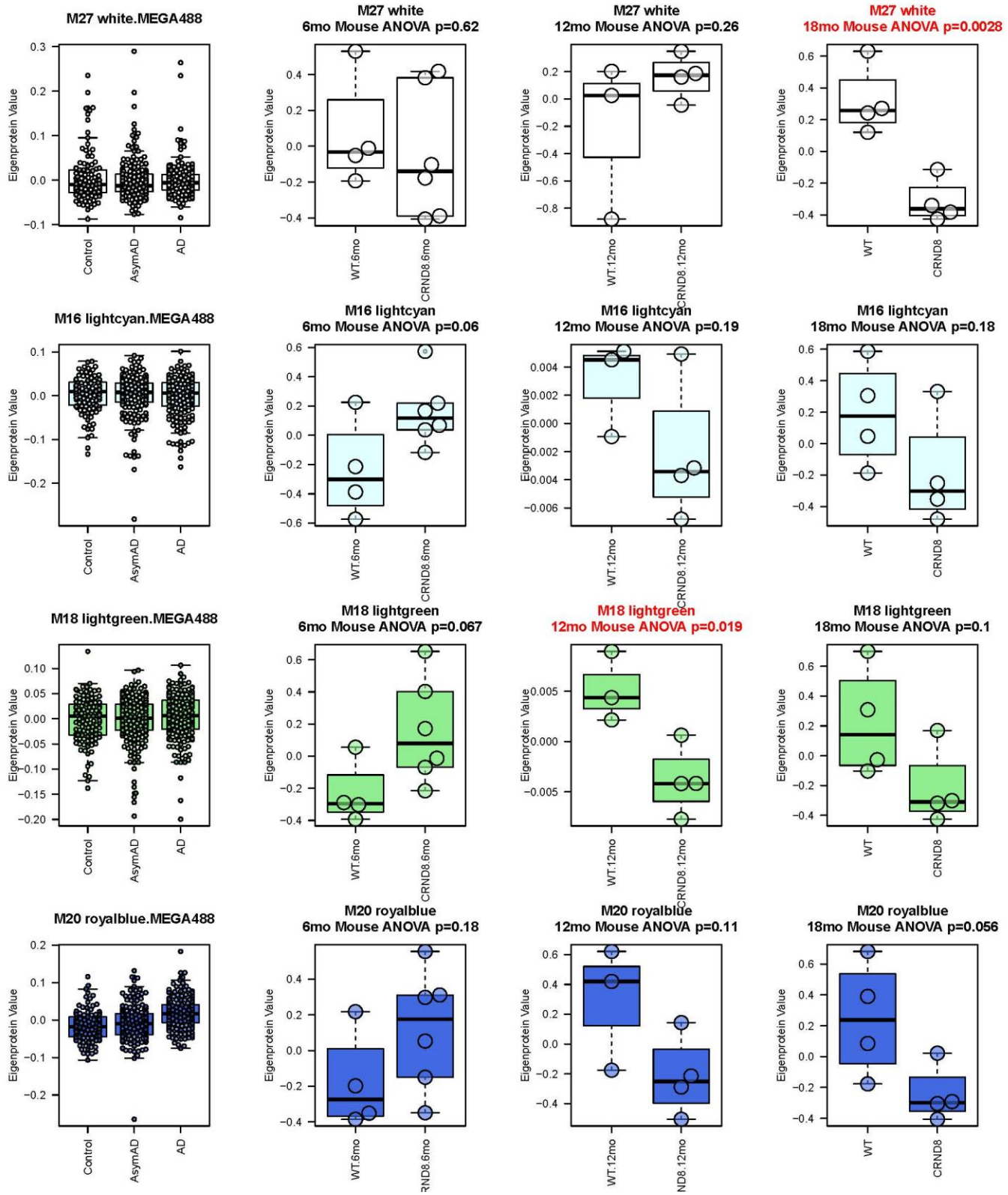

Figure S3 (cont.). Synthetic eigenproteins (modules) show trends across the three cohorts of aged Tg and non-Tg mice for all 44 consensus brain modules.

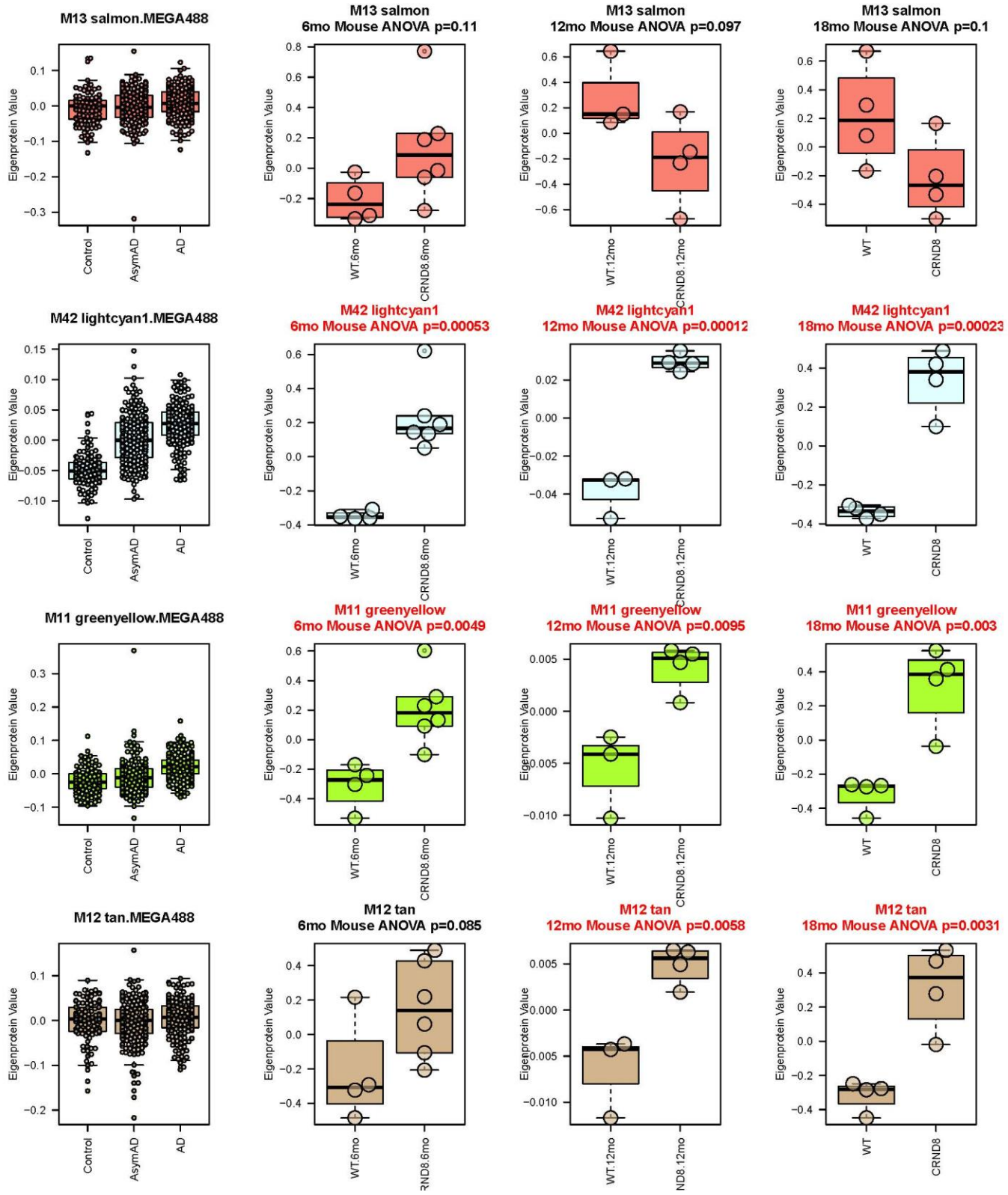

Figure S3 (cont.). Synthetic eigenproteins (modules) show trends across the three cohorts of aged Tg and non-Tg mice for all 44 consensus brain modules.

Figure 4

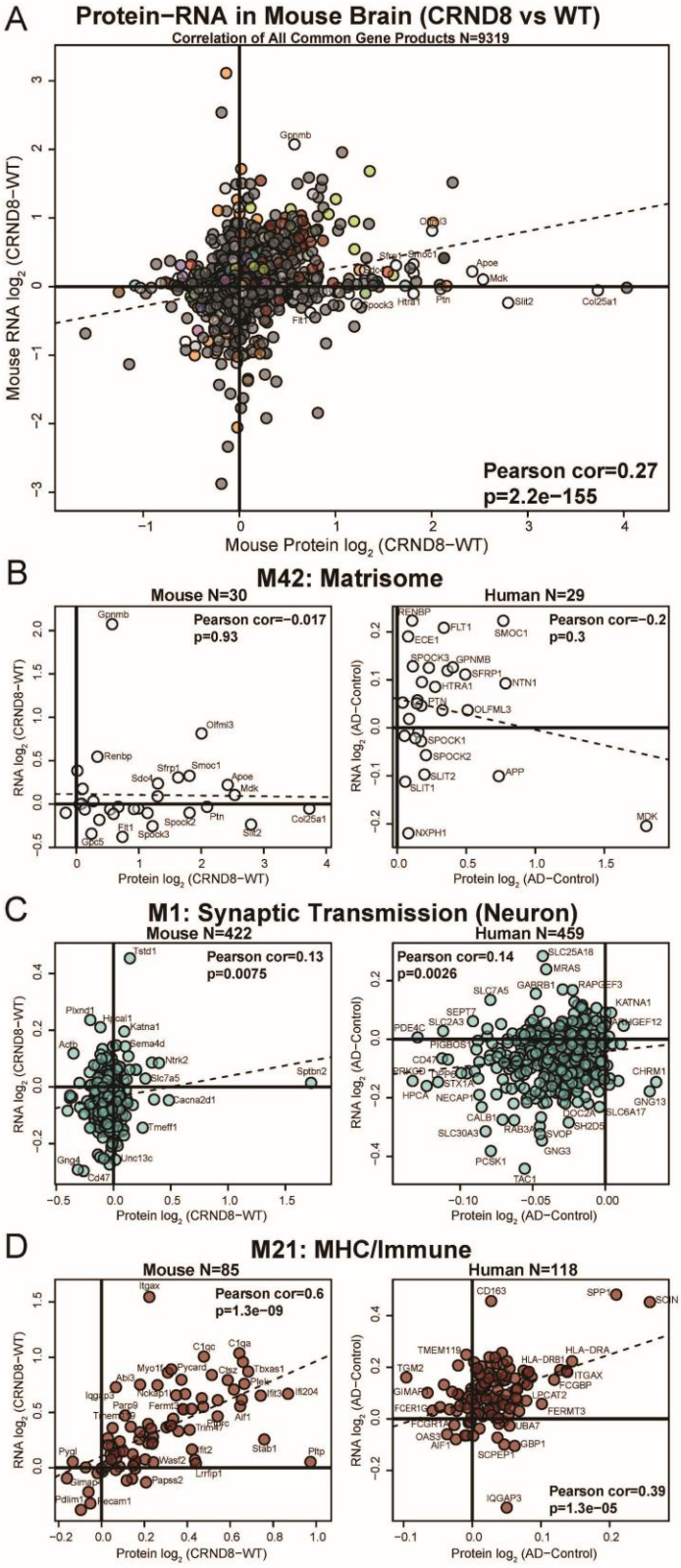

Figure S4. RNA-Protein AD or Tg Effect Size Correlation, in total and within modules.

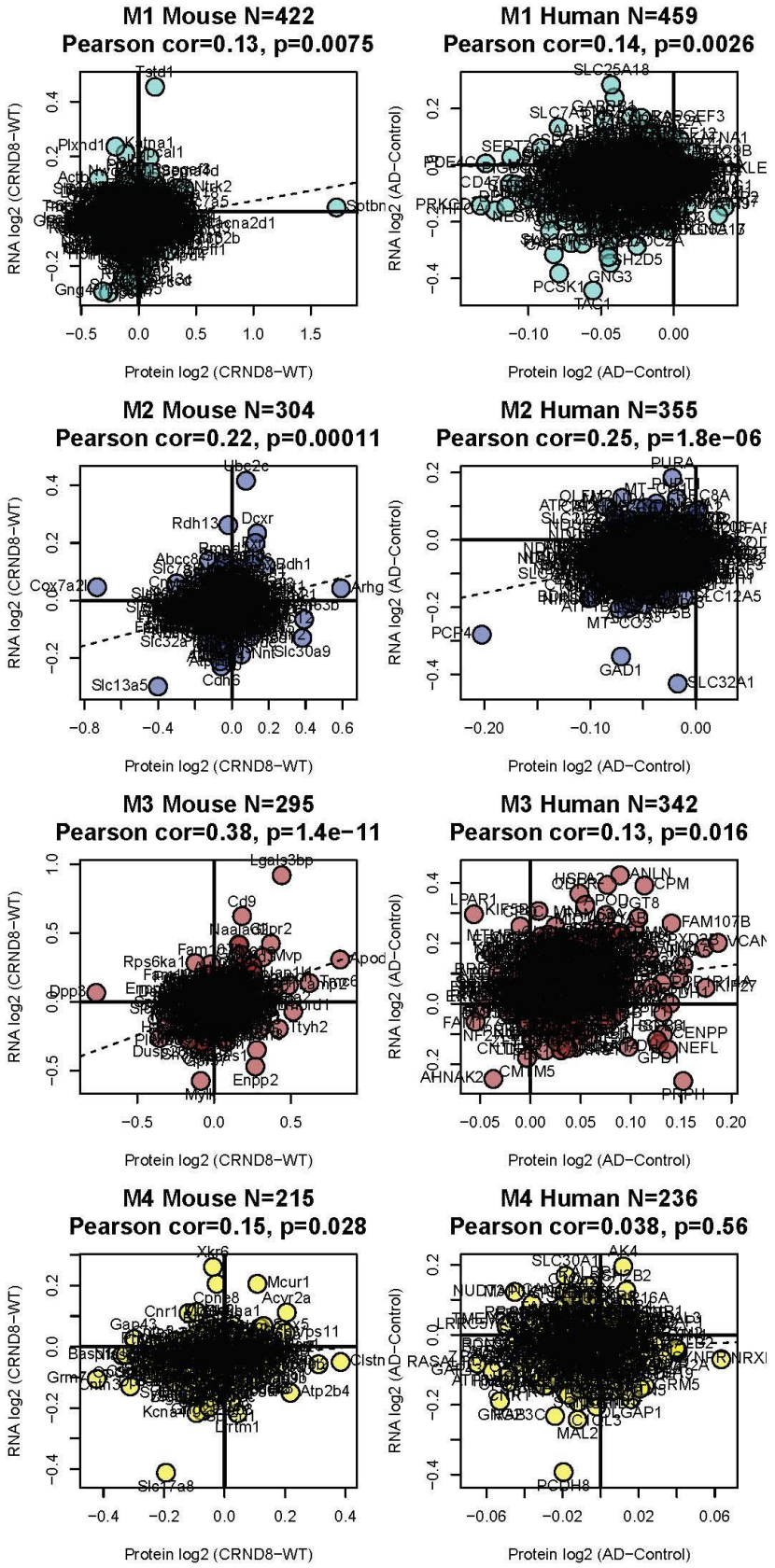

Figure S5. Protein-RNA effect size correlation varies in mouse and human for all 44 consensus brain modules.

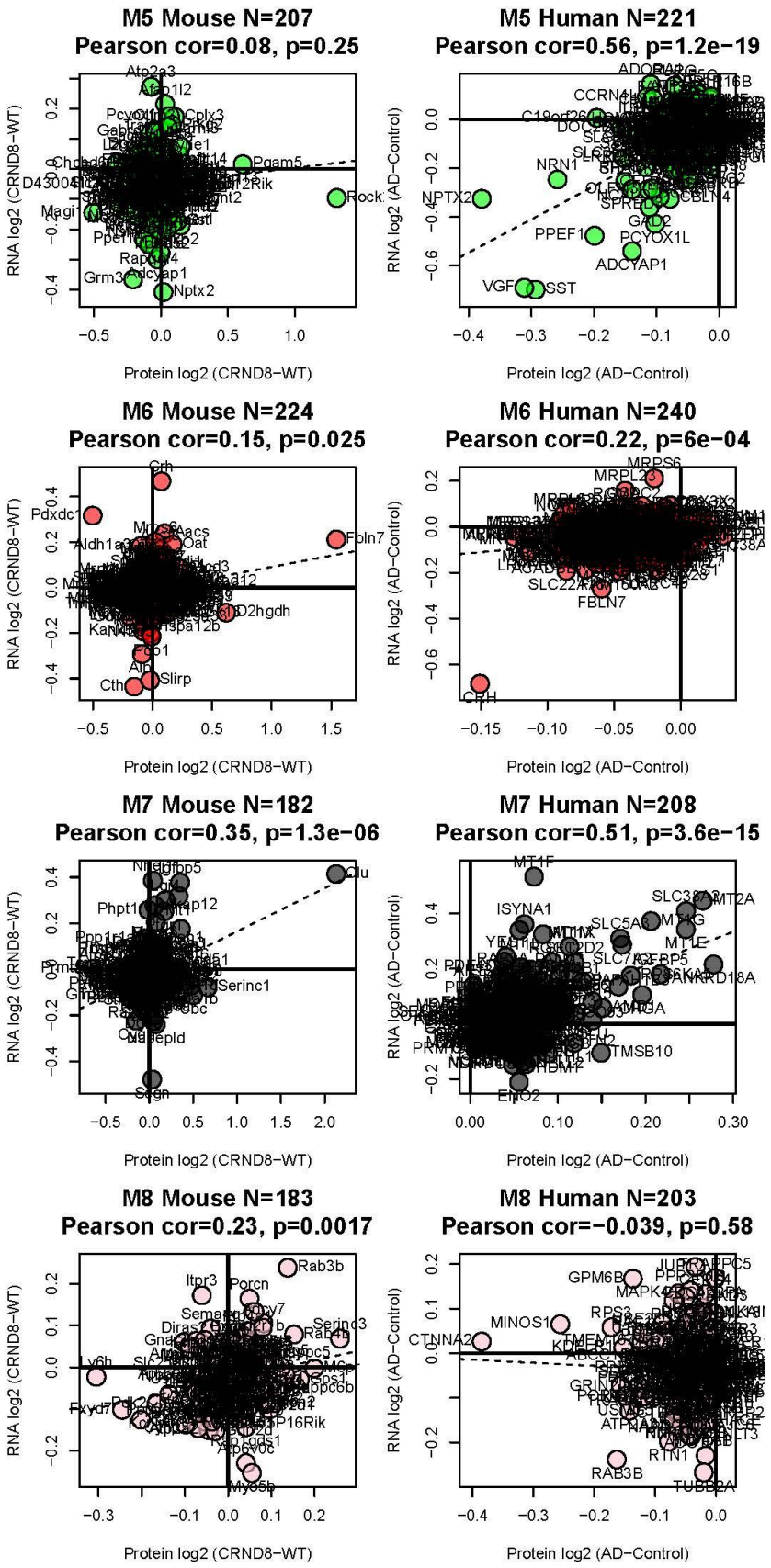

Figure S5 (cont.). Protein-RNA effect size correlation varies in mouse and human for all 44 consensus brain modules.

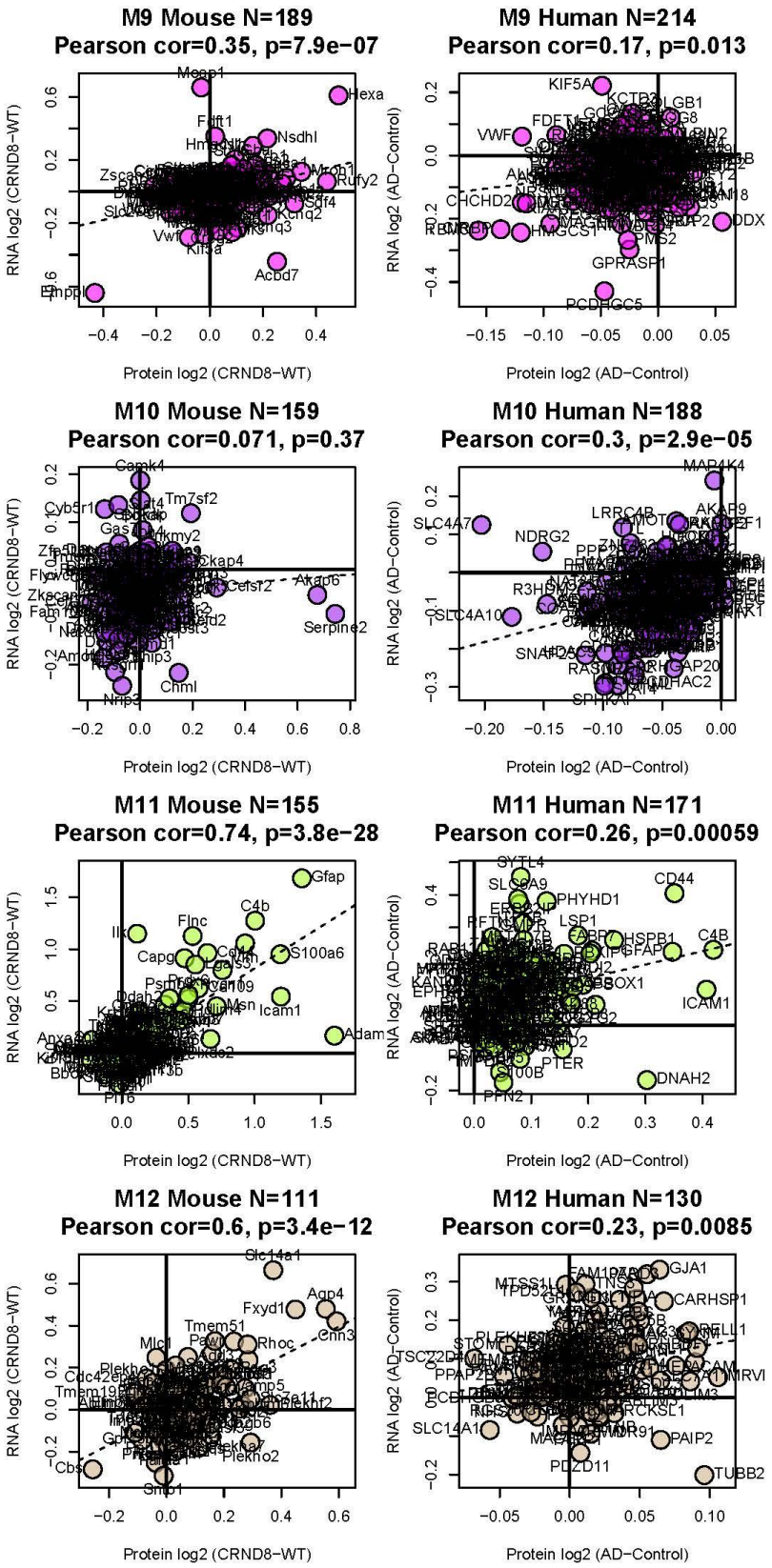

Figure S5 (cont.). Protein-RNA effect size correlation varies in mouse and human for all 44 consensus brain modules.

1680

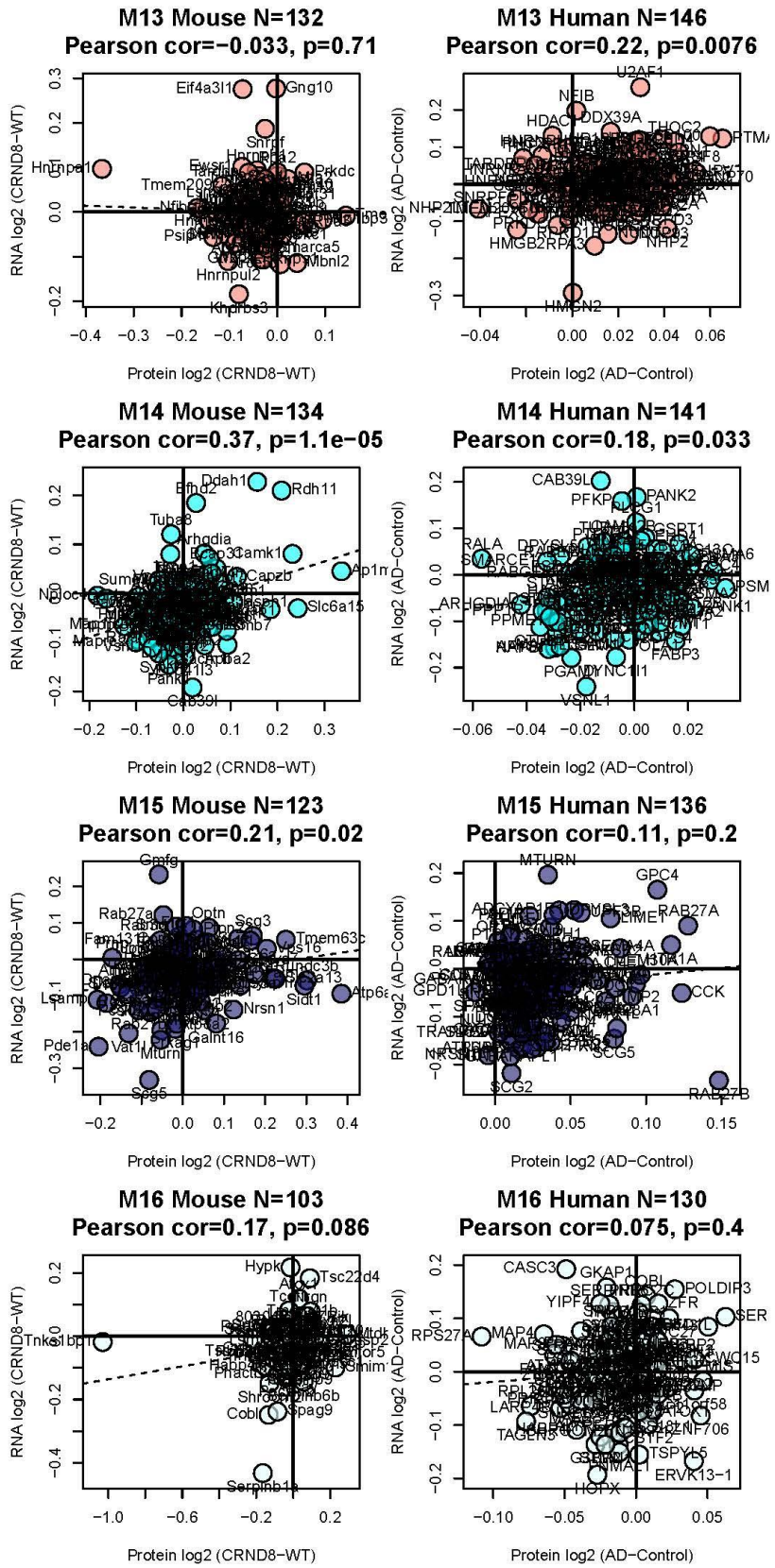

Figure S5 (cont.). Protein-RNA effect size correlation varies in mouse and human for all 44 consensus brain modules.

1681

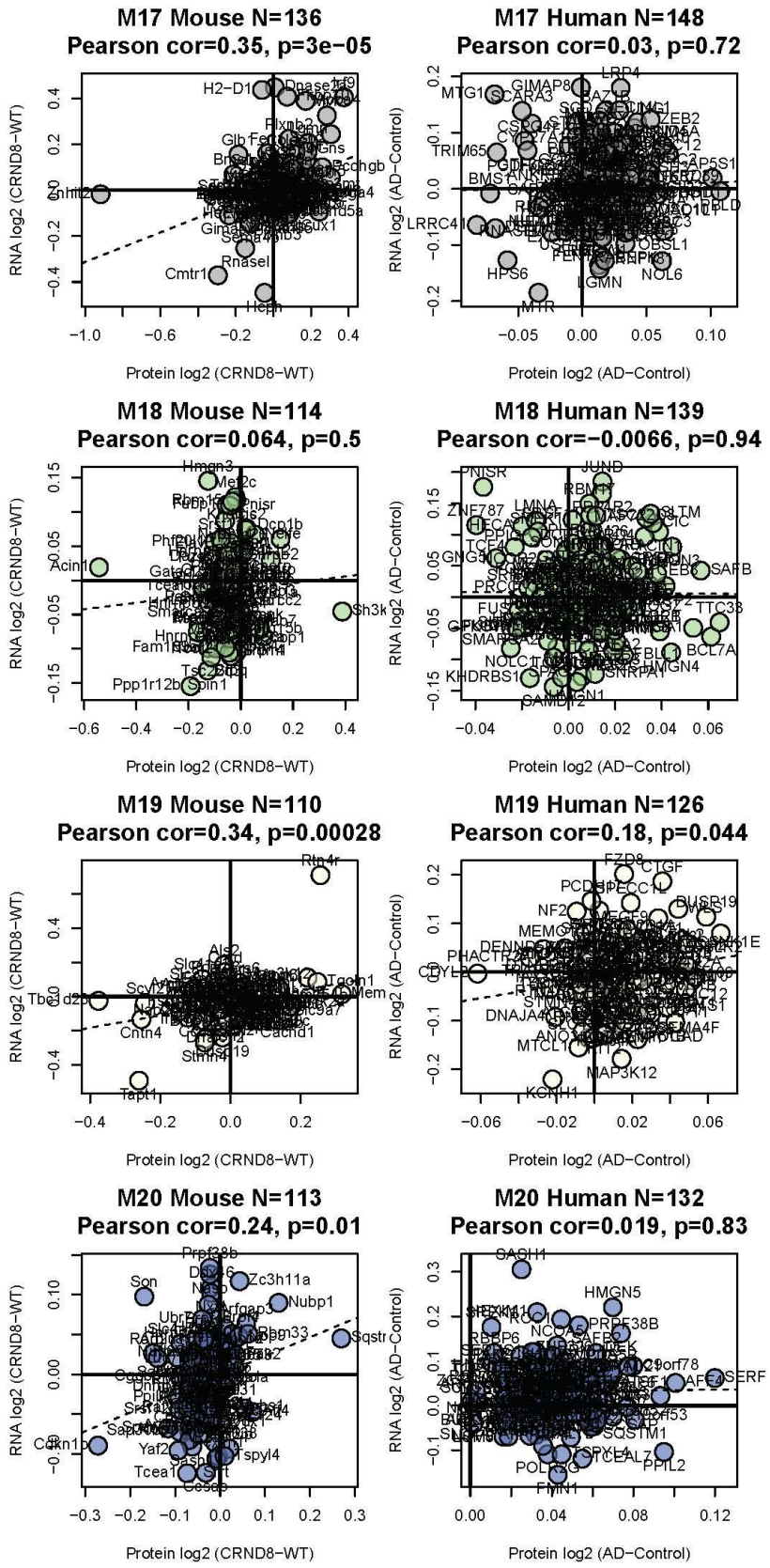

Figure S5 (cont.). Protein-RNA effect size correlation varies in mouse and human for all 44 consensus brain modules.

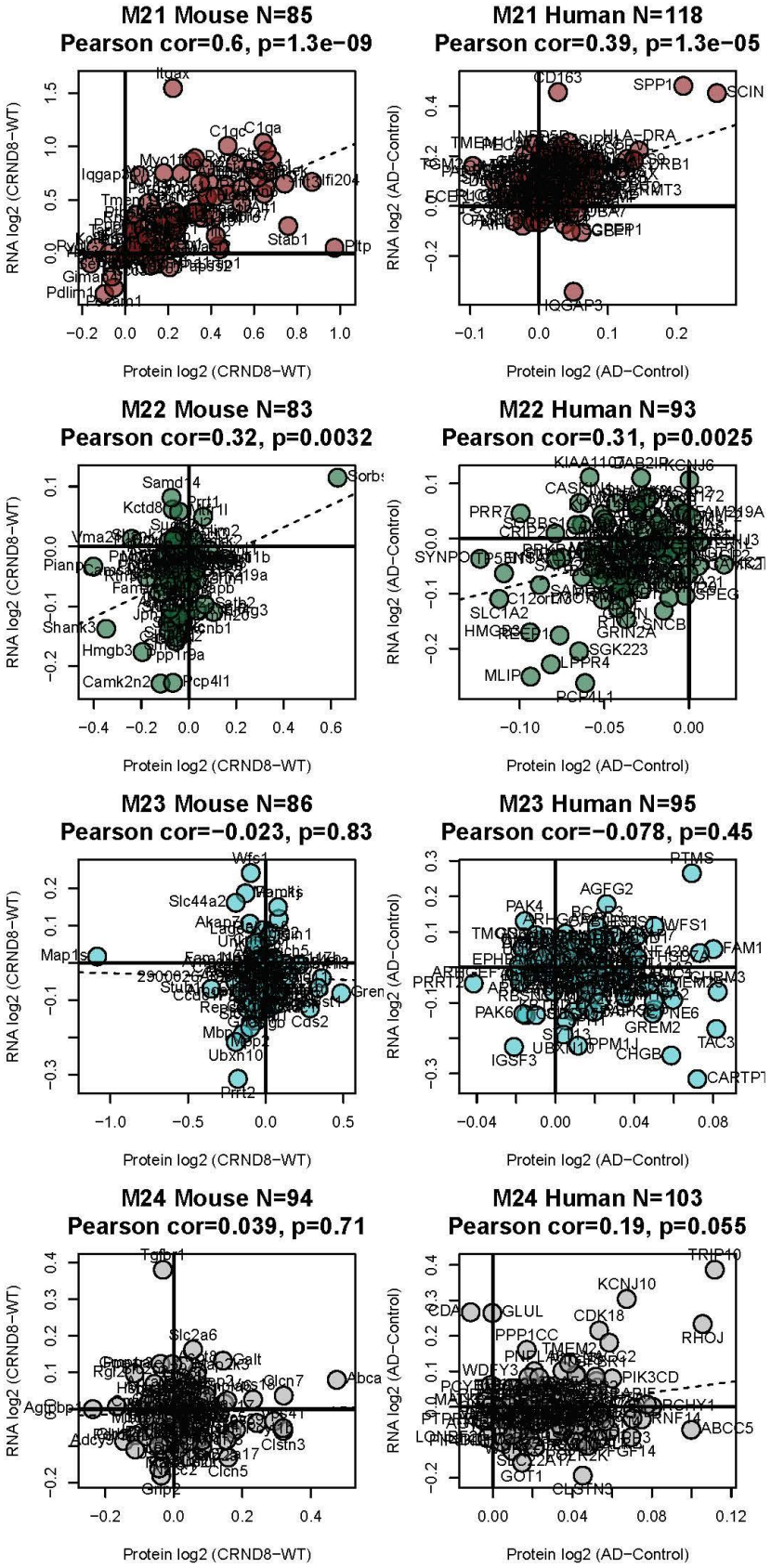

Figure S5 (cont.). Protein-RNA effect size correlation varies in mouse and human for all 44 consensus brain modules.

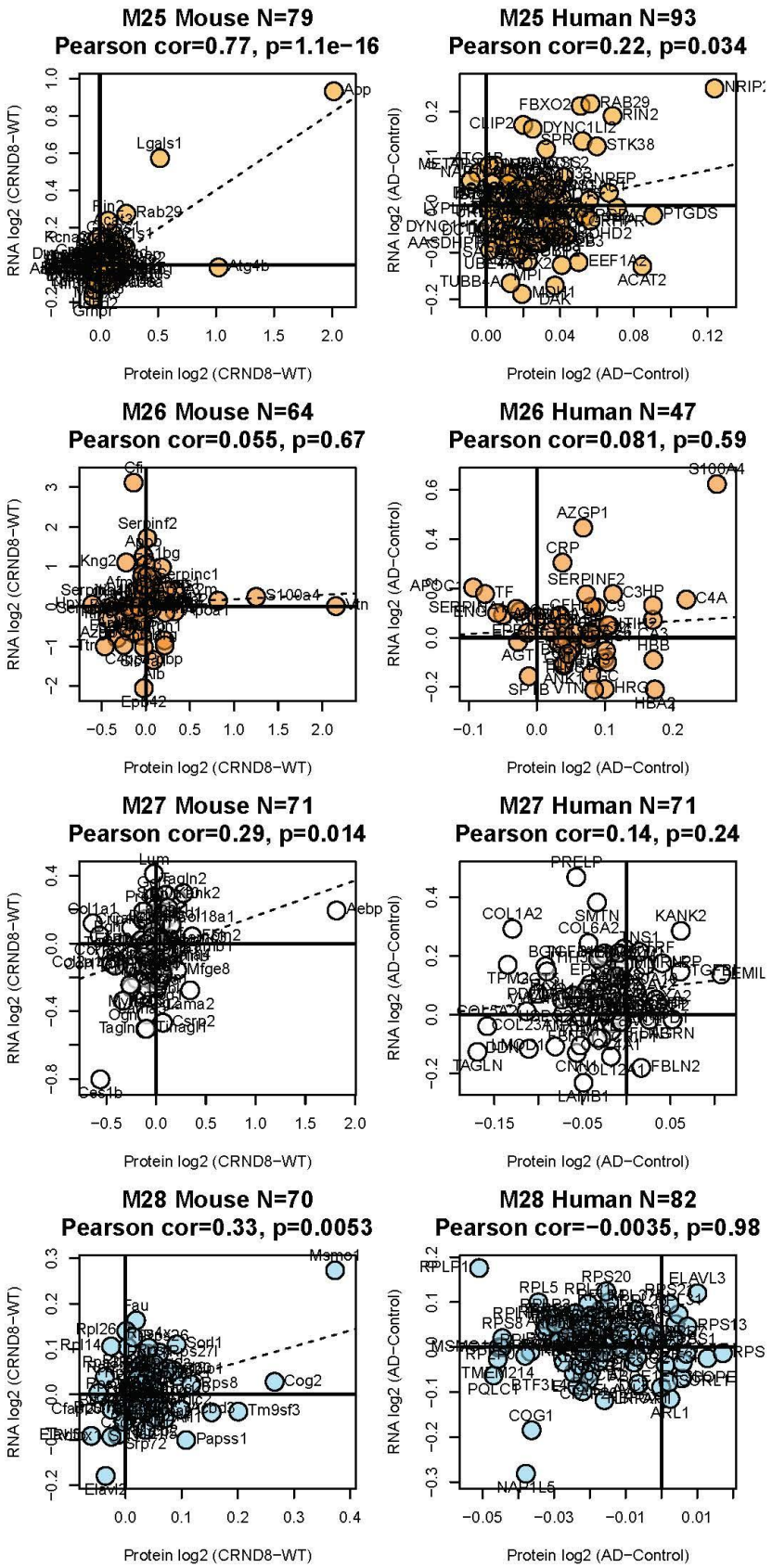

Figure S5 (cont.). Protein-RNA effect size correlation varies in mouse and human for all 44 consensus brain modules.

1684

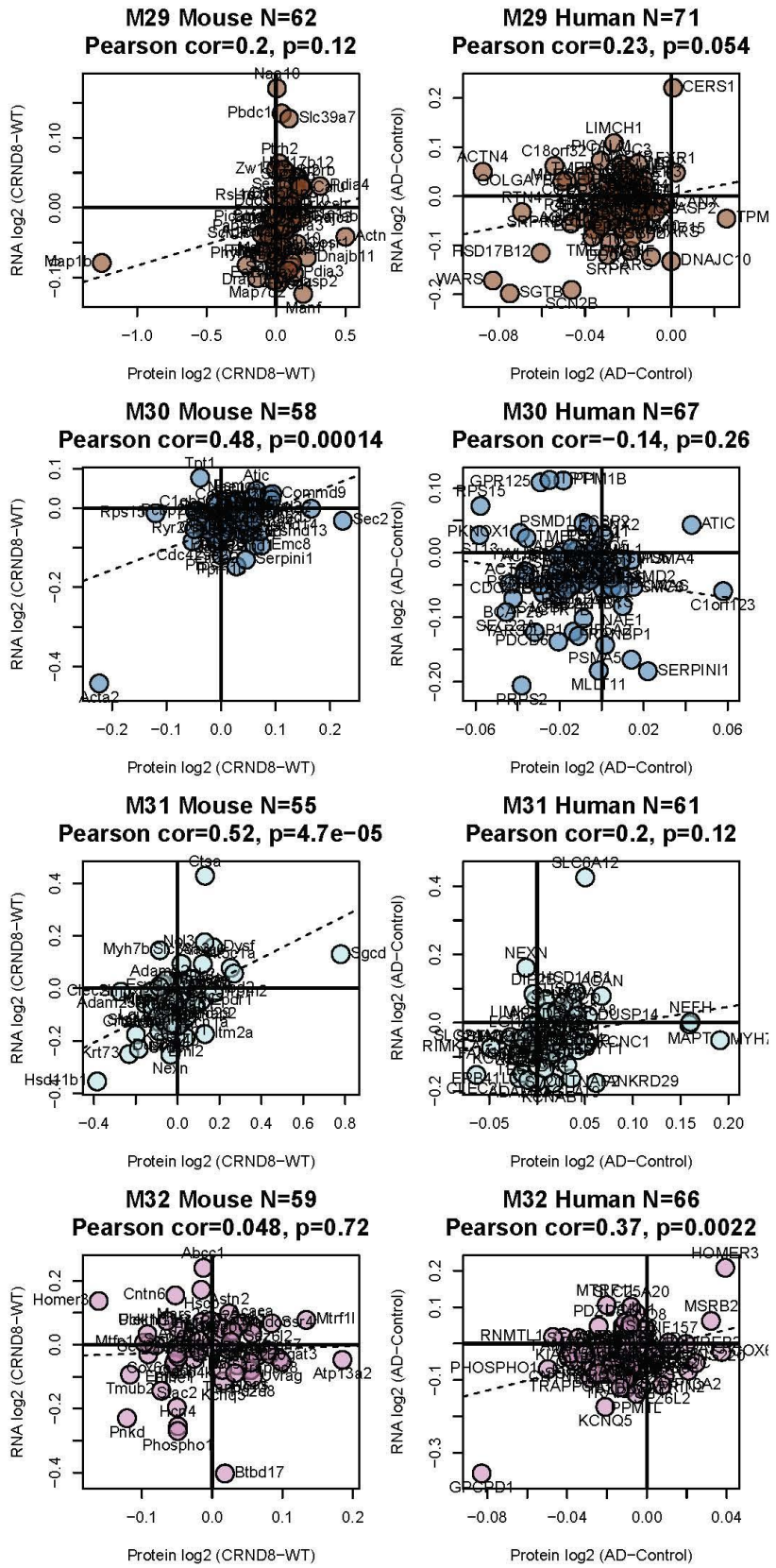

Figure S5 (cont.). Protein-RNA effect size correlation varies in mouse and human for all 44 consensus brain modules.

1685

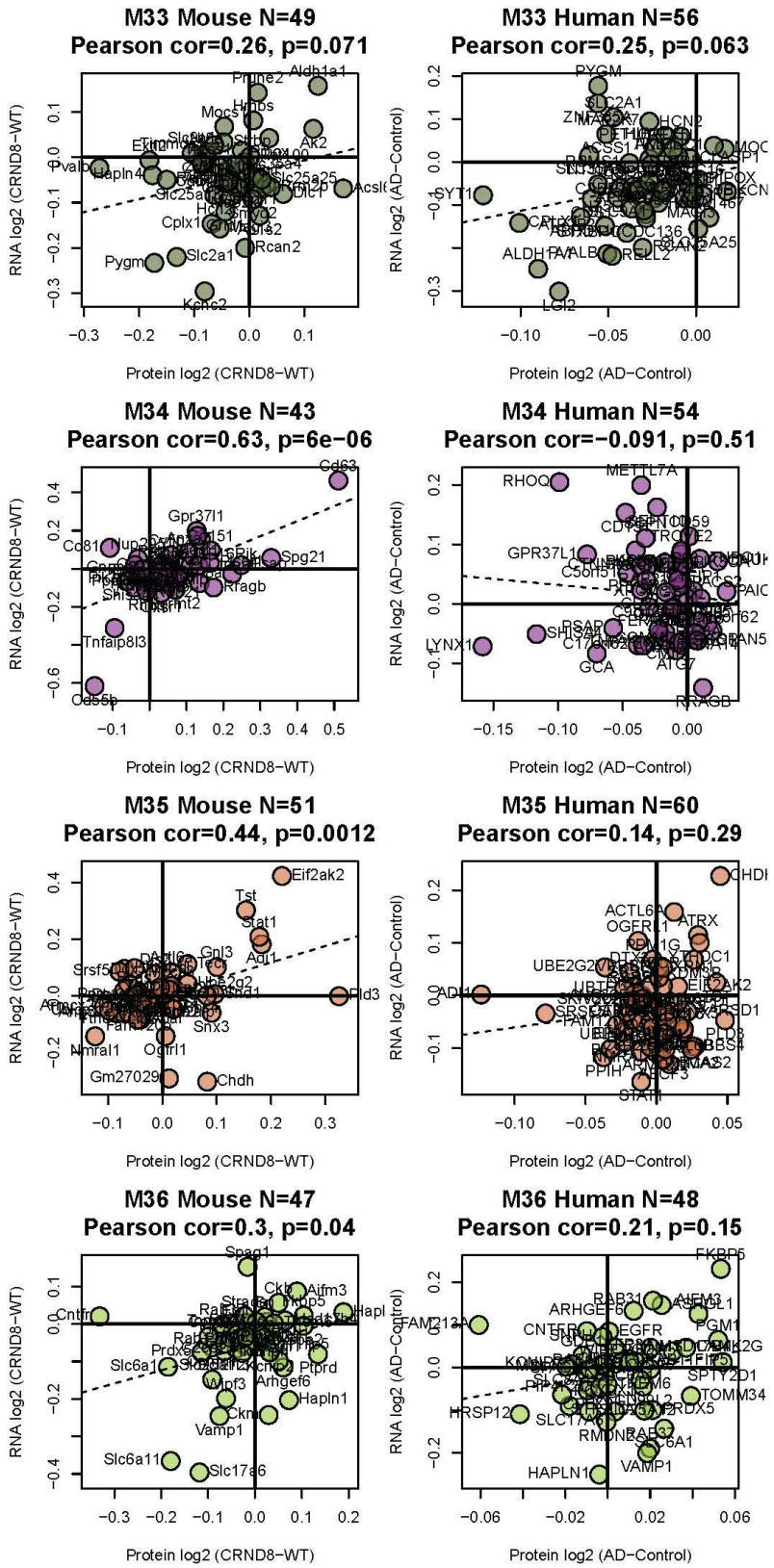

Figure S5 (cont.). Protein-RNA effect size correlation varies in mouse and human for all 44 consensus brain modules.

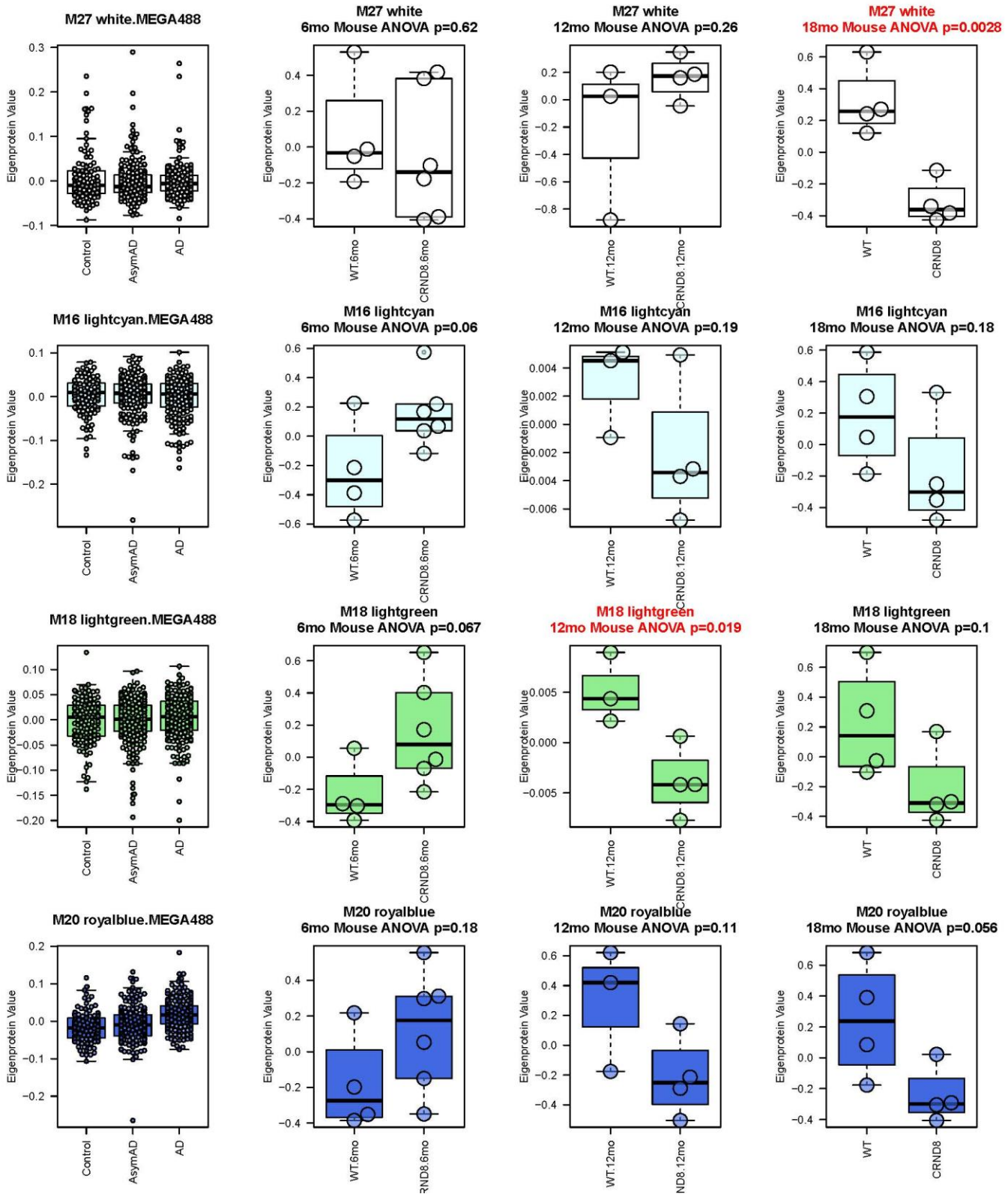

Figure S5 (cont.). Protein-RNA effect size correlation varies in mouse and human for all 44 consensus brain modules.

1687

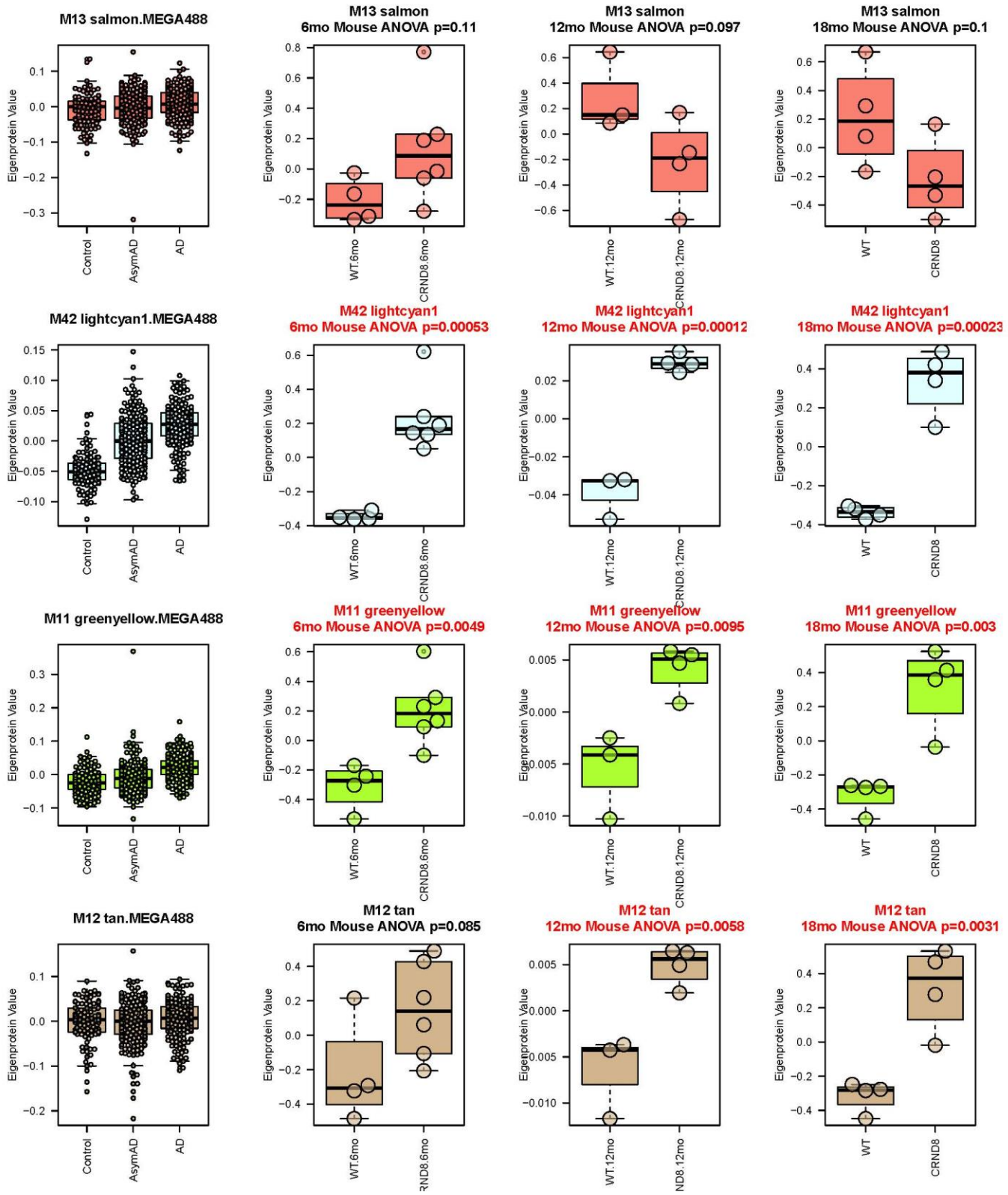

Figure S5 (cont.). Protein-RNA effect size correlation varies in mouse and human for all 44 consensus brain modules.

168

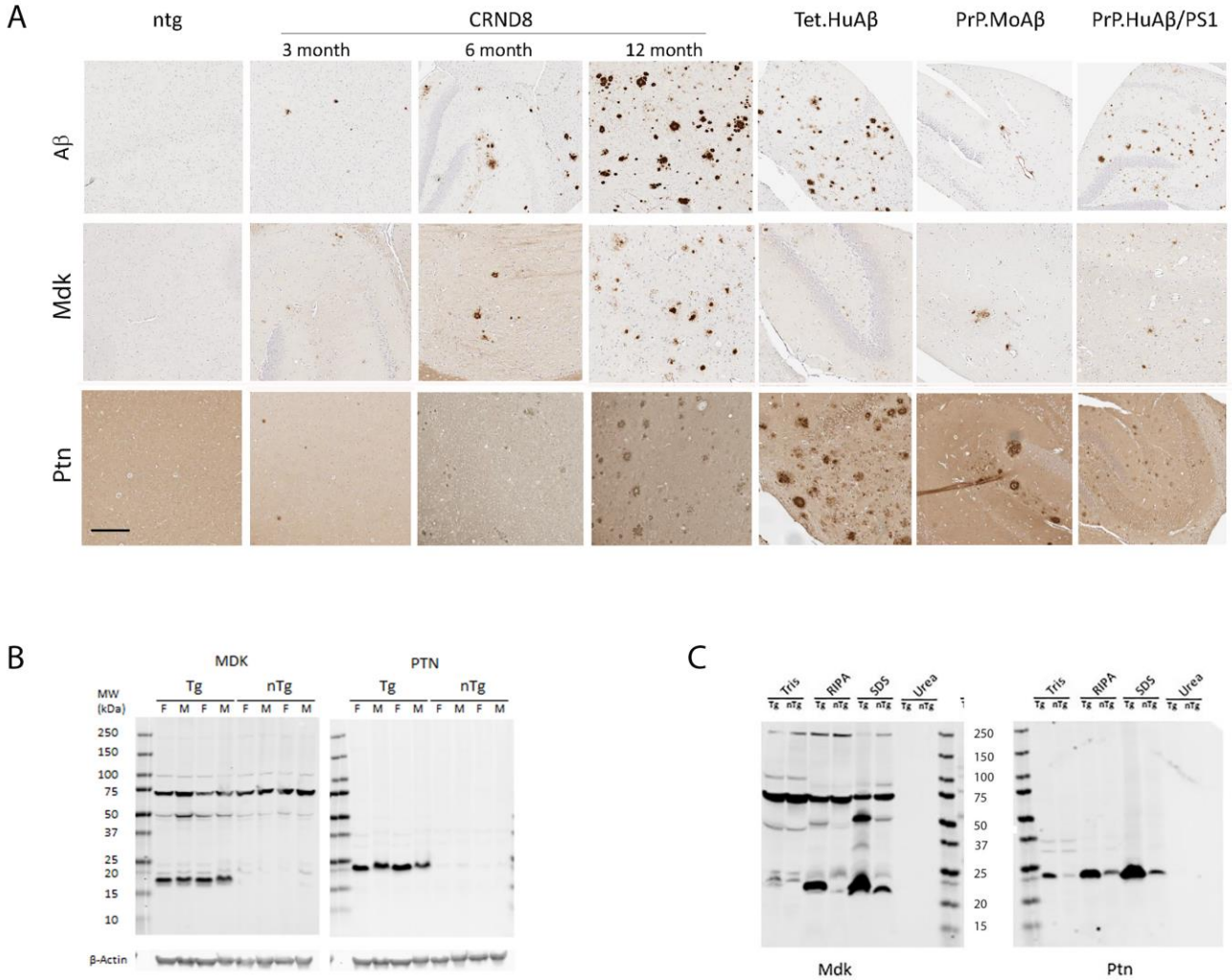

Figure S6. Mdk and Ptn colocalization with amyloid is age dependent, occurs in various AD transgenic mouse models but are enriched in soluble brain fractions.

A

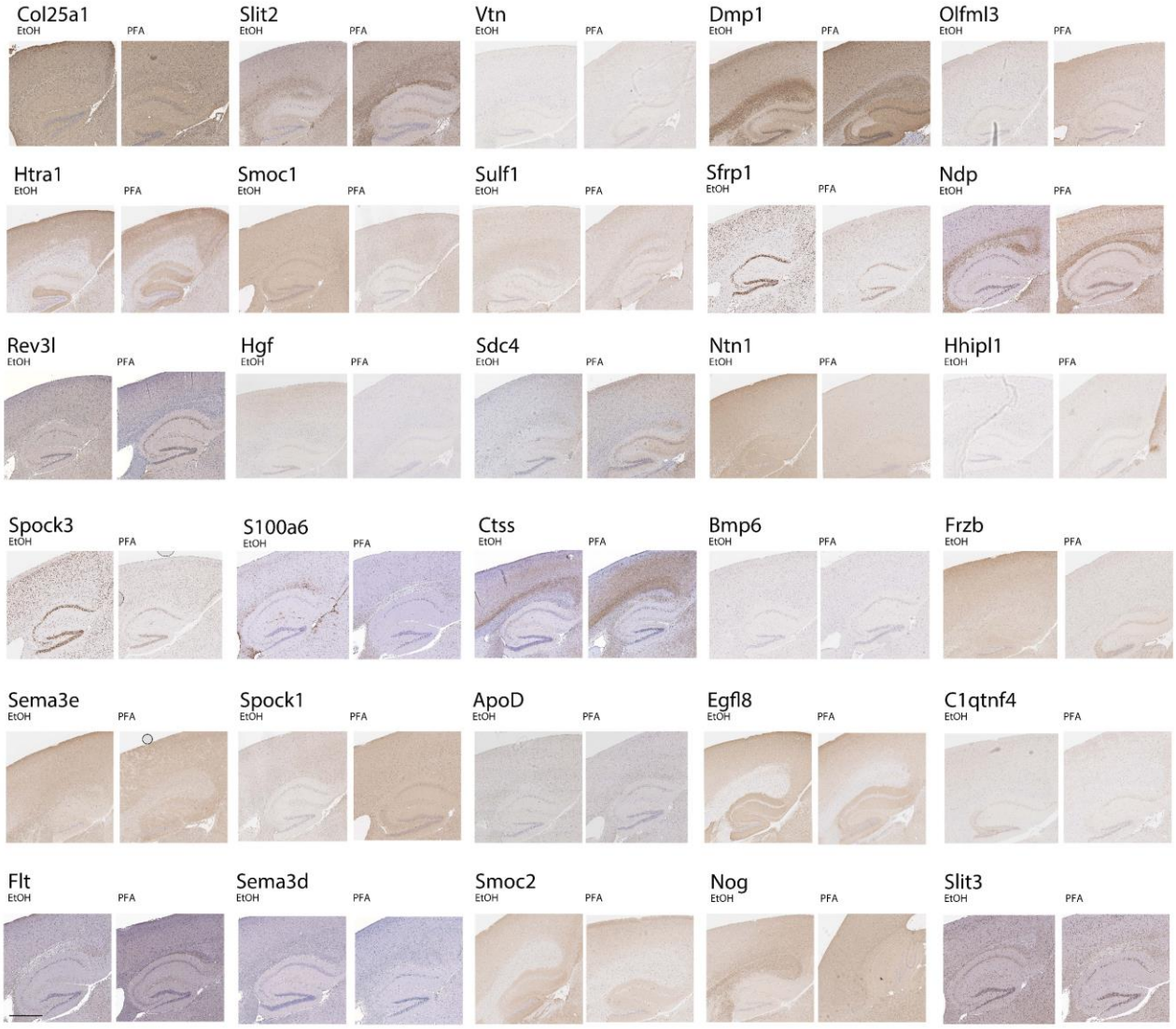

Figure S7A. non-Tg staining, fixation effects, co-localization, and astrocyte staining.

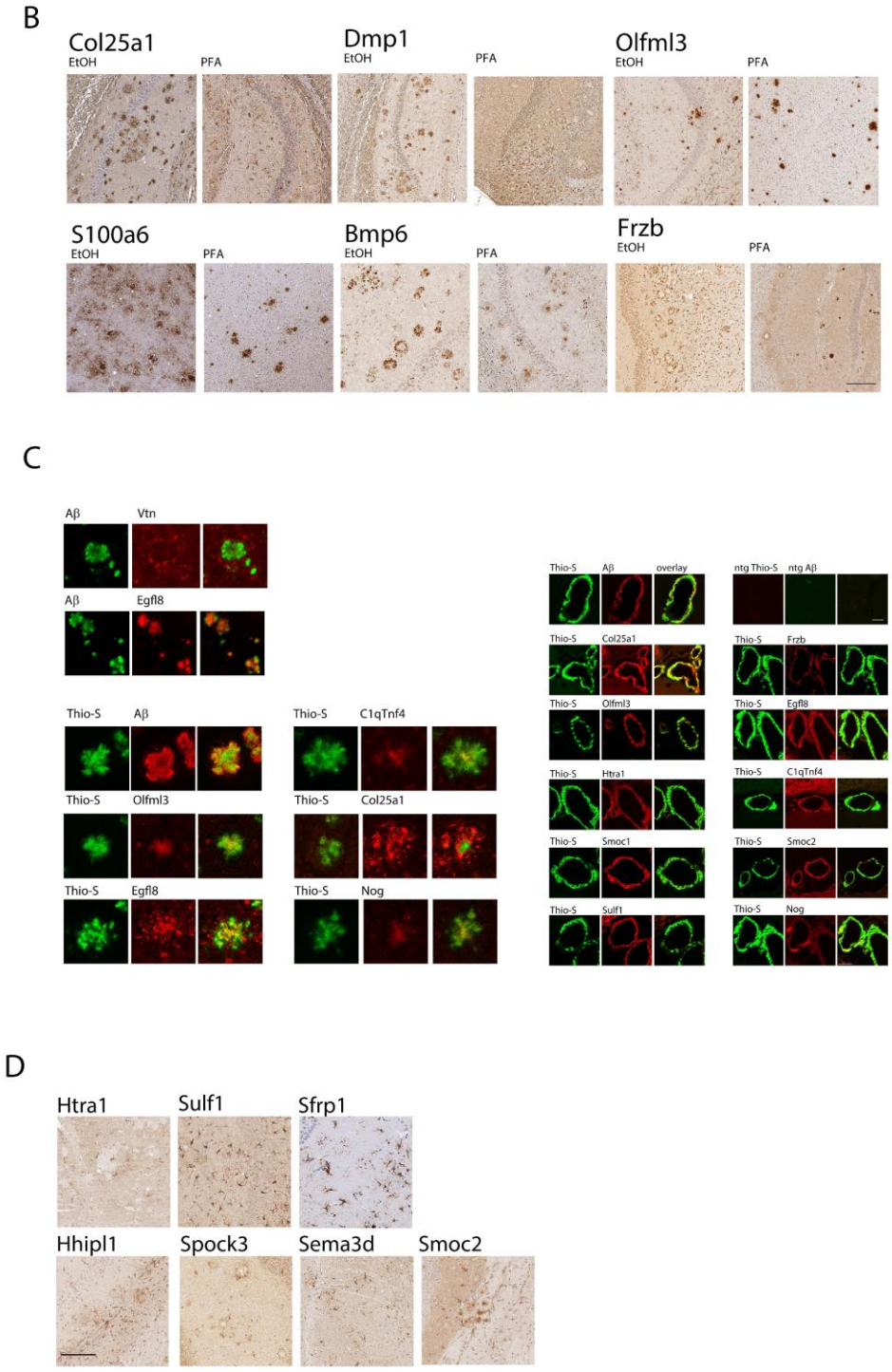

Figure S7B-D. non-Tg staining, fixation effects, co-localization, and astrocyte staining.

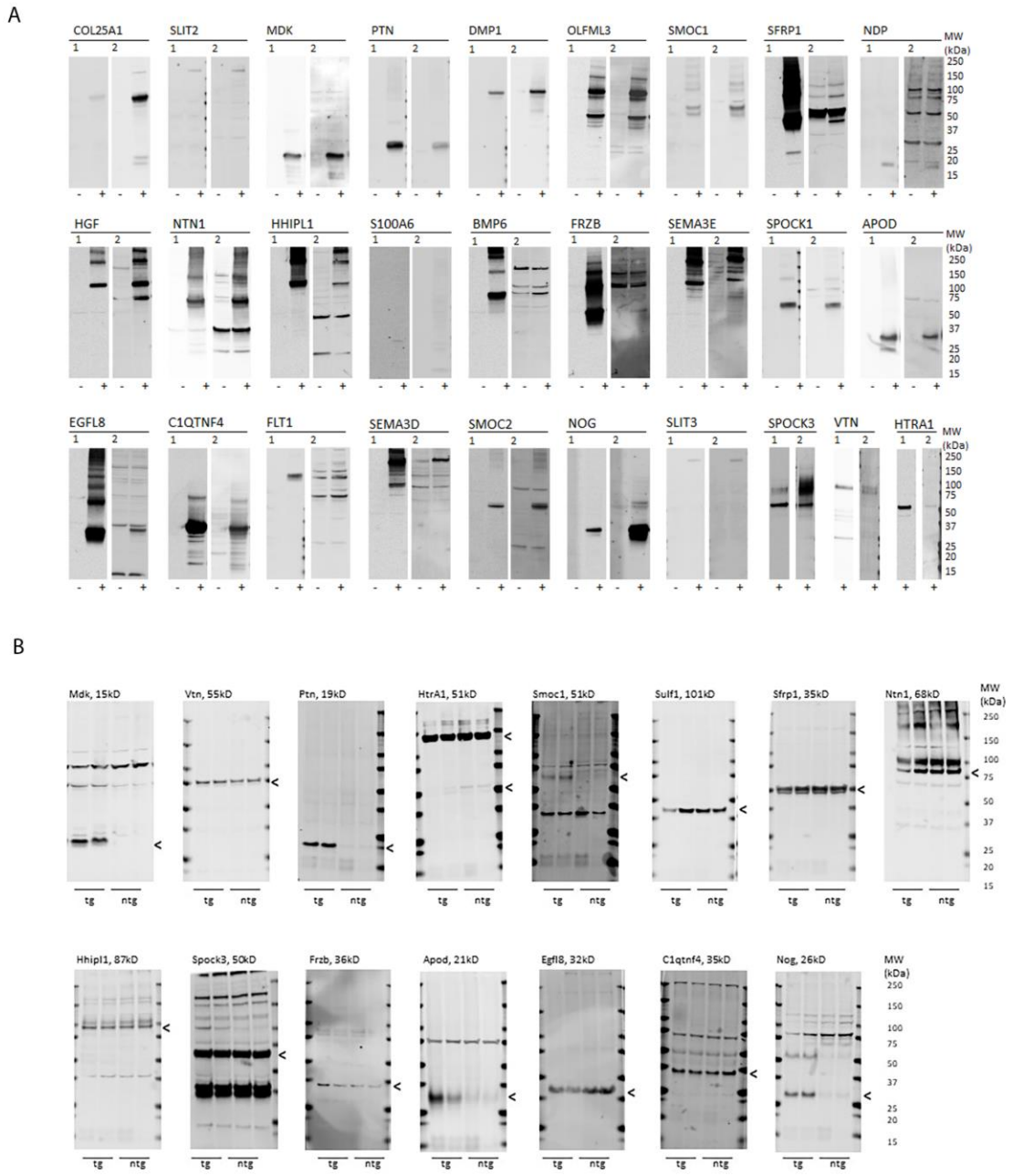

Figure S8. Antibody validation studies and additional DEPS validated by Western blotting.

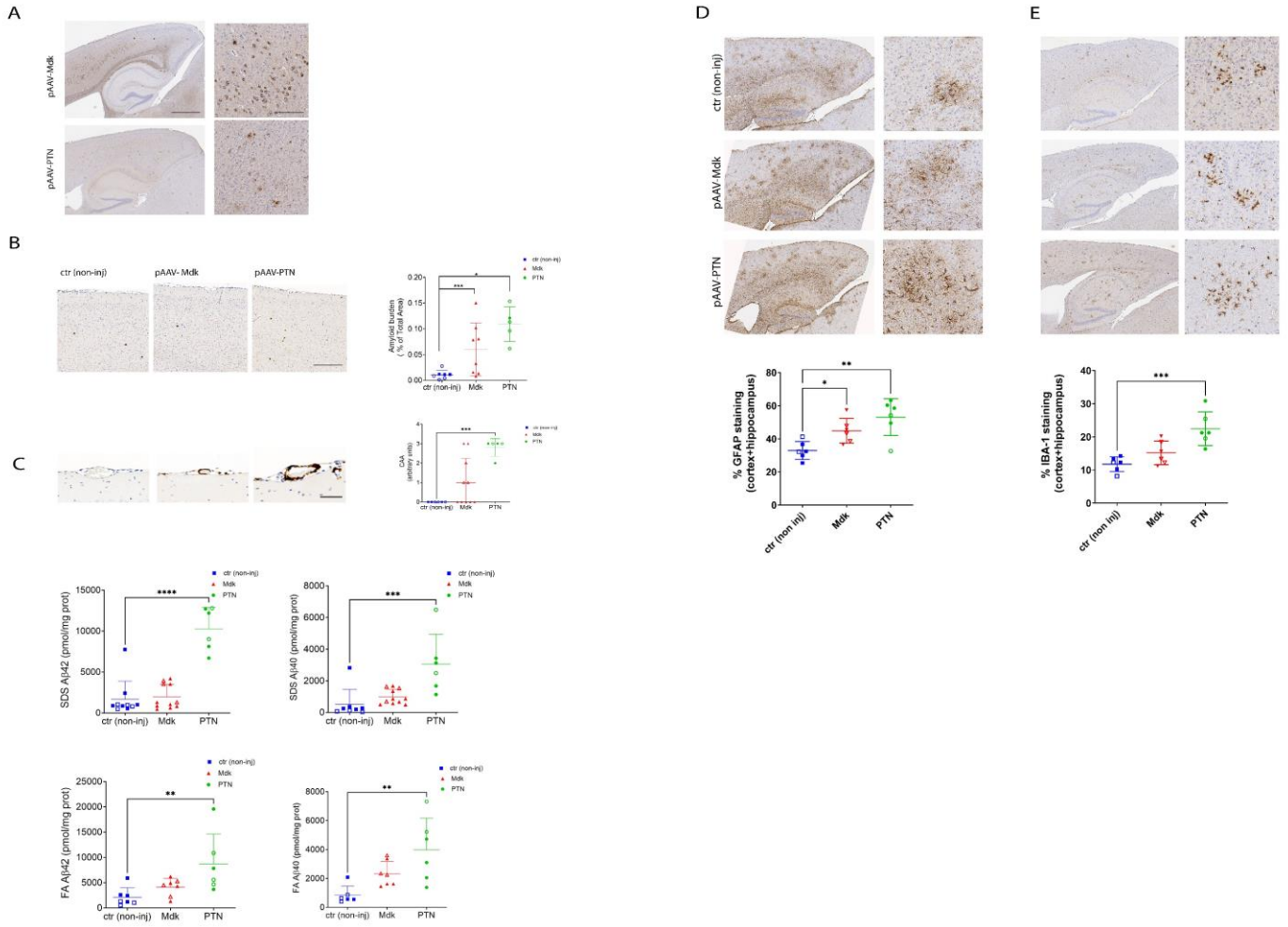

Figure S9. Midkine and Pleiotrophin overexpression increase formation of Aβ amyloid deposition and CAA in 3M CRND8 mice and 6M mouse data on gliosis.

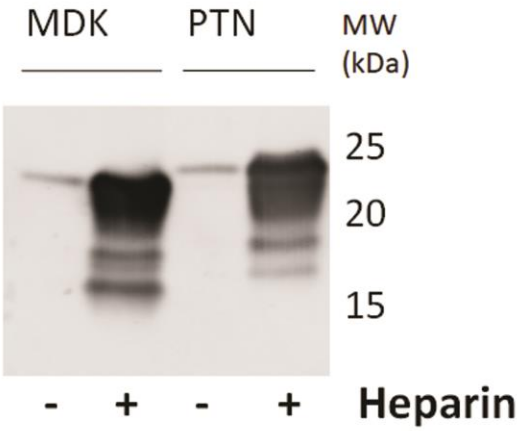

Figure S10. Mdk and PTN interact with heparin.

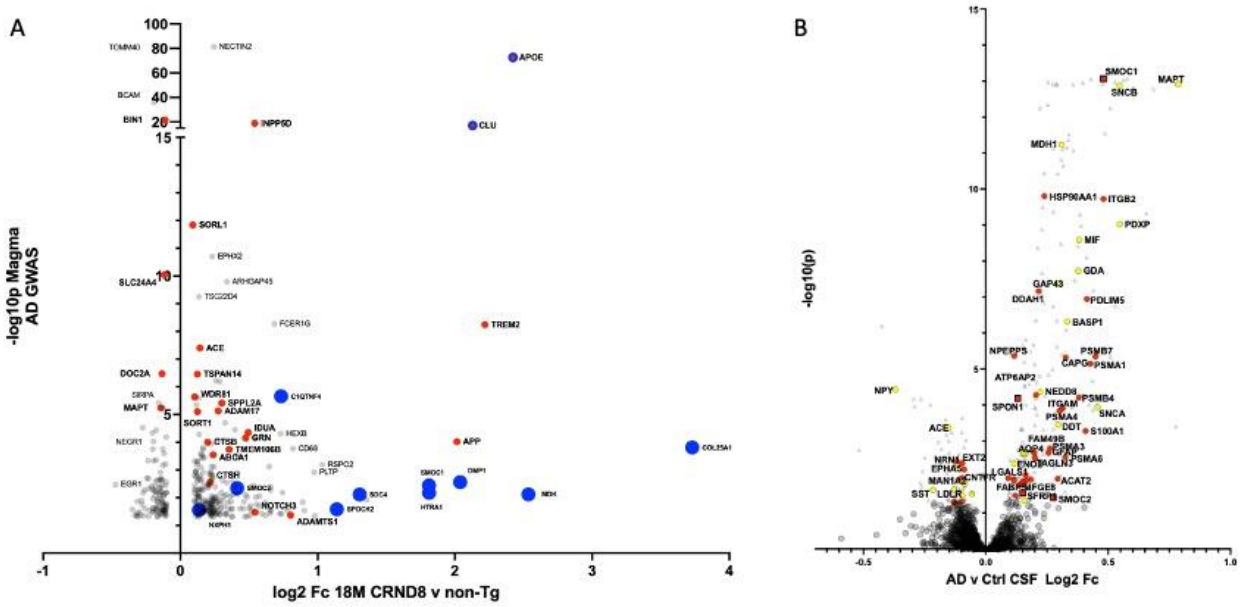

Figure S11. Contextualization of CRND8 18M Proteome by integration with AD GWAS MAGMA p values and AD CSF proteomic changes

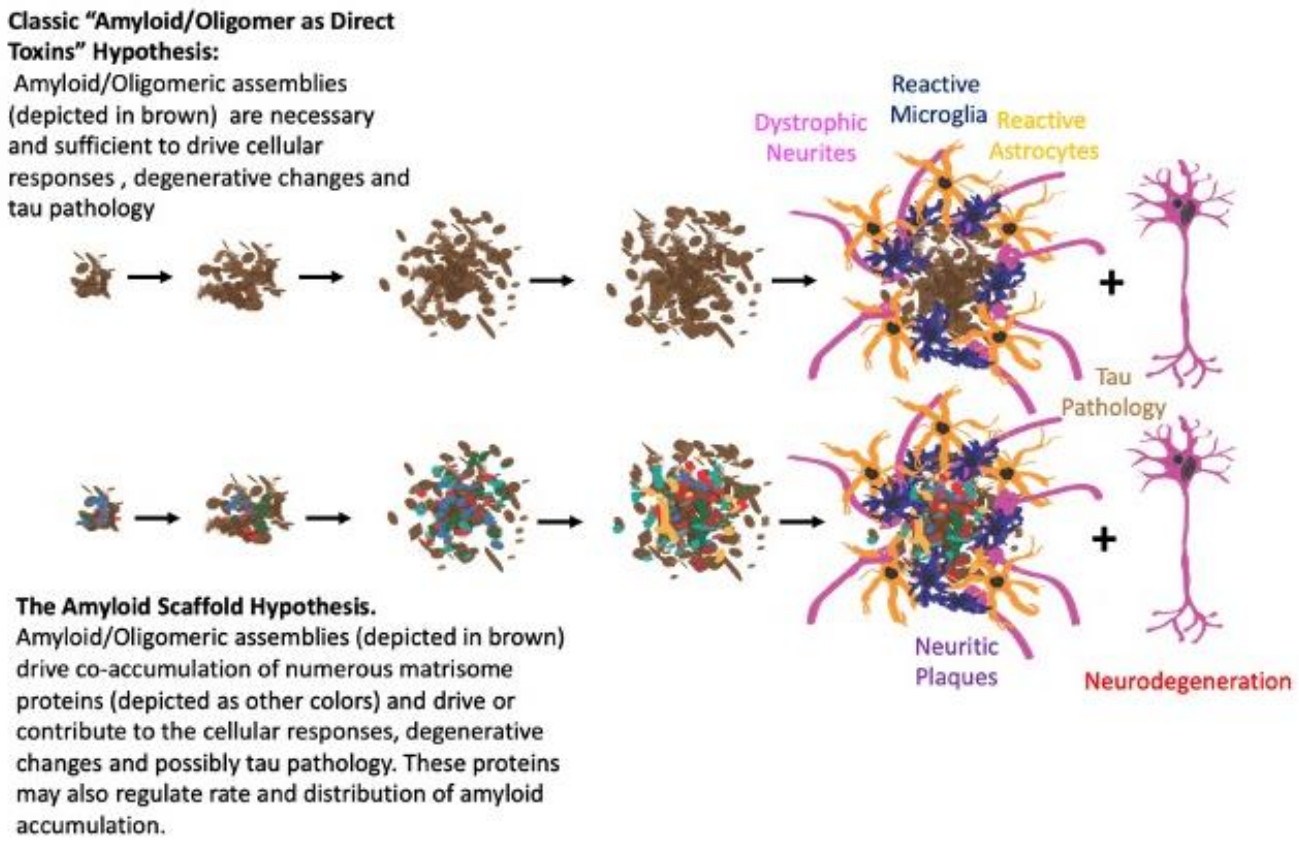

Figure S12. A schematic illustrating the Amyloid Scaffold Hypothesis.